University of Trento

Department of Civil, Environmental and Mechanical Engineering

---

Luca Adami

Multi-decadal morphodynamics of alternate bars in channelized rivers: a multiple perspective

PhD Thesis

April 2016

(this page has intentionally been left blank)

Luca Adami

Academic year 2014/2015

28^{th} cycle

PhD Student at Department of Civil, Environmental and Mechanical Engineering, University of Trento, Italy.
Academic Guest at Laboratory of Hydraulics, Hydrology and Glaciology, Zurich, Switzerland.
Home Institution:
Department of Civil, Environmental and Mechanical Engineering, University of Trento, Trento, Italy
Host Institution:
Swiss Federal Institute of Technology Zurich, Laboratory of Hydraulics, Hydrology and Glaciology, Zurich, Switzerland
Supervisors:
Guido Zolezzi, Department of Civil, Environmental and Mechanical Engineering, University of Trento, Italy.
Walter Bertoldi, Department of Civil, Environmental and Mechanical Engineering, University of Trento, Italy.

(this page has intentionally been left blank)

Abstract

Alpine rivers have been regulated to claim productive land in valley bottoms since the last two centuries. Width reduction and rectification often induced the development of regular scour-deposition sequences, called alternate bars, with implications for flood protection, river navigation, environmental integrity.

Understanding how alternate bars evolve in rivers and defining the key aspects that influence the development of these regular deposits of sediments represents a challenge that is not fully described. Most studies on alternate bars are in fact based on mathematical theories, laboratory experiments and since 1990s numerical simulations, but only few studies on field cases have been performed so far.

The goals of this work are: i) to quantify the morphodynamics of alternate bars in the Alpine Rhine River, with a particular emphasis on bar migration; ii) to assess to what extent the predictions of analytical bar theories are consistent with field observations and to explore how theories may help interpret observed alternate bars dynamics; iii) to determine the ability of a numerical model to simulate correctly the formation and the length scale of alternate bars and the influence of different multi-decadal inflow conditions.

The 42 km chosen reach is located along the border between Austria and Switzerland, between the confluences of Landquart and Ill rivers. The whole reach has been completely embanked starting from the 19th century, so alternate bars have been present for more than a century. Moreover the simplification of the cross section, together with the presence of only few bends, puts the Alpine Rhine in the ideal position to be compared with analytical theories of alternate bars in straight channels.

The goals are achieved by analyzing a dataset of freely available Land-

sat imagery, which combine unprecedented temporal length (3 decades), spatial length (more than 400 channel widths) and temporal resolution (around 3 images per year).

Bars show a spatially selective behavior, with short bars occurring in distinct straight reaches with respect to longer bars. The same evidence is found in terms of bar migration, so that short bars are shown to migrate more than longer bars, in agreement with theoretical predictions. A full range of bar wavelengths and more complex patterns occur in reaches with bends and ramps. Bar height, obtained from cross section monitoring, was found to be much more uniform. The temporally long dataset, including approximately 30 floods with different magnitude and duration, allowed the investigation of bar migration as a function of discharge, showing that bars migrate faster for intermediate floods.

Predicted values of linear theories for free and forced bars in straight channels are in good general agreement with field observations, when considering conditions of bar formation and bar wavelength. Comparing theories and observations suggests that theoretical outcomes may represent the boundaries of the actual, wide range of bar behaviour, which likely reflects non-linear interactions, flow unsteadiness, sediment size heterogeneity and finite length of straight reaches, which are not retained in linear theories.

Non-linear interactions are investigated through the 2D numerical morphodynamic model Basement, developed at the Swiss Federal Institute of Technology of Zurich. Preliminary investigations focus on the role of the transverse sediment transport, that behaves as a diffusive term. The numerical diffusion can be indirectly evaluated starting from the calibration of the coefficient of the diffusive term. A benchmark methodology to evaluate the lateral and numerical diffusion is defined. The results are used in the morphological calibration of the model. The spatial trend of wavelengths is in general agreement with the field data, and the migration takes place mainly in correspondence to short bars, whereas long bars tend to elongate with time. The choice of a constant discharge or a real hydrograph influences the time scale of bar evolution.

The present analysis results in the longest spatial and temporal field case study of river bars in channelized rivers with a temporal survey reso-

lution that allows the investigation of the effect of individual flood events, and provides new quantitative data on bar wavelength and migration. The dataset provides useful information to assess the applicability of analytical bar theories, so far mainly tested against flume experiments, and following recent attempts in French and Dutch streams. Moreover, a novel two-dimensional morphological benchmark to access the role of numerical diffusion is proposed.

Acknowledgements

I would like to thanks my supervisors Guido Zolezzi and Walter Bertoldi for their continuous support and guidance throughout the whole period of my PhD research period. The enthusiasm in the research that we shared made the entire period unforgettable.

For the wonderful period I spent at VAW, I am really grateful to the Applied Numerical group of the Swiss Federal Institute of Technology of Zurich, in particular to Annunziato Siviglia for his right words in the right moments and to David Vetsch for providing me field data of the Alpine Rhine and speed-up my research through his comments.

I really thanks Eric Mosselman for his clear and precise comments and feedbacks on this thesis.

My gratitude goes to Marina Rogato, Aureliano Cerreti and Claudia Fraizinger for taking care of all the administrative and bureaucratic issues of the PhD period.

I would like to thanks all the friends and colleagues that shared this intense period with me for all the scientific discussions and jokes we have shared in these three years.

I thank my family and the family of my wife for their constant and unconditioned support and for been present especially in all the moments of need.

Finally, I would love to express my heartfelt gratitude to my lovely wife Elena.

Contents

List of Figures

List of Tables

(this page has intentionally been left blank)

Chapter 1

Introduction

1.1 Context

River morphology affects the dynamics of water and sediment, and is also affected by them. This interaction, mostly investigated through a Newtonian mechanics approach [*Church and Ferguson*, 2015], brought the attention to the development of morphological patterns resulting from such mutual feedbacks that are typically non-linear and characterised by threshold behavior. In the evolution of river morphology such interaction develops within unsteady flow regimes, variable sediment supply, local effects of channel geometry, all being common characteristics of a complex river system. Moreover, the riparian ecotone (vegetation, *Gurnell et al.* 2012; *Camporeale et al.* 2013; *Solari et al.* 2016 and fauna, *Curran and Hession* 2013; *Nagayama et al.* 2015; *Reid and Church* 2015) interacts with the abiotic components and further complicates the picture. Vegetation interacts through (i) the abovegorund biomass that affects the flow field and the sediment transport, (ii) the belowgorund biomass that modifies the hydraulic and mechanical properties of the substrate [*Gurnell*, 2014, 2015]. Fauna is especially affected by the abiotic components [*Hauer*, 2015].

Efforts to confine rivers using artificially stabilised banks to discourage bank erosion have been put in place in Europe since the Roman times [*Church and Ferguson*, 2015] and have been continually practiced through the medieval times [*Brown*, 1991], up to the present period [*Nakamura*

et al., 2007; *Mähr et al.*, 2014]. The increasing settlement of river floodplains, the increase of land value and the established conviction that society has to be more and more protected by natural hazards are only some of the recent anthropogenic constraints that brought rivers to be channelized [*Nienhuis and Leuven*, 2001; *Brinson and MalvÃąrez*, 2002; *Tockner and Stanford*, 2002; *Palmer et al.*, 2009]. Such interventions often modify the natural morphological dynamics of the river as well as the river ecosystem [*Lane and Richards*, 1997; *Whipple and Tucker*, 2002; *Surian and Rinaldi*, 2003; *Lytle and Poff*, 2004], determining profound alterations of riverine landscapes and of their related hydro-morphological functioning. Such transformations strongly affect sediment transport processes, potentially modifying both the catchment scale sediment budget and altering the local transport capacity and bedform formation. In particular, simplification of the morphology and channelization affected the form and dynamics of river bars, one of the fundamental fluvial patterns at the reach scale. In many channelized streams regular patterns of alternate bars developed as a consequence of river embankments and straightening (e.g. *Ikeda* 1984; *Chang* 1985).

Alternate bars can be viewed as sediment waves with regular sequences of scours and deposits, alternating along the left and right banks, with a wavelength that scales with the channel width (generally in the range of 5-20 widths), and with height scaling with the channel depth. They have been extensively studied for decades because of their huge implications for bank erosion, navigation, flood risk, stability of built structures and the quality of physical habitat for freshwater and terrestrial species.

The process of formation and the characteristic length scale of alternate bars have been explored mainly by laboratory analysis started since the 1970s [*Schumm and Khan*, 1972; *Sukegawa*, 1972] and the 1980s [*Fujita and Muramoto*, 1982; *Jäggi*, 1984; *Ikeda*, 1984; *Chang*, 1985; *Fujita and Muramoto*, 1985] and continued with subsequent works by *Garcia and Niño* [1993]; *Lanzoni* [2000a,b]; *Crosato et al.* [2011, 2012]. On the opposite, field analyses are still rare [*Lewin*, 1976; *Welford*, 1994; *Rodrigues et al.*, 2012; *Eekhout et al.*, 2013; *Claude et al.*, 2014; *Jaballah et al.*, 2015; *Rodrigues et al.*, 2015].

An indication of the properties of alternate bars (e.g. wavelength,

migration speed, temporal growth rate and spatial damping rate) can be obtained from linear stability analysis of the mathematical system of equations that describe the flow and sediment dynamics [*Hansen*, 1967; *Callander*, 1969; *Blondeaux and Seminara*, 1985; *Struiksma et al.*, 1985]; indications on bar amplitude can be obtained from weakly non-linear analysis [*Colombini et al.*, 1987; *Schielen et al.*, 1993].

From the consistent theoretical framework developed by various scientific schools in the last four decades, two distinct types of bars can be theoretically found in straight channels: (i) free migrating bars, and (ii) hybrid steady bars. These two types are generated by different types of streamwise boundary conditions of the governing system of equations and by the possible presence of external forcing conditions, and reflect two distinct morphological responses of the river/channel configuration. Such theoretical framework has received a strong support from laboratory observations in scaled physical experiments, whereas the ability of these theories to predict the alternate bar behavior in more complex situations typical of real streams on the one hand, and to facilitate the interpretation of field observations on the other hand, have been explored only quite recently [*Welford*, 1994; *Eekhout et al.*, 2013; *Adami et al.*, 2014; *Jaballah et al.*, 2015; *Rodrigues et al.*, 2015], such integration representing still an open research field.

A complementary approach to study the properties and the dynamics of alternate bars is through numerical morphodynamic models. Morphodynamic numerical models advanced in the last decades by developing, with different numerical schemes, valuable tools to simulate geomorphic changes in natural and artificial river channels [*Struiksma et al.*, 1985] (subsequent development and applications on the 1980s and 1990s [*Lane et al.*, 1999; *Nicholas*, 2013; *Rousseau et al.*, 2016; *Siviglia and Crosato*, 2016]). Processes of formation and development of alternate bars have been studied mainly through 2D morphological models (e.g. *Takebayashi and Egashira*, 2001; *Defina and Lanzoni*, 2002; *Federici and Colombini*, 2002; *Defina*, 2003; *Bernini et al.*, 2009 and *Crosato et al.*, 2011, 2012). However, despite that both analytical and numerical models have their roots in the same governing mathematical system, and ultimately provide different solutions of that system with varying levels of approximations,

the integration between the numerical and the theoretical analytical approaches has been achieved only rarely so far [*Siviglia et al.*, 2013]. Moreover, a consistent standard practice on benchmark validation of morphological numerical models through analytical morphodynamic theories is still a challenge [*Siviglia et al.*, 2013].

The present work broadly aims at increasing our present understanding on the morphodynamics of alternate bars in channelized river systems by integrating an observational (remote sensing) approach on a representative case study, an analytical/theoretical approach applied to the same case study and the numerical modelling of alternate bar dynamics benchmarked through analytical theories.

The work focuses on three distinct aspects of the study of alternate-bar morphodynamics: (i) the long term analysis of the field case of the Alpine Rhine river, which represents a classical, well known example of a regulated river (see Fig. 1.1) composed by fixed levees, straight reaches and regular bends in which alternate gravel bars spontaneously form and migrate since more than a century; (ii) the analysis of the outcomes of the application of analytical solutions of linear and weakly non-linear theories to the field case of Alpine Rhine river, in terms of bar properties (wavelength, celerity of migration and height) and theoretical thresholds (critical and resonant behaviours); (iii) a numerical analysis of free and forced alternate bar formation (through the freely available 2D morphodynamic model Basement), which is applied to the field case of the Alpine Rhine river, by means of different scenarios of analysis.

1.2 Research questions

The present PhD work has been developed along three main research elements, which are reported below together with the key research questions that have been investigated:

1. *Long term morphodynamics of alternate bars in a straightened river*

    - What are the key properties and processes related to the multi-decadal evolution of a long straightened river with alternate bars?

Figure 1.1: A comparison between Fig. 1 of *Jäggi* [1984] in the left panel and the satellite image of the Alpine Rhine river in the right panel (*Source:* "Alpine Rhine": 47°2′3.92″ N, 9°29′26.97″ E. **Google Earth**. January 7, 2009. August 5, 2015).

- What is the role of fixed planform constraints (e.g. bends and ramps) in the development of migrating or non-migrating bars?

2. *Application of analytical bar theories to a real case*

- Which approach can be proposed for the application of analytical theories to field cases, characterized by markedly different settings?
- To which extent can fundamental theoretical behavior and characteristics of free and forced bars be observed in real regulated

rivers and how do they correspond to the theoretical settings?

- To which extent can analytical theories help interpreting field data and explain observed behavior?

3. *Numerical modelling the long term evolution of alternate bars*

   - To which extent is it possible to predict the observed alternate bar properties and behavior in a real case at a multi-decadal time scale through a numerical morphodynamic model?
   - How can the mutual effects of the gravity affects on sediment transport and of the numerical diffusion be quantified in numerical studies of bars, benchmarked with analytical theories?
   - What is the role of event-scale discharge variability on the multi-decadal evolution of bar properties and behaviors?

1.3 Outline of the thesis

This thesis is outlined in six chapters.

- Chapter 2 reviews the state of the art of the theoretical framework on alternate bars morphodynamics in straight channels.
- Chapter 3 describes the observed multi-decadal alternate bar dynamics of the Alpine Rhine river through the analysis of satellite images.
- Chapter 4 presents and discusses the application of free and forced theories of alternate bars to the field case of the Alpine Rhine.
- Chapter 5 describes the results of the numerical modelling of the multi-decadal alternate bar dynamics of the Alpine Rhine river.
- Chapter 6 summarizes the key findings of the present work and the suggestions for future investigations.

Two appendices complete the thesis:

Appendix A presents the results of a sensitivity analysis of the closure relation of the system of equations solved by free bar theory.

Appendix B shows the numerical simulations of migrating and non-migrating alternate bars in straight domains.

Chapter 2

Alternate bars in straight channels: theoretical background

2.1 Introduction: types of alternate bars

Several mathematical theories have been proposed since the 1960s [*Callander*, 1969] with the aim to evaluate and to predict the morphodynamics of alternate bars in straight channels. These mathematical theories, typically based on the two dimensional (depth averaged) Saint Venant - Exner shallow water system of equations [*Tubino et al.*, 1999], solve analytically (or semi-analytically) this mathematical representation of the physical system. In these '*bar theories*' analytical solutions in closed form are most often obtained after introducing a series of simplifying hypotheses that aim to keep the mathematical problem at the lowest level of complexity, although maintaining the key physical ingredients for the analysed processes. This analytical approach results in models that require an almost negligible computational time. Their main strength is the possibility they offer to easily evaluate the role of the most important governing parameters of the physical processes, together with the ability to estimate the relevant spatial and temporal time scales of bar morphodynamics.

Here a general summary is proposed of the existing theories on alternate bars, which consider an infinitely long straight channel domain. Like many other analytical models for river bars and meandering, these theories evaluate the main properties of alternate bars in the specific case of constant values of flow discharge (Q^*), channel width (W^*), reach longitudinal slope (s) and mean sediment grain size (d_{50}^*), that usually correspond to their reach-averaged values.

Note that, within this work, several dimensional parameters are denoted with an asterisk (*). This choice has been made to maintain consistency with the Italian scientific literature on the subject.

Moreover, these models assume flow conditions in which the entire cross section is actively transporting sediments, so that the channel width corresponds to the morphologically active width [*Ashmore et al.*, 2011; *Zolezzi et al.*, 2012].

Two distinct physical processes can theoretically trigger alternate bar development in straight reaches with constant active width. The first is a *free* instability mechanism of the riverbed under a uniform incompressible flow (free bars: *Blondeaux and Seminara*, 1985; *Colombini et al.*, 1987; *Seminara and Tubino*, 1992; *Schielen et al.*, 1993). Alternate bars in straight channels can also be forced by local persistent perturbations of the constant-width straight-channel planform, e.g. those associated with the sharp transitions from bends to straight reaches or with localized narrowing. Following the terminology proposed by *DurÃš et al.* [2015], local bars arise from the presence of forcing (e.g bend, width variation) and their size is proportional to the forcing. These bars are called *forced* bars. *Parker and Johannesson* [1989] referred to these bars as 'curvature-driven' bars, since the most common bars of this type are point bars. *Hybrid bars* arise from morphodynamic instability, but they also need the presence of forcing (hybrid bars: *Olesen*, 1984; *Struiksma et al.*, 1985; *Struiksma and Crosato*, 1989). Herein, both forced and hybrid bars are indicated as *forced*, following the terminology of the stability analyses. Persistent local perturbations can be represented by groynes, bridge piers, ramps or other local river structures, as well as by any other relevant abrupt planform change in space. A classical example is a transition between a straight reach and a bend of constant radius [*Struiksma et al.*, 1985], which causes

a discontinuity in channel curvature.

In addition to the responsible physical mechanism, the distinction between free and forced bars reflects the mathematical type of the governing differential system that is solved. In the case of free bars a homogeneous solution of the Shallow Water-Exner differential system of equations (SWE) (e.g. *Tubino et al.* 1999) with periodical streamwise boundary condition is obtained, while in the case of forced bars a non-vanishing forcing term is present in the streamwise boundary conditions [*Struiksma and Crosato*, 1989; *Zolezzi and Seminara*, 2001].

Linear and weakly non-linear theories consider bars as small-amplitude perturbations (much smaller compared to the reach-averaged flow depth) of the bed topography. Linear theories allow to predict conditions of existence, bar wavelengths and migration properties of free and forced bars. The amplitude of free alternate bars is predicted only by non-linear theories [*Colombini et al.*, 1987; *Schielen et al.*, 1993], while the amplitude of forced bars depends on both the geometry of the local perturbation and on non-linear effects. In straight channels, linear theories predict free alternate bars to migrate downstream and forced bars to be non-migrating; moreover, free migrating bars are predicted to be nearly two times shorter (L^*/W^* 6 $\div$ 8) than forced steady bars (L^*/W^* 15 $\div$ 20), where L^* denotes the bar wavelength. Comparable length scales are predicted by non-linear theories, whereas bar migration rate is largely overestimated by linear theories [*Colombini et al.*, 1987]. Furthermore, theories of free bars assume indefinitely long straight reaches, while forced bar theories refer to a reach of semi-finite or finite length.

These assumptions strongly simplify the real heterogeneity that distinguish natural rivers characterized by unsteady discharge, heterogeneous grain size, varying width and slope. *Tubino* [1991] proposed an analytical non-linear theory that explores the role of discharge unsteadiness in the formation, wavelength and amplitude of free alternate bars. Such theoretical analysis describes the ratio between the temporal scale of floods in comparison with the morphological scale of the bar development. *Tubino* [1991] introduced the parameter U, defined as the ratio between these two scales, suggesting that for $U \gg 1$ floods do not last long enough for the riverbed configuration to reach morphological equilibrium, while in the

opposite case, $U \ll 1$, the bar morphology can be considered in equilibrium with the flow conditions (e.g. for an application on this, see: *Eekhout et al.*, 2013). The effect of grain size hetereogenity has been addressed by *Lanzoni and Tubino* [1999], who developed a linear theory for the case of free bars with bi-modal sediments, while *Repetto et al.* [2002] extended the bar theory to the linear case of (sinusoidally) varying width using two- and three-dimensional linear mathematical models. Finally, linear theory of free alternate bars under a dominant suspended load can be found in [*Tubino et al.*, 1999].

2.2 Governing dimensionless parameters

Bar theories are commonly based on a series of simplifying assumptions with the aim of focussing on the fundamental morphodynamical processes, while keeping the mathematical problem in a form that can be solved analytically. In the literature of analytical solutions of alternate bars in straight domains, it is often assumed that the channel is fed by a representative (constant) value of the flow discharge, the channel width and grain size are uniform, and the sediment transport mainly occurs as bedload at a rate that is in equilibrium with the stream transport capacity (e.g. *Colombini et al.*, 1987).

Once the above parameters are fixed, they define a reference uniform flow condition, which is the one occurring over a flat bed with the given discharge, channel slope, width and sediment diameter. For the sake of achieving more generality, analytical morphodynamic theories, including bar theories, are often formulated with reference to dimensionless equations, where every quantity is normalised by means of a corresponding *scale quantity* that is representative of the reach averaged reference uniform flow conditions. For this reason, the outcomes of analytical theories are often presented in terms of several dimensionless parameters that define a scale-independent set of reference uniform flow conditions. The key dimensionless parameters are presented below.

Quantities that refer to uniform flow conditions are indicated with the subscript '$_0$'. The first dimensionless parameter β is a measure of the

channel width to depth ratio:

$$\beta = \frac{W_0^*}{2D_0^*} \,, \tag{2.1}$$

where W_0^* and D_0^* are respectively the channel width and the water depth of the reference uniform flow. The parameter β is usually called '*aspect ratio*' or '*width ratio*' and is equal to half of the real aspect ratio of the channel cross-section.

The second dimensionless parameter is the Shields parameter θ, expressed as:

$$\theta = \frac{\tau^*}{(\rho_s - \rho_w)\, g d_{50}^*} \,, \tag{2.2}$$

in which τ^* is the mean shear stress that the fluid exerts on the riverbed, d_{50}^* is the median value of the bed surface grain size distribution, ρ_s and ρ_w are the mass density of the sediment and the mass density of the fluid (water) respectively, while $g \simeq 9.8\,\mathrm{m\ s^{-2}}$ is acceleration due to gravity.

The third dimensionless parameter, d_s, is the so called *relative roughness*: the ratio between the mean sediment diameter and the reference uniform water depth, expressed by:

$$d_s = \frac{d_{50}^*}{D_0^*} \,, \tag{2.3}$$

This means that the theory refers to rivers without ripples or dunes (i.e. gravel-bed rivers).

2.3 Governing equations

Mathematical modelling of bar morphodynamics in single-thread channels is commonly achieved through approximate solutions of the depth-averaged momentum equations and of the continuity equations for water and sediment flows, along with appropriate closure relationships that relate sediment transport rate and friction to local flow properties.

Here the governing mathematical system of SWE used to solve the general case of a single-thread straight channel is reported, expressed in

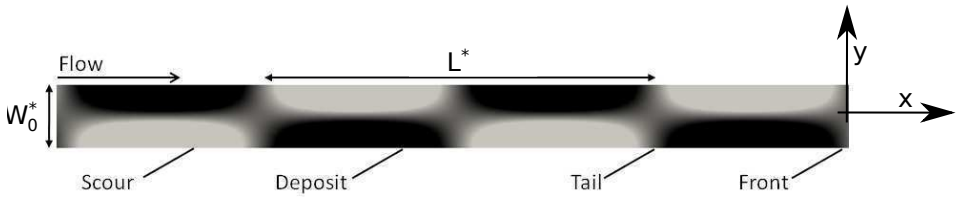

Figure 2.1: Planform view of alternate bar morphology, with definition of relevant geometric quantities.

dimensionless form and with reference to a classical Cartesian coordinate system (x, y) (see Figure 2.1):

$$U\frac{\partial U}{\partial x} + V\frac{\partial U}{\partial y} + \frac{1}{F_0^2}\frac{\partial\left(\eta + D\right)}{\partial x} + \beta\frac{\tau_x}{D} = 0 \tag{2.4}$$

$$U\frac{\partial V}{\partial x} + V\frac{\partial V}{\partial y} + \frac{1}{F_0^2}\frac{\partial\left(\eta + D\right)}{\partial y} + \beta\frac{\tau_y}{D} = 0 \tag{2.5}$$

$$\frac{\partial\left(DU\right)}{\partial x} + \frac{\partial\left(DV\right)}{\partial y} = 0 \tag{2.6}$$

$$\left(1 - p\right)\frac{\partial \eta}{\partial t} + \left[\frac{\partial q_s}{\partial x} + \frac{\partial q_s}{\partial y}\right] = 0. \tag{2.7}$$

In $(2.4 \div 2.7)$ each variable is dimensionless and has been obtained from its dimensional correspondent through normalization with a representative, reach-averaged uniform flow quantity. Namely, the channel width W_0^* has been used for the stream wise and transversal coordinates (x, y), the reach-averaged water depth D_0^* for the local water depth (D) and the reach-averaged uniform flow velocity U_0^* for the depth-averaged velocity field (U, V). W_0^* is adopted as the normalizing factor for the planform coordinates because alternate bar morphology displays relevant horizontal variations at this scale (e.g. bar wavelength). Moreover p is the sediment porosity and F_0 is the Froude number of the reference uniform flow.

Theories for free and forced bars in straight channels are based on perturbation solutions of the governing mathematical system. Linear theories assume bar amplitude to remain "small" and address (i - free bars) the stability of an initially flat bed and of the the imposed reference uniform

flow with respect to bed perturbations of bar-type and (ii - forced bars) the forced response of the flow field and riverbed to the presence of a fixed obstacle in the straight domain (e.g. channel narrowing, bridge piers).

In the presented $2D_{(xy)}$ system of four equations ($2.4 \div 2.7$) the unknowns are four, and precisely: D, U, V and η, where η represents the bed elevation.

In order to close this mathematical problem, closure relations that relate the shear stress τ and the sediment flow rate (q_x, q_y) to the flow characteristics are needed. A frequently used option is to express the former, τ, as function of the friction coefficient C, defined by:

$$\tau = (\tau_x, \tau_y) = (U, V) \left(U^2 + V^2\right)^{\frac{1}{2}} C \ , \tag{2.8}$$

where the friction coefficient can be computed through a variety of relations such as the *Einstein* [1950] formula:

$$C = 6 + 2.5 \ln \left(\frac{D^*}{2.5 d_{50}^*} \right) , \tag{2.9}$$

hence no ripples or dunes are considered.

The second closure, that relates the unit sediment transport rate with the local values of the Shields parameter and water depth, is written often assuming that the total sediment transport is due mainly to bed-load and that the local bed slope mainly affects the direction of the bed-load [*Engelund*, 1981]:

$$q^* = \left(q_x^*, q_y^*\right) = (\cos\delta, \sin\delta)\, \Phi \ , \tag{2.10}$$

where Φ represents the mean sediment load function, as described by Eqs. (2.18) and (2.19), while the angle δ, assumed small, is defined as:

$$\sin\delta = V^* \left(U^{*2} + V^{*2}\right)^{-\frac{1}{2}} - \frac{r}{\beta\sqrt{\theta}} \frac{\partial \eta^*}{\partial y^*} \ , \tag{2.11}$$

in which r is a parameter that assumes values in the range $0.3 \div 0.6$ [*Engelund*, 1981; *Olesen*, 1984; *Talmon et al.*, 1995].

It is important to note that another implicit assumption of bar theories is that sediment transport is assumed to occur at flow transport capacity, i.e. it is supply âĂŞ unlimited.

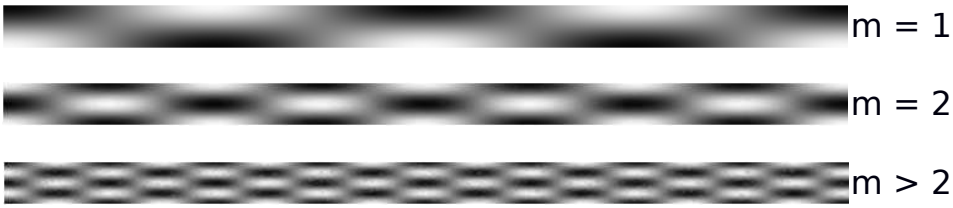

Figure 2.2: Examples of bed configurations with different transverse bar modes: from the case of alternate bars (corresponding to $m = 1$), to the case of central or mid-channel bars (corresponding to $m = 2$), to the case with multiple bars ($m > 2$).

2.4 Free bars in straight channels

2.4.1 Free-bar formation and linear stability

Free-bar formation is connected with an intrinsic instability of the channel bed. In this section a short overview of free-bar theory, as proposed by *Colombini et al.* [1987] is presented. We defined m as the transverse bar mode, which implies $m = 1$ for alternate bars, $m = 2$ for central bars, $m > 2$ for multiple bars (see also Figure 2.2). The system of equations presented herein is focused on the specific case of alternate bars ($m = 1$).

The flow domain that is investigated is represented by a straight channel with rectangular cross sections and constant width. Imposing constant water and solid discharge at the upstream (asymptotic) boundary, with solid discharge at equilibrium (capacity) with flow rate, free bar stability is studied through the governing equations ($2.4 \div 2.7$). The boundary conditions in the transverse direction impose vanishing lateral flux of water and of sediments between the channel and the lateral boundaries: $V = q_y = 0$.

A trivial analytical solution of system ($2.4 \div 2.7$) is the reference uniform flow described in 2.3, which reads:

$$\begin{cases} D = D_0 = 1 \\ U = U_0 = 1 \\ V = 0 \\ \eta = \eta_0 (x) \end{cases}, \tag{2.12}$$

where subscript '$_0$' refers to uniform flow.

System (2.4 ÷ 2.7) is solved studying the stability of a small (strictly infinitesimal) perturbation, with amplitude ϵ, of the uniform flow solution (2.12) that depends on time t and on (x, y), which reads:

$$\begin{cases} D = D_0 + \epsilon D_1(x, y, t) \\ U = U_0 + \epsilon U_1(x, y, t) \\ V = 0 + \epsilon V_1(x, y, t) \\ \eta = \eta_0(x) + \epsilon \eta_1(x, y, t) \end{cases} . \tag{2.13}$$

The assumption of infinitely long channel allows to assume a periodical structure of the perturbation in the streamwise direction. Therefore, focusing on the water depth D, but remembering that all four perturbations have the same functional structure, $D(x, y, t)$ reads:

$$D(x, y, t) = D_0 + \epsilon e^{(\Omega t + i\omega t + i\lambda x)} \sin\left(\frac{2\pi y}{W_0}\right) + c.c. \tag{2.14}$$

$$= D_0 + \epsilon e^{\Omega t} \sin\left(\frac{2\pi y}{W_0}\right) \cos(\lambda x - \omega t) + c.c. \tag{2.15}$$

where the exponential notation for complex numbers, together with Euler's rule ($e^{i\alpha} = \cos\alpha + i \sin\alpha$) are used in (2.15). This apparently meaningless equivalence is presented here because many analytical bar theories employ such notation, because it helps speeding up the long and somehow tedious algebraic calculations that eventually lead to the analytical solution.

The dimensional bar wavenumber λ is easily derived from the wavelength L^* (Figure 2.1) and it relates with the dimensionless bar wavelength, L^*/W_0^*, such that small wavenumbers correspond to long bars and vice versa. It reads:

$$\lambda = \frac{\pi W_0^*}{L^*} . \tag{2.16}$$

In (2.15), ϵ is a small (strictly infinitesimal) coefficient that sets the amplitude of the perturbation, Ω and ω are amplification rate and angular phase of the perturbation, respectively, and "c.c." stands for *complex conjugate*.

Note that the solution of the algebraic system that results from substituting the perturbations (2.13) with functional structure (2.15) into the

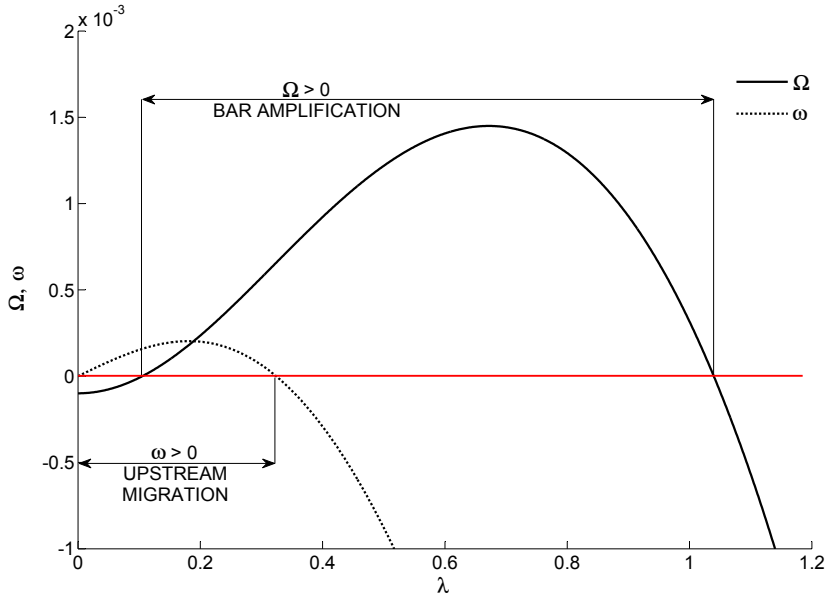

Figure 2.3: Amplification Ω and angular frequency ω of free alternate bars ($m = 1$) versus wavenumber λ, with $\theta = 0.10$, $d_s = 0.067$ and $\beta = 32.6$.

governing system (2.4 $\div$ 2.7) fundamentally consists of the possibility to quantify how bar amplification rate Ω and the intensity of angular frequency ω depend on the reference uniform flow parameters (θ_0, β and d_s), on the bar wavenumber λ and on the transverse bar mode m. The angular frequency ω quantifies bar migration in time and its direction (upstream or downstream).

The solution of the governing system yields an exponential growth of bar amplitude A:

$$\frac{\mathrm{d}A}{\mathrm{d}t} = \Omega A \Longrightarrow A(t) = e^{\Omega t} \; . \tag{2.17}$$

Solution (2.17) defines two well distinct regimes in terms of bar stability, depending on the sign of the amplification rate Ω. The initial bar wave can be flattened if $\Omega < 0$, **stable** regime, or grow in time if $\Omega > 0$, **unstable** regime.

For a given flow condition, i.e. given θ_0, β and d_s, the growth rate Ω and angular frequncy ω can be plotted versus bar wavenumber λ, as

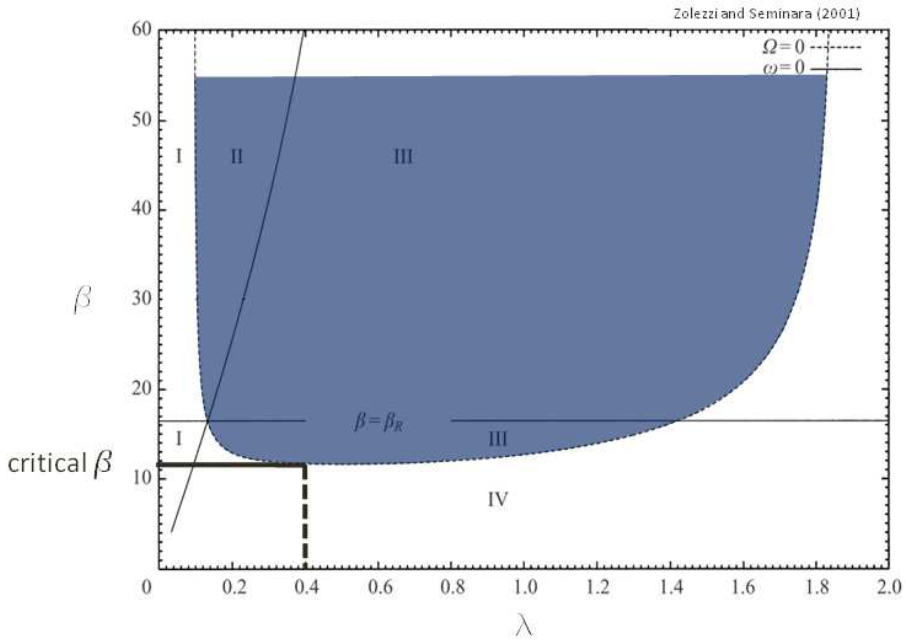

Figure 2.4: Marginal curve of bar amplification, β versus wavenumber λ with $\theta = 0.10$ and $d_s = 0.01$. Blue ($\Omega > 0$) and white ($\Omega < 0$) regions represent the unstable and stable configuration of alternate bars respectively. In the former ($\Omega > 0$) a perturbation tends to grow in time, so alternate bars can form, in the latter ($\Omega < 0$) a perturbation tends to be damped in time.

shown in Fig. 2.3. Fixing θ and d_s and varying the value of β, it is possible to note that for low values of β the amplification rate is always negative, while the amplification region widens for increasing β.

Changing the value of β and selecting wavenumbers with $\Omega = 0$ and also $\omega = 0$, it is possible to plot a graph that sums up alternate bars linear stability and migration properties in the form of neutral curves, i.e. curves denoting bar configurations that are marginally stable ($\Omega = 0$) or not migrating ($\omega = 0$) (Fig. 2.4 and Fig. 2.5).

In Fig. 2.4 and Fig. 2.5 these neutral curves are plotted for given values of θ and d_s: the black dotted line represents the condition of vanishing growth rate ($\Omega = 0$), while the black continuous line corresponds to non-migrating free bars ($\omega = 0$). The blue region of Fig. 2.4 ($\Omega > 0$) encloses all states that express intrinsic instability of the system, corresponding to free-bar amplification. On the other hand, the region below the marginal

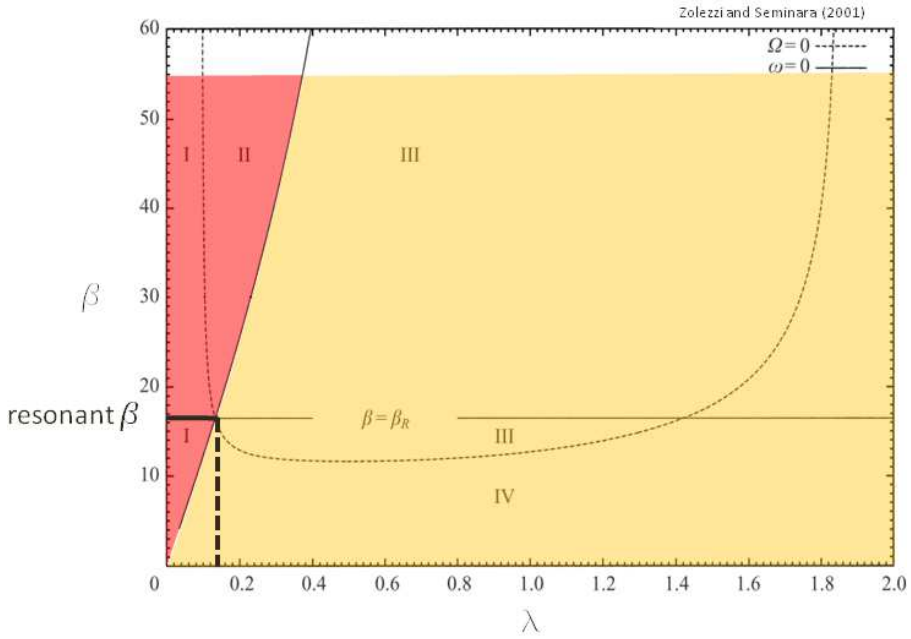

Figure 2.5: Marginal curve of bar migration, β versus wavenumber λ with $\theta = 0.10$ and $d_s = 0.01$. Red ($\omega > 0$) and yellow ($\omega < 0$) regions correspond to different directions of bar migration in time: in the red region a small-amplitude bar perturbation tends to migrate upstream, in the yellow region a bar perturbation tends to migrate downstream.

curve ($\Omega < 0$) corresponds to states where bars are stable, invariably leading to a flat bed through the suppression of the linear perturbation. The minimum value of β for bar formation is named "critical" and denoted with β_{cr}; and the corresponding wavenumber value is denoted with λ_{cr}. The shape of the neutral curve in Figure 2.4 is particularly relevant because it suggests that the channel aspect ratio is a key parameter for bar stability, because no free bars could form for relatively narrow and deep channels, i.e. having $\beta < \beta_{cr}$, regardless of the length of the bars. Starting from a subcritical condition (flat bed) and increasing β, at the limit of $\beta = \beta_{cr}$ bars with $\lambda = \lambda_{cr}$ start to develop. Note that while β_{cr} has a well defined limit, λ_{cr} has a smooth limit and can be found into a range between 0.3 and 0.7, though mostly can be found in the range $0.4 \div 0.5$, and is often close to the wavenumber having the maximum linear amplification rate, which is the wavenumber that is initially selected by the instability

process. The result on free-bar stability is related to a delicate physical balance between stabilizing and de-stabilizing effects. The key stabilizing role is played by gravity, which poses a limitation to the local bed slope associated with the development of bar forms. In the equations, the relative importance of this effect is associated with the parameter r, already defined in Eq. (2.10), which then is fundamental in the computation of the bar amplification rate Ω: if this value is set to $r = 0$, no stable regions are present ($\Omega < 0 \; \forall \, (\lambda, \beta) \in \mathbb{R}^2$) and a small-amplitude bar perturbation can only grow in time; if otherwise this parameter is set to a high value (its experimental limit being in the range up to $0.5 \div 0.6$) the opposite configuration is described: the neutral curve is shifted to higher values of β and bars tend to be invariably suppressed. Calibration of the value of the parameter r is also influenced by the choice of the roughness and of the bed-load formula.

In Fig. 2.5, the continuous line divides the $(\lambda - \beta)$ plane into two main regions: the left one, coloured in red, corresponds to positive values of ω and it corresponds to the region in which small-amplitude, linear free bars tend to migrate upstream; on the contrary, the larger region on the right, coloured in yellow, corresponds to negative values of ω, physically meaning that these bar wavenumbers tend to migrate downstream.

As shown in Fig. 2.5, the value of β that presents both $\Omega = 0$ and $\omega = 0$ identifies a second threshold aspect ratio for which free bars are theoretically non-migrating and non-amplifying. Such threshold is called *resonant* threshold (β_{res}) because it coincides with the theoretical resonance condition of purely periodic river meanders [*Blondeaux and Seminara*, 1985]. Only for $\beta > \beta_{res}$ unstable small-amplitude free bars (growing in time) can migrate upstream, while for $\beta < \beta_{res}$ only downstream migration occurs. These considerations strictly apply for initial, small amplitude bar perturbations, coherently with the linear approach under which they have been derived.

These theoretical results have found strong support from experimental observations on migrating bars. Laboratory experiments (e.g. *Kinoshita*, 1961; *Jäggi*, 1984; *Lanzoni*, 2000a; *Lanzoni*, 2000b and relatively few field observations (e.g. *Ferguson et al.*, 2011; *Eekhout et al.*, 2013; *Rodrigues et al.*, 2015; *Jaballah et al.*, 2015; *Adami et al.*, 2016) indicate that the

wavelength of migrating bars in straight reaches of mobile-bed channels ranges between 7 and 9 times the channel width. This range corresponds, in terms of wavenumber λ, to the interval $0.35 - 0.45$, consistently with theoretical predictions on the maximum linearly unstable wavenumber range, which falls in the neighbourhood of critical conditions ($\beta \simeq \beta_{cr}$).

The outcomes of the bar theories, such as values and limits of curves shown in Fig. 2.3, Fig. 2.4 and 2.5 are sensitive to the chosen sediment transport formula; in the cases presented in this report, two bedload formulas have been used. The classical *Meyer-Peter and Müller* [1948] formula reads:

$$\Phi = 8\,(\theta - \theta_{cr})^{\frac{3}{2}}\,, \tag{2.18}$$

where Φ expresses the mean sediment load function, and θ_{cr} is the threshold of the bedload motion, fixed to the value of $\theta_{cr} = 0.047$.

The framework of bar theories allows to adapt a variety of bed-load predictors, such as the modified versions proposed by *Wong and Parker* [2006]:

$$\Phi = 3.97\,(\theta - \theta_{cr})^{\frac{3}{2}}\,, \tag{2.19}$$

where the exponent of the original formulation is maintained and $\theta_{cr} = 0.0495$. The formula may also read:

$$\Phi = 4.93\,(\theta - \theta_{cr})^{1.6}\,, \tag{2.20}$$

where $\theta_{cr} = 0.047$ is maintained and the exponent is adjusted.

Though strictly valid only for small-amplitude bar perturbations, the outcomes of the linear theory for free bars provide useful information about bar wavelength and condition of formation. Information on bar amplitude, instead, can only be computed, on a theoretical basis, by accounting for non-linear effects (see next Section).

2.4.2 Free-bar amplitude and non-linear growth

Field and laboratory observations suggest that migrating bars may reach a rather uniform height in a given reach, which scales with water depth (e.g. *Ikeda* [1984]; *Knaapen et al.* [2001]).

Within the linear theory for free bars, Eq. (2.17) predicts an exponential growth of bar amplitude with time. Adopting a weakly non-linear theory for bar instability, it is possible to obtain a modified version of the amplitude equation that admits a theoretical equilibrium condition after a transient growth [*Colombini et al.*, 1987]:

$$\frac{\mathrm{d}A}{\mathrm{d}t} = \Omega A + \Omega_1 A|A^2| \; . \tag{2.21}$$

The non-linear amplitude equation (2.21) defines the time growth of bar amplitude towards an equilibrium condition, where Ω and Ω_1 are functions of λ, θ, β and d_s. The equilibrium bar amplitude corresponds to the condition $\mathrm{d}A/\mathrm{d}t = 0$; it is then possible to write (2.21), substituting the total derivative:

$$\Omega A + \Omega_1 A|A^2| = 0 \; , \tag{2.22}$$

which gives two possible solutions, written as follows:

$$A_1 = 0 \quad ; \quad A_2 = \sqrt{-\frac{\Omega}{\Omega_1}} \; . \tag{2.23}$$

Solution A_1 remarks that a possible equilibrium condition is the reference uniform flow on a flat bed. The non trivial solution A_2 shows how term Ω_1 must be negative for coherence of square root, remembering Ω is a positive term in the amplification region. The parameter Ω_1 represents non-linear suppressing effects that limit exponential growth. Examples of bar amplitude growth in time are plotted in Fig. 2.6.

Eq. (2.23) on free-bar equilibrium amplitude allows to derive a relatively simple expression for bar height H_{BM}, defined as the difference between the maximum and the minimum of the bed oscillation along one bar wavelength, [*Colombini et al.*, 1987]:

$$H^*_{BM} = D^*_0 \left[b_1 \left(\frac{\beta - \beta_{cr}}{\beta_{cr}} \right)^{1/2} + b_2 \left(\frac{\beta - \beta_{cr}}{\beta_{cr}} \right) \right] \quad \text{with} \quad \beta < 2\beta_{cr} \; . \tag{2.24}$$

In Eq. (2.24), D^*_0 is uniform-flow depth of the undisturbed channel while both b_1 and b_2 are functions of θ and d_s; the dependence of b_1 and

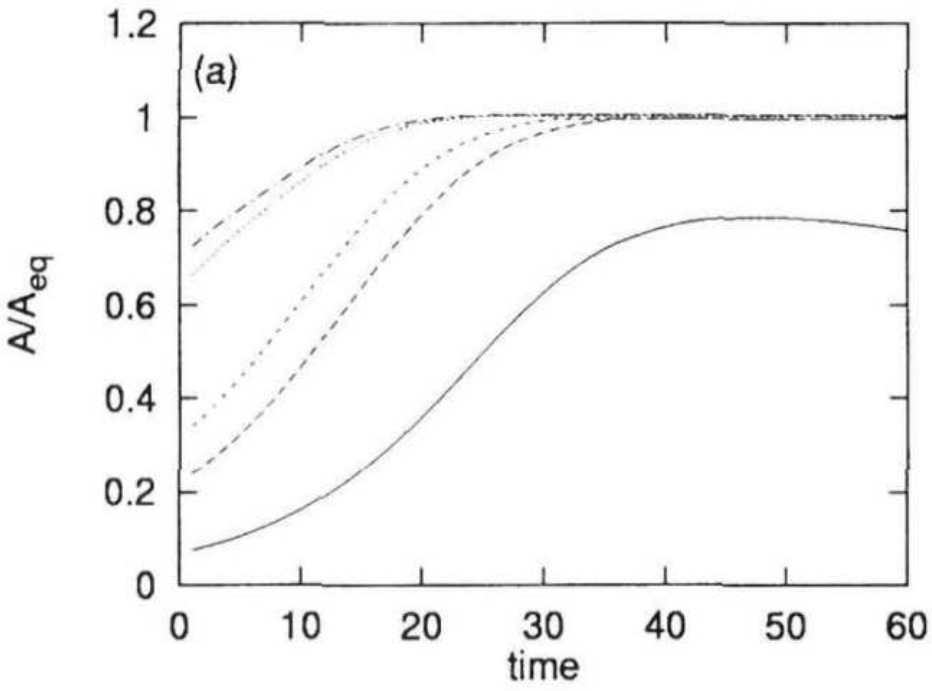

Figure 2.6: Time development of bar amplitude A scaled with equilibrium amplitude A_{eq} for different values of the initial amplitude A_0 (plane bed, $\theta = 0.1$,$d_s = 0.01$, $\beta = 15$, $\lambda = 0.2$. Reprinted from *Tubino et al.* [1999].

b_2 on these parameters being relatively smooth. In Fig. 2.7 and Fig. 2.8 the values of β_{cr}, b_1 and b_2 are presented for different values of θ and d_s, allowing an easy estimate of the equilibrium bar amplitude H_{BM}.

Relation (2.24) gives an important cue: the height of bars is not related with the absolute value of β but with its difference with the critical limit β_{cr}. Moreover, the equilibrium bar height scales with the reference uniform depth, as observed in the field.

This theoretical formulation can be compared with other empirical formulations, e.g. the one proposed by *Ikeda* [1984]:

$$H_{BM} = 0.18 d_s^{0.45} \beta^{1.45} \tag{2.25}$$

Finally, a weakly non-linear analytical theory like the one of *Colombini et al.* [1987] can also give a formulation for maximum scour η_M, defined as the difference between mean bed elevation and minimum elevation of

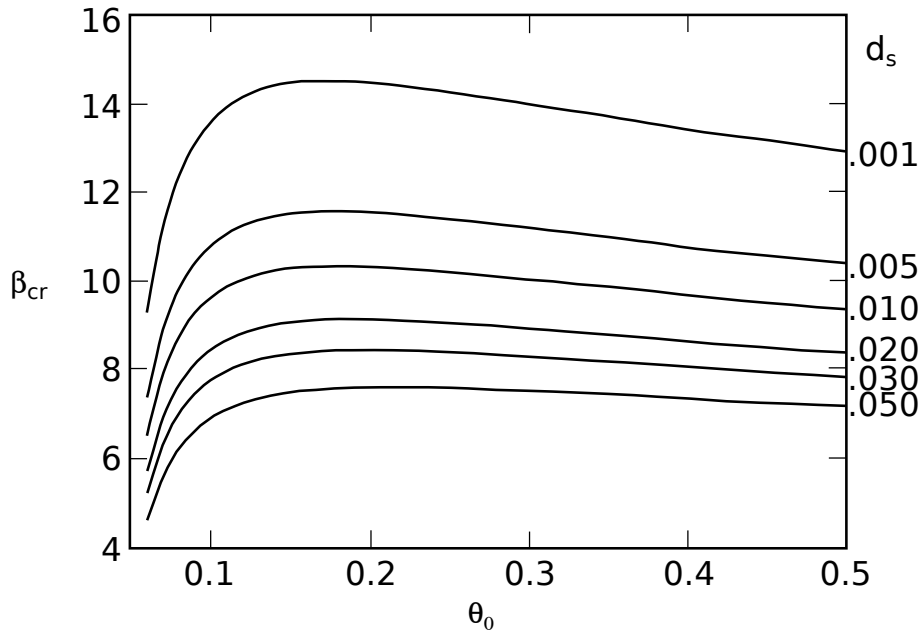

Figure 2.7: Curves of the critical aspect ratio β_{cr} for free bar stability as function of the Shields parameter θ for different values of d_s.

bar oscillation:

$$\eta_M = 0.57 H_{BM} \ . \tag{2.26}$$

Theoretical predictions on bar height have found satisfactory agreement with existing laboratory observations.

2.5 Forced bars in straight channels

As introduced in Section 2.1, also forced steady bars can theoretically be found in straight channels e.g. near a bend, a channel narrowing or a hydraulic structure. Forced bars in straight channels have been often named in different ways in the scientific literature. Other terms used to denote them include "steady bars" and "spatial bars". [*DurÃš et al.*, 2015] make an end to the ambiguity of the different terms by distinguishing 3 types of bars: free, forced and hybrid.

On the basis of theoretical analysis (e.g. *Olesen* [1984]; *Struiksma et al.* [1985]; *Seminara and Tubino* [1992]; *Zolezzi and Seminara* [2001])

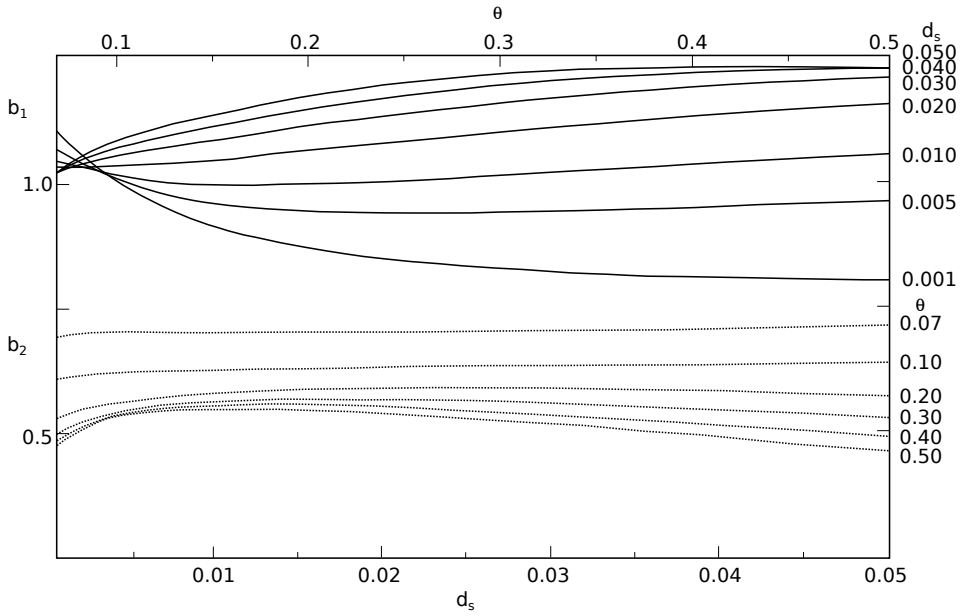

Figure 2.8: Coefficients b_1 and b_2 of the Eq. (2.24). In particular, b_1 is plotted as function of θ for different values of d_s; b_2 is plotted as function of d_s for different values of θ.

it is possible to recall some distinctive features of forced bars in straight channels:

- forced bars are **non-migrating**: there is no migration of forced bars in straight channels;
- forced bars are **longer than free bars**: their typical wavelength range is about $15 \div 20$ times the channel width W (nearly twice compared to free bars);
- the **amplitude** of forced bars **changes in space**: it is damped in the longitudinal direction when only linear effects are accounted for and it also predicts growth in longitudinal direction [*Mosselman et al.*, 2006].

Based on the development of the related theories for straight channels, free bars are bed-forms that migrate and grow in time, while forced bars are steady bedforms with spatially varying amplitude [*Olesen*, 1984]. This

concept is part of the general issue of morphodynamic influence, as it has been stated theoretically by *Struiksma et al.* [1985]; *Zolezzi and Seminara* [2001] and supported experimentally by *Zolezzi et al.* [2005].

The linear theory for forced steady bars in straight channels is formulated with reference to the same system of governing equations (2.4 ÷ 2.7) used to derive the linear free bars theory. The main differences are that (i) steady solutions of the system are sought and (ii) non-periodic boundary conditions are imposed in the streamwise direction, representing the "forcing" effect related to the local persistent perturbation of the channel geometry (bend, local narrowing etc.). Steady conditions imply to set $\partial/\partial t = 0$ in the governing equations (2.4 ÷ 2.7), particularly in the sediment continuity equation (2.7).

2.5.1 Linear theory of forced bars in straight channels

Using an approach similar to the one described in Section 2.4, a small spatial bar perturbation is added to uniform flow solution. In particular, considering the water depth, it takes the form:

$$D\left(x,y\right) = D_0 + \epsilon D_1\left(x,y\right) \ , \tag{2.27}$$

where D_0 is the water depth of the reference uniform flow and $D_1\left(x,y\right)$ represents the functional structure of the first order spatial perturbation, written as follows:

$$D_1\left(x,y\right) = e^{(\lambda_r + i\lambda_i)x} sin\left(\frac{\pi y}{W_0}\right) \ + c.c. \tag{2.28}$$

$$= e^{\lambda_r x} \sin\left(\frac{\pi y}{W_0}\right) \cos\left(\lambda_i x\right) \ + c.c. \tag{2.29}$$

In equation (2.27) ϵ is a small number, requested by linear approach, while λ_r and λ_i are the spatial amplification rate and wavenumber of the steady bars. Eq. (2.29) is written within the same system of coordinates used for free bars (see Fig. 2.1).

It is useful to focus on the mathematical differences between the linear solutions for free migrating bars and forced steady bars. When studying free alternate bars, the most important parameters for bar stability and

migration are Ω and ω (Eq. 2.15): they express how free-bar stability and migration depend on the governing parameters θ, β, d_s for a given λ and transverse mode m. The solution of the linear differential system that is obtained by substituting the linear expansion (2.27) into the steady form of the governing equations (2.4, $\div$ 2.7) yields, in the present case, the dependence of λ_r and of λ_i on (β, θ, d_s) and on the transverse bar mode m. This makes it possible to compute values of λ_r and λ_i fixing θ and d_s and changing β. The solution of the perturbed system are four complex numbers λ_{1-4} and an example of their variability with β is reported in Fig. 2.9.

It is worth noting that several formulations for the steady-bar theory have been proposed in the scientific literature. They are all based on the same set of governing equations and mainly differ for the simplifying hypothesis that have been made to solve them. The key outcomes do not qualitatively differ among these theories [*Olesen*, 1983; *Struiksma and Crosato*, 1989; *Parker and Johannesson*, 1989; *Seminara and Tubino*, 1992]. In some cases, two (instead of four) eigenvalues of the homogeneous differential system are obtained, because of a larger number of terms that is neglected in the equations, which results in a reduced order of the linear differential problem. The two eigenvalues that are obtained within such 2^{nd} order linear mathematical theories correspond to the complex eigenvalues λ_3, λ_4 of the 4^{th} order model that is discussed further in the present chapter and, more in general, that is used and applied in the present thesis. It is worth noting that the additional eigenvalues of the 4^{th} order model with respect to the 2^{nd} order model are always real numbers. The real part λ_r of the complex eigenvalue (Fig. 2.9B) denotes spatial damping rate of steady bars, while the imaginary part λ_i, reported in Figure 2.9C, denotes its wavenumber, as defined in (2.16). More in detail, positive values of the real part denote that bar amplitude decays in the upstream direction, vice versa it decays in the downstream direction. The linear solution of steady bar pattern is composed by the sum of four different complex exponentials of the type $e^{(\lambda_r + i\lambda_i)x}$. Each exponential contributes to the steady bar solution as follows:

λ_1 The first solution has a vanishing imaginary part and a real part always positive: this means that this component of the bed eleva-

tion is non-oscillating and rapidly decaying upstream (or growing upstream).

λ_2 It has the same configuration as λ_1 but negative sign; it means that this component is a non-oscillating signal and quickly decays downstream (or grows upstream).

λ_3 It corresponds to a steady bar with wavelength $(2\pi/\lambda_{3i})$ of about $10-20$ times channel width. The direction along which the amplitude is damped is controlled by the real part of λ_3: for small values of β the amplitude is damped in the downstream direction, while increasing β above the resonant threshold β_R, implies an upstream decaying bar amplitude (or a growth in the downstream direction).

λ_4 It has the same real part as λ_3 and the same absolute values for the imaginary part: the bar "signal" coincides with the previous one (λ_3).

Because of the structure of such a linear solution, the sign of the real part of the characteristic exponents (λ_3, λ_4 see Figure 2.9) control whether, at a linear level, forced bars are expected to appear downstream or upstream the local geometrical perturbation (bend, narrowing,...).

Namely, when $\beta < \beta_{res}$, $\lambda_{3r} = \lambda_{4r} < 0$, forced bars can only occur *downstream* of the local perturbation and their amplitude is downstream damped. An unbounded upstream growth would indeed lead to unrealistic patterns and those solutions are discarded. This is called "2D downstream morphodynamic influence" and linearly occurs under sub-resonant conditions (i.e. $\beta < \beta_{res}$). When β increases, the *resonant* condition is reached, characterized by a theoretical zero-damping of the bar amplitude. Moving in upper region, where $\beta > \beta_{res}$, forced bars are damped in the upstream directions. Following an analogous reasoning, this would imply that forced steady bars, when $\beta > \beta_{res}$, appear *upstream* the forcing discontinuity. This is called "2D upstream morphodynamic influence" and occurs only under super-resonant conditions (i.e. $\beta > \beta_{res}$). In the linear solution, the distance of β from the resonant condition also quantifies the longitudinal distance over which the amplitude of the steady bar is damped. The damping rate of the bar wave is indeed higher far from the resonant

condition, while it is smaller when approaching the resonant condition. The link between the outcomes of forced and free bars theories in straight channels is shown in Fig. 2.9.

It is represented by the resonant point, which corresponds to both marginally stable, non migrating free bars and to non amplifying and non decaying forced steady bars in straight channels. A vertical line is drawn connecting figure 2.9A and 2.9B to clarify such link graphically.

As a final remark, it must be noted that the two families of analytical bar theories for free and forced bars in straight channels likely represent end members of what is actually observed in a field situation, and even in a laboratory flume setting, which is likely related to complex non-linear interactions between these theoretical bar types. Nevertheless, especially for representing purely free or purely forced bar behavior, the theories reviewed in this chapter can be effectively used to benchmark numerical simulations aiming at reproducing the fully non-linear dynamics of alternate bars, e.g. [*Siviglia et al.*, 2013].

2.5.2 Weakly non-linear theory of forced bars in straight channels

Spatial behaviour of forced steady bars can be viewed through an analogy with free migrating bars with two main differences: substituting time with the longitudinal coordinate and the critical parameters (β_c,λ_c) with resonant parameters [*Seminara and Tubino*, 1992]. The analogy is particularly relevant to illustrate the key outcomes of the non-linear theory of steady bars, which exactly coincides with that of the corresponding theory of migrating bars, provided time is replaced by space.

Referring to a semi-infinite straight reach with an upstream local persistent perturbation (Fig. 2.11), under sub-resonant conditions an initial amplitude of steady bars set by the presence of a local discontinuity, decays exponentially downstream by a rate that is proportional to $\lambda_{3r} = \lambda_{4r}$. After a certain length, which is a function of the hydraulic conditions (β, θ, d_s), the straight reach is characterized by absence of steady bars. This behaviour is predicted by both linear and non-linear theories.

On the opposite, under super-resonant conditions, non-linear effects

play a relevant role and modify the linear response. Linear theory predicts an indefinite downstream exponential growth of an initial steady bar amplitude as shown in Fig. 2.12, while non-linear effects limit the growth of bar amplitude towards and equilibrium value in space (Fig. 2.13). The analogous behaviour of free-bar theory (Fig. 2.4.2) is given by the amplitude of migrating bars that grows in time at a rate that is exponential in the initial stages (dominant linear effects) and afterwards is damped by non-linear effects, eventually tending towards an equilibrium amplitude. In forced-bar theory the amplitude of forced bars evolves in the same way when time is replaced by the longitudinal coordinate.

Non-linear analysis, performed by *Seminara and Tubino* [1992] in the neighbourhood of the resonant condition, considers the basic flow properties and the fundamental and second harmonics of the expansion in powers of $\epsilon^{1/2}$. The equilibrium amplitude in space presents the same structure of the amplitude in time of the free bar theory and takes the expression [*Seminara and Tubino*, 1992]:

$$|A_{EQ}| = \sqrt{\frac{-Re\left(\alpha_1^R\right)}{Re\left(\alpha_2^R\right)}} \tag{2.30}$$

where the two parameters α_1^R and α_2^R are functions of (θ, d_s) and can be found in *Seminara and Tubino* [1992] in their Fig. 6 and Fig. 7 for the case of a plane bed and a dune-covered bed, respectively. The weakly non-linear analysis performed by *Seminara and Tubino* [1992] suggests that under super-resonant conditions, the initial steady perturbation (say, A_0) develops asymptotically in space into a periodic equilibrium configuration (say, A_{EQ}) consisting of steady bars. The solution presented in Fig. 2.13 is a qualitative attempt to describe the behaviour of the non-linear effect pointed out by *Seminara and Tubino* [1992]. In Fig. 2.13 the following approximate expression has been used to plot the spatial variability of the bed elevation near one of the banks:

$$\eta\left(x, y, t\right) = \eta_0 + \frac{A_0 e^{\lambda_r x}}{1 + \left(e^{\lambda_r x} - 1\right)\frac{A_0}{A_{EQ}}} sin\left(\frac{2\pi y}{W_0}\right) cos(\lambda_i x)\ . \tag{2.31}$$

The solution of *Seminara and Tubino*, 1992 refers to the ideal case of a straight channel with semi-infinite length in the direction of propagation

of the steady perturbation. In summary, the weakly non-linear theory for forced steady bars in straight channels [*Seminara and Tubino*, 1992] is the analogous of the weakly non-linear theory for free migrating bars, with the difference that the independent variable on which the non-linear amplitude equation depends is space (the streamwise direction x) instead of time, and the threshold β_{cr} is replaced by the threshold β_{res}. Therefore, under sub-resonant conditions ($\beta < \beta_{res}$), forced steady bars occur only downstream the localized perturbation, with downstream decaying amplitude, in analogy with the behaviour of free bars that decay in time when $\beta < \beta_{cr}$. Under super-resonant conditions ($\beta > \beta_{res}$), instead, the amplitude of forced bars varies in space and tends, both upstream and downstream, to an equilibrium amplitude that can be computed by the linear theory of *Seminara and Tubino* [1992]. All the above picture has received experimental support [*Struiksma et al.*, 1985; *Zolezzi et al.*, 2005].

2.5.3 Illustration of steady bar patterns in straight channel reaches with local planform perturbations

A first example is shown in Figure 2.10 in which the case of three straight reaches and two bends is presented. The Figure shows the analytical solution of the linearised system of equations presented before, with different values of a steady flow discharge, uniform sediment diameter, constant channel width and the Meyer Peter and Müller formula [*Meyer-Peter and Müller*, 1948] as bed-load predictor. The channel geometry consists of three straight reaches connected by two bends of constant radius. To save space, the bed morphology in the bends is not plotted in the diagrams of Fig. 2.10, and the bends are ideally located at $x = 50$ and $x = 150$ (numbers of channel width). Each bend is one channel width long and its radius of curvature is 10 times the channel width (5.73 degrees).

At the interface between straight and curved sub-reaches, four conditions have been imposed to match the upstream and downstream solutions on both parts of the interface. In particular Figure 2.10 presents the planform configuration of three single straight reaches in which the length of the upstream and the downstream ones is equal to one half of the central

one. Longitudinal and transverse lengths are nondimensional, in particular $x = x^*/W^*$ and $y = y^*/W^*$. Figure 2.10 shows the first three cases in which $\beta > \beta_r$ and the last two cases in which $\beta < \beta_r$. In fact, in channels where channel width almost does not vary with flow discharge, the aspect ratio β decreases with increasing discharge, while the opposite applies for the resonant value β_r. This is obtained changing the value of the dimensional discharge, so changing the value of θ. Observations of the various diagrams in Fig. 2.10 suggests different behavior:

- length of the influence is maximum when $\beta - \beta_r$ is nearly vanishing, while it is shorter when $\beta - \beta_r$ is larger;
- in the linear case, we have only upstream influence in super-resonant conditions and only downstream influence in sub-resonant conditions;
- amplitude and wavelength of the alternate bars are proportional with the length of the influence: a longer influence corresponds to higher amplitude and bar wavelength;

Moreover, linear analysis is not able to capture the alternate bars commonly present downstream of an obstacle like a bend, even under sub-resonant conditions.

In view of the comparison with a field case (see Chapter 3), a second example is presented considering reaches with finite length separated by fixed perturbations (physically planform discontinuities e.g. bends) that trigger the formation of steady bars in space. The geometrical configuration of the channel is analogous to the one of Fig. 2.10. The effect of two perturbations of the same type (e.g. two bends that generate the same effect in terms of amplitude A_0) is shown in Fig. 2.14 and 2.15 for the sub-resonant case and for the super-resonant case respectively. The solutions of the two perturbations are superimposed to obtain the combined effect in the streamwise direction. The role of non-linearity is fundamental to analyse a reach with multiple discontinuities, because it corrects the streamwise exponential growth, and determines the amplitude of bed oscillations to achieve an equilibrium amplitude provided enough channel length is available. In Figure 2.16 the linear and non-linear solution of

the sub-resonant (upper and central) and super-resonant (lower) cases are shown. In particular, the effect of the non-linearity is evident by comparing plots in Fig. 2.16A,B where the linear super-resonant solution indefinitely grows in the longitudinal coordinate, with the plot in Fig. 2.16C, where non-linear effects cause the solution to tend to the equilibrium value A_{EQ}.

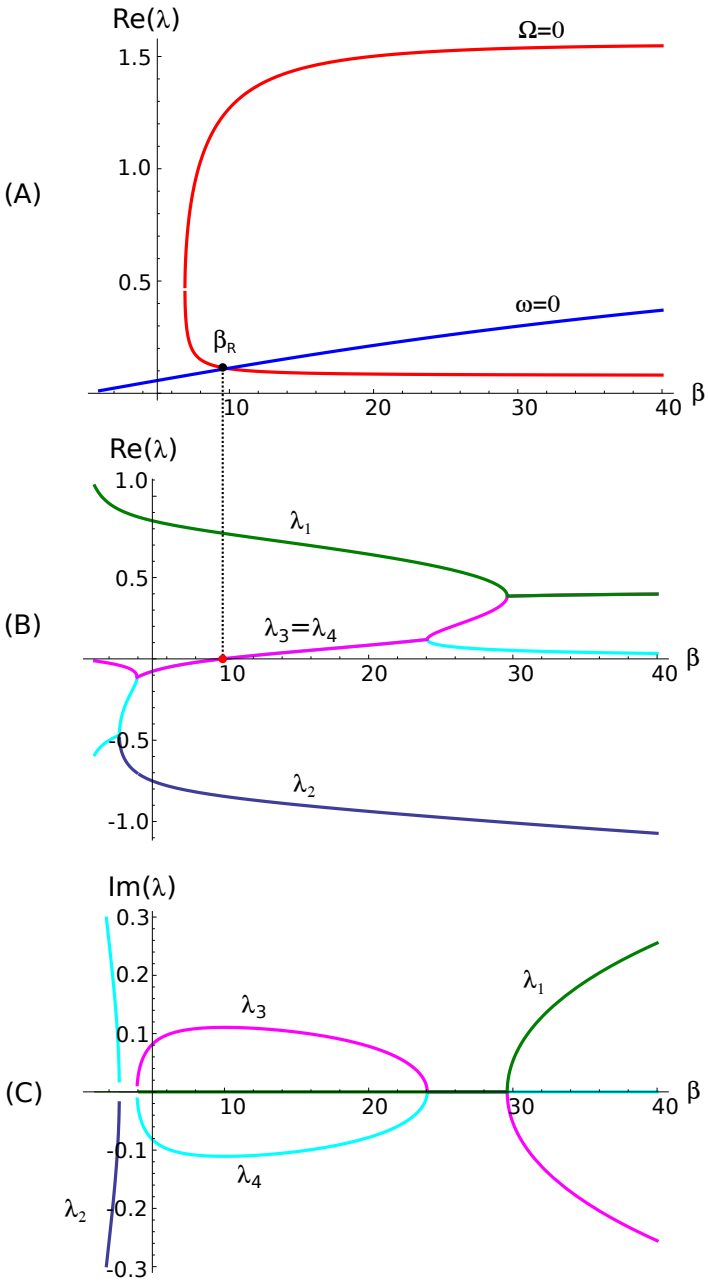

Figure 2.9: (A) Marginal curves for free bar stability ($\Omega = 0$, red line) and migration ($\omega = 0$, blue line). (B) Spatial damping rates (real part of λ_1, ..., λ_4) of steady bars. (C) Dimensionless wavenumber (imaginary part of λ_1, ..., λ_4). All diagrams refer to the same combination of parameters ($\theta = 0.1, d_s = 0.02$, Parker bed-load formula, $r = 0.3$), therefore the value of β_{res} is the same in diagrams A and B. *Courtesy of M. Redolfi.*

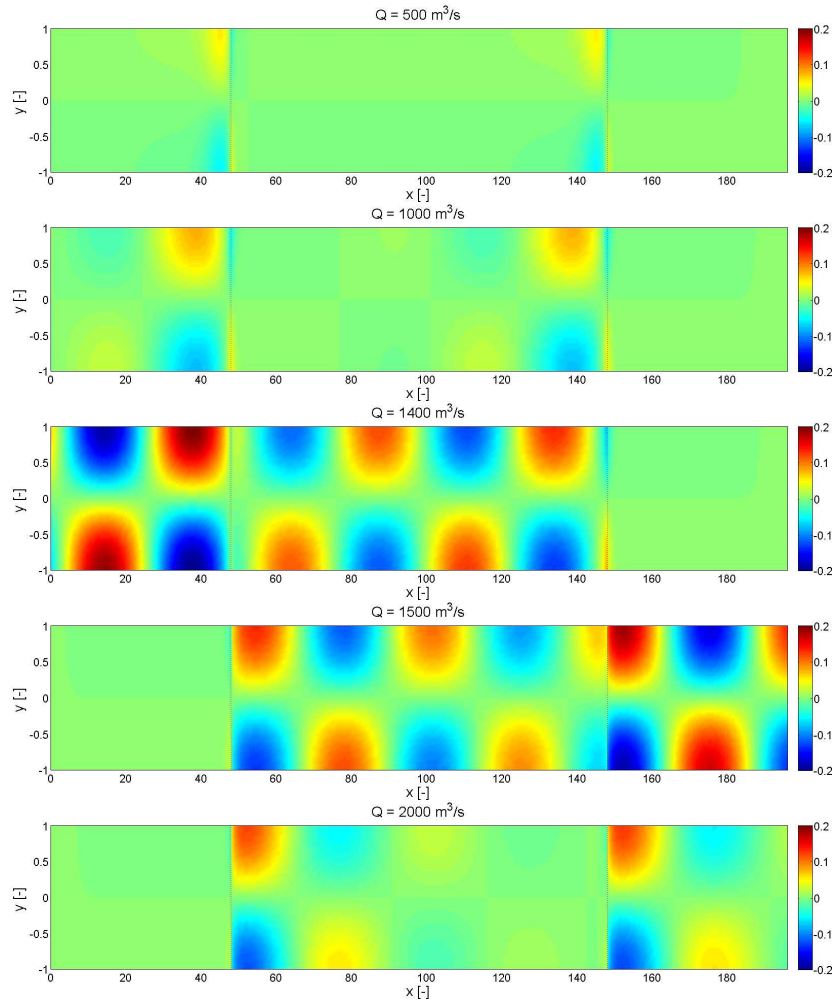

Figure 2.10: Theoretical case of three straight channels linked by two obstacles (two bends: vertical dotted lines). Forced alternate bars formation is shown in five different cases of flow discharge under constant channel width. The first three cases describe the super-resonant regime in which steady bars form upstream the obstacles, the last two cases describe the sub-resonant regime, in which steady bars form downstream the obstacles.

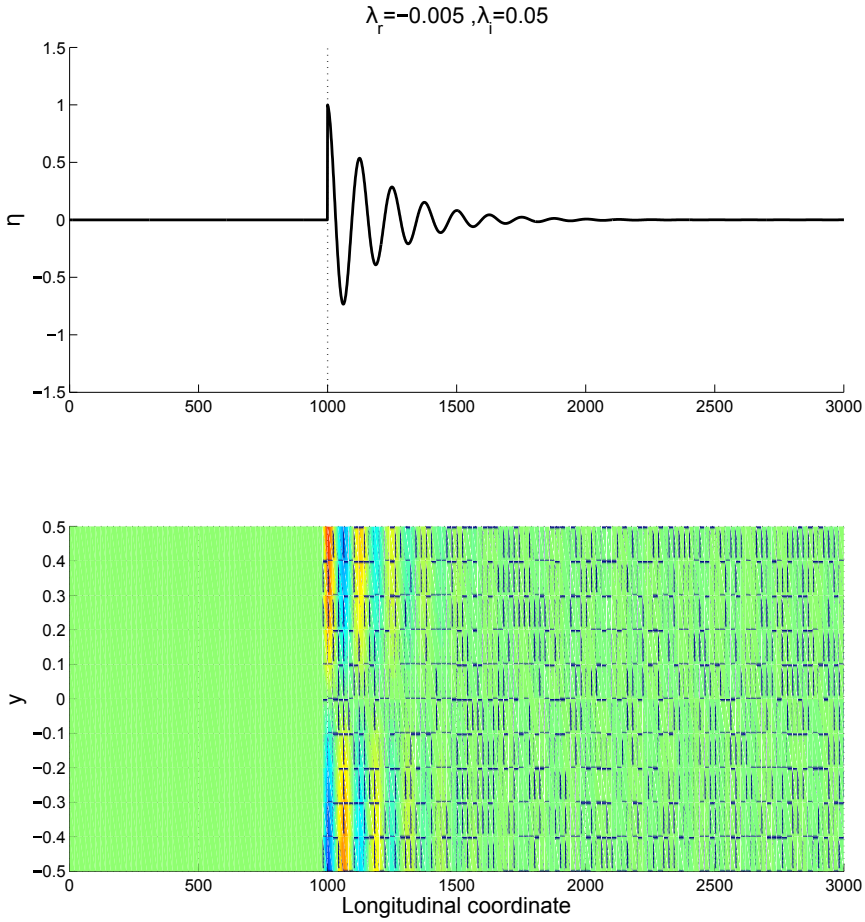

Figure 2.11: Sub-resonant case ($\lambda_r < 0$) of a fixed perturbation located at $x = 1000$ that generates and amplitude $A_0 = 1$. Real and imaginary wavelength are respectively $\lambda_r = -0.005$ and $\lambda_i = 0.05$. Upper figure shows the bed elevation η function of the longitudinal coordinate, downer figure shows the planform evolution of the same case, with color-bar ranging $\eta = [-1.5; 1.5]$.

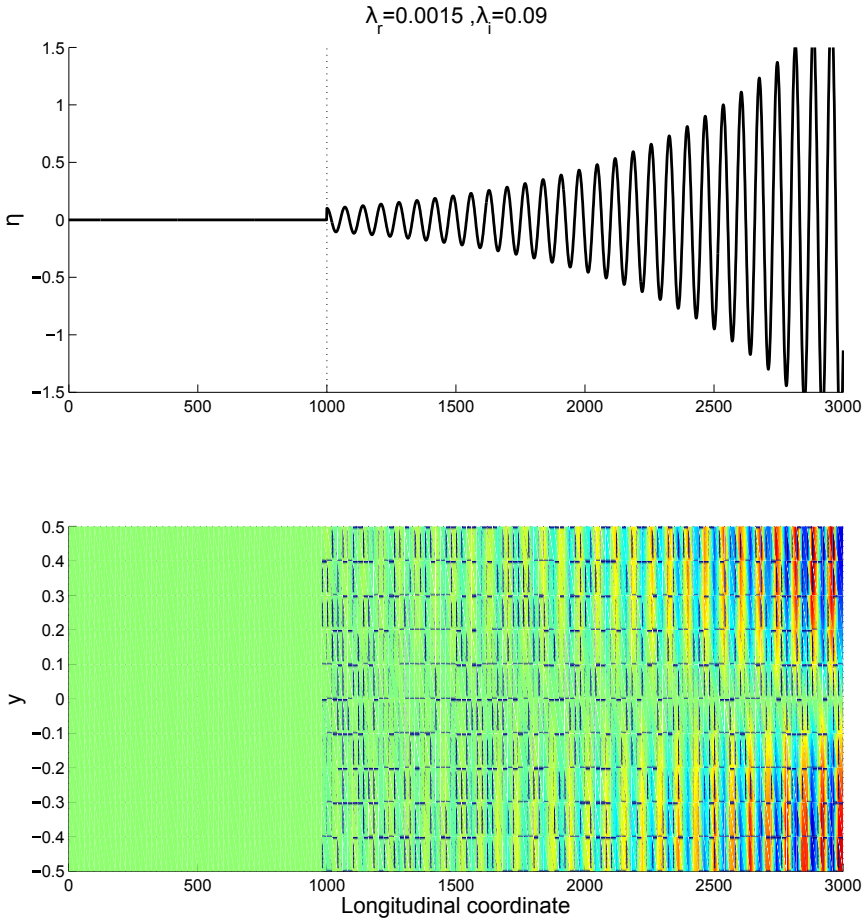

Figure 2.12: Super-resonant case ($\lambda_r > 0$) of a fixed perturbation located at $x = 1000$ that generates and amplitude $A_0 = 0.1$. Real and imaginary wavelength are respectively $\lambda_r = 0.0015$ and $\lambda_i = 0.09$. Upper figure shows the bed elevation η function of the longitudinal coordinate, downer figure shows the planform evolution of the same case, with color-bar ranging $\eta = [-1.5; 1.5]$.

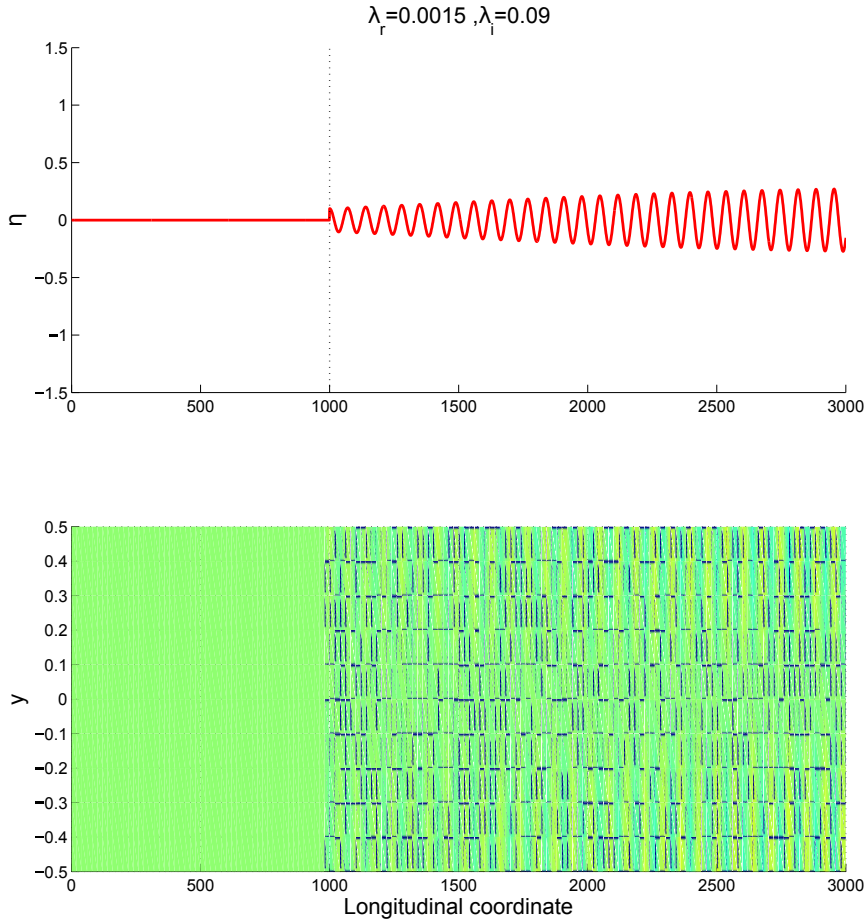

Figure 2.13: Super-resonant case ($\lambda_r > 0$) of a fixed perturbation located at $x = 1000$ that generates and amplitude $A_0 = 0.1$ in which the linear exponential growth is substituted with a non-linear growth up to the equilibrium value $A_{EQ} = 0.3$. Real and imaginary wavelength are respectively $\lambda_r = 0.0015$ and $\lambda_i = 0.09$. Upper figure shows the bed elevation η function of the longitudinal coordinate, downer figure shows the planform evolution of the same case, with color-bar ranging $\eta = [-1.5; 1.5]$.

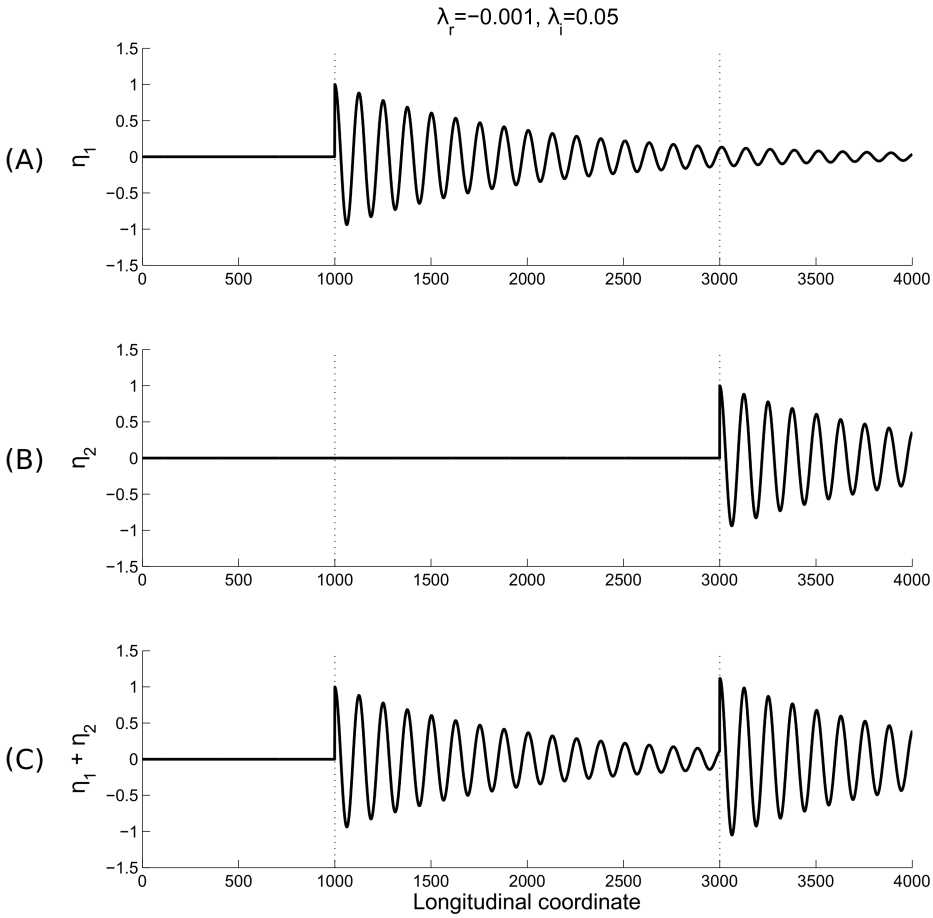

Figure 2.14: Illustrative diagram of the linear solution of the dimensionless bed elevation η corresponding to two fixed perturbations connecting three straight reaches under *sub*-resonant conditions. Solutions of the single perturbations (η_1 and η_2) are shown plots (A) and (B). Plot (C) shows the combined effect ($\eta_1 + \eta_2$) of the perturbation in the finite length straight reach.

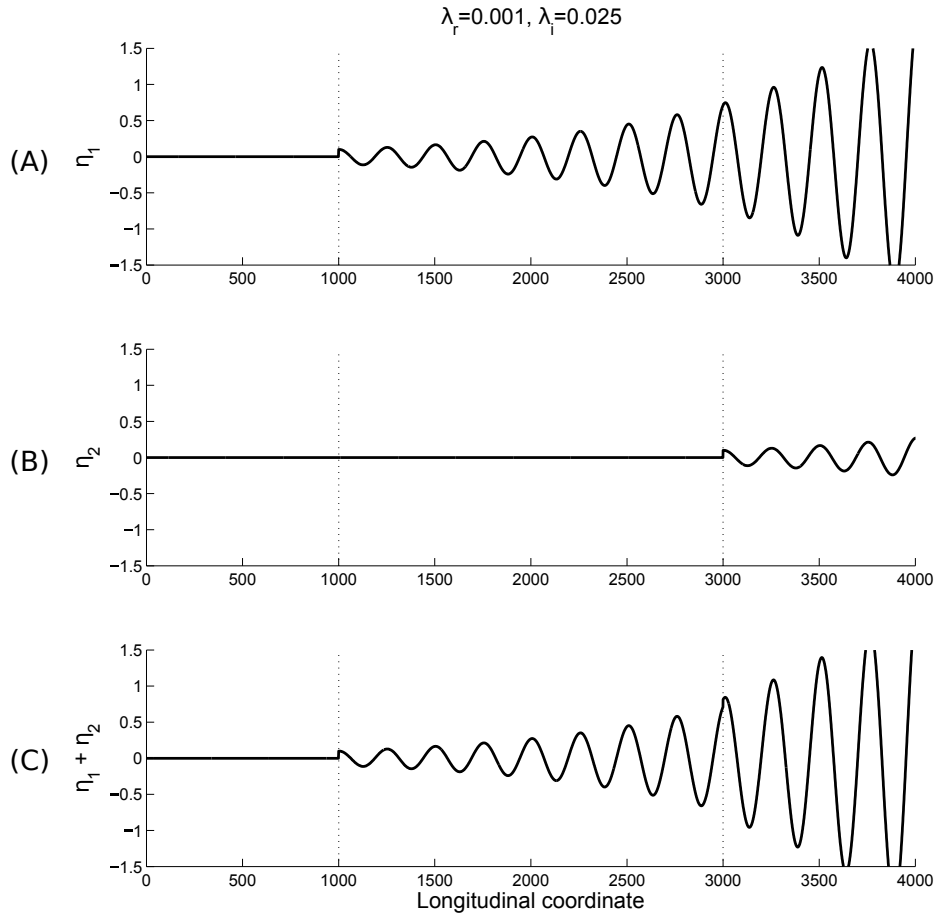

Figure 2.15: Illustrative diagram of the linear solution of the dimensionless bed elevation η corresponding to two fixed perturbations connecting three straight reaches under *super*-resonant conditions. Solutions of the single perturbations (η_1 and η_2) are shown plots (A) and (B). Plot (C) shows the combined effect ($\eta_1 + \eta_2$) of the perturbation in the finite length straight reach.

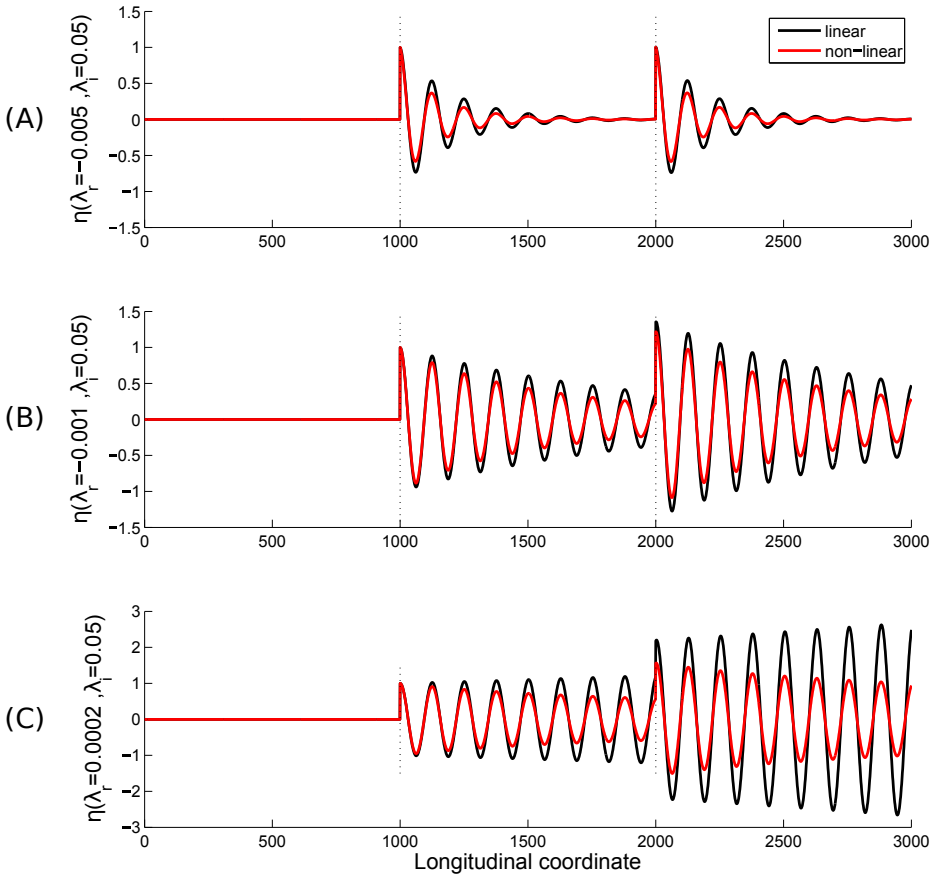

Figure 2.16: Illustrative comparison of the linear and non-linear solutions for the dimensionless bed elevation η both *sub*-resonant (A,B) and *super*-resonant conditions (C). Channel geometry is analogous to that of Fig. 2.14 and Fig. 2.15.

Chapter 3

Multi-decadal alternate bar dynamics of the Alpine Rhine river

Based on the paper: Adami L., Bertoldi W., Zolezzi G., Multi-decadal dynamics of alternate bars in the Alpine Rhine River. Water Resources and Research, under review.

This chapter reports on a multi-decadal analysis of alternate bars dynamics in a 41.7 km reach of the Alpine Rhine River, which represents an almost unique example of a regulated river composed by fixed levees, straight reaches and regular bends in which alternate gravel bars spontaneously form and migrate since more than a century. The analysis is based on freely available Landsat imagery, which provides an accurate and frequent survey of the dynamics of alternate bar configuration since 1984. Bars are characterized in terms of wavelength, migration, and height. Longitudinal and temporal patterns are investigated as a function of flood occurrence and magnitude and in relation to the presence of local planform discontinuities (bends and ramps) that may affect their dynamics. The study shows spatially selective behavior of alternate bars, with longer (about 13 channel widths) steady bars more common in the upper reach and shorter (about 9 channel widths) migrating bars observed in the downstream reach. Bar height is rather uniform along the reach,

ranging between 3 m and 4 m. The observed relation between bar migration and wavelength is consistent with linear theories for free migrating and steady forced bars in straight channels. Observed characteristics show intermediate values between the theoretical boundaries of linear theories. Overall, the analysis provides observations on the morphodynamics of alternate bars in channelized river reaches at an unprecedented combination of length scale, time scale and time resolution. The outcome of the analysis improves the present understanding of alternate bars behavior in regulated rivers and provides a valuable dataset for comparison with complementary approaches to the study of alternate bars, like analytical theories and numerical morphodynamic modelling.

3.1 Introduction

Alternate bars have been documented in channelized river reaches since nearly 3 centuries (e.g *Engels* [1914], *Werth* [2014]). They emerged as a morphological response of the river bed to levee construction and channel straightening. Their widespread occurrence in wide enough, morphologically regulated streams attracted the attention of hydraulic engineers because of their undesired effects on bridges, embankments, intake structures and on river navigation [*Jäggi*, 1984]. Moreover the weakly, regular periodic oscillations that alternate bars impose to the flow in a straight channel initially provided an intriguing (though lately discarded for the case of free bars) possible explanation to the origin of river meandering [*Parker*, 1975; *Lewin*, 1976], thus stimulating the interest of fluvial geomorphologists.

In the 1960s, a consistent research effort to understand the causes and controls on their formation, their geometrical properties (length, magnitude of scours and deposits), and migration was undertaken, through complementary approaches, mainly including mathematical and physical scale modeling. A remarkable bias towards modeling approaches is evident in the alternate-bar literature, with limited availability of field observations till recently, mainly because of the relatively long time and space scales needed to properly describe their dynamics (e.g., *Eekhout et al.* [2013]). Such bias limits our present understanding of and ability to predict the

morpho-dynamic response of regulated rivers to hydromorphological pressures, like those associated with changes in the flow and sediment supply regime, in levee alignment, and with other river management or restoration measures.

The observation gap is being increasingly addressed only very recently, thanks to the development of in-situ monitoring technologies e.g., flow and bathimetric survey, (*Rodrigues et al.* [2015]), as well as through remote sensing and the use of satellite imagery (*Henshaw et al.* [2013]). Table 3.1 summarizes the main existing field studies with focus on alternate-bar dynamics. Three studies out of eight (*Welford* [1994]; *Eekhout et al.* [2013]; *Jaballah et al.* [2015]) focus on a reach length of nearly 100 channel widths or more, allowing the observation of a consistent number of alternate bar units, which length is typically in the range of 6 to 30 channel widths. However, only one of these three (*Jaballah et al.* [2015]) covers a multi-decadal time scale, with the other two multi-decadal studies referring to reaches with a more limited number of bars (*Church and Rice* [2009], *Ferguson et al.* [2011]). Furthermore, the three multi-decadal analyses have a relatively poor temporal resolution of surveys, with an average of 1 available survey every 3 to 5 years.

The present chapter focuses on a quantitative understanding of long-term dynamics of alternate bars in the Alpine Rhine River. This is a renowned example of a channelized stream where an impressively long and regular sequence of alternate bars is observed since decades (*Jäggi* [1984]). Moreover, it is believed to be one of the few examples of rivers where migrating alternate bars can be observed (*Crosato and Mosselman* [2009]).

The main goal of this chapter is to quantify the morphodynamics of alternate bars in the Alpine Rhine River, with a particular emphasis on bar migration; This goal is achieved by developing and analyzing a dataset of freely available multitemporal Landsat imagery, which combine unprecedented temporal length (3 decades); spatial length (> 400 channel widths); and temporal resolution (~ 2 images per year).

Table 3.1: References, geometric and hydraulic data of the main field studies reported in the literature.

Authors	River	d_{50} [mm]	s [m/km]	W [m]	Q_{mean} [m^3 s^{-1}]	L_R [km]	n_{bars} [-]	ΔT [year]
Lewin [1976]	Ystwyth (UK)	0.7 – 42	3.7	36	5.5	0.5	4	2
Welford [1994]	Embarras, Illinois (US)	0.53	0.6	12	0.1	4	-	0.25
Church and Rice [2009]	Lower Fraser, British Columbia (Canada)	17 – 53	0.48	1000 – 2000	3410	50	20	51
Ferguson et al. [2011]	Vedder Canal, British Columbia (Canada)	12 – 35	2 – 5	100 – 240	67	4.7	9	57
Rodrigues et al. [2012]	Loire (France)	0.83	0.25	145 – 200	850	3	2	2
Zolezzi et al. [2012]	Tagliamento (Italy)	40	3.6	840	1400	3	braided	5
Eekhout et al. [2013]	Hooge Raam (The Netherlands)	0.218	0.18	7.5	0.22	0.6	6	3
Jaballah et al. [2015]	Arc (France)	80	6 – 11	35 – 50	12	8	10	30
Rodrigues et al. [2015]	Loire (France)	0.83	0.25	145 – 200	850	3	2	2
present work	Alpine Rhine (Switzerland-Austria)	20 – 60	1.3 – 2.9	86 – 106	230	41.7	80	30

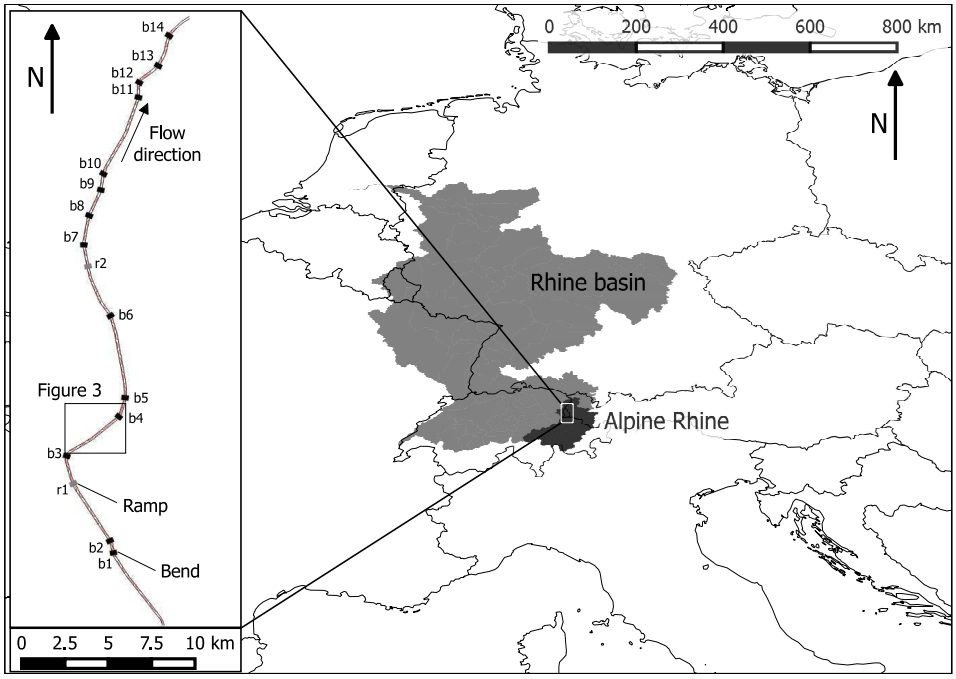

Figure 3.1: Overview of the study area with the catchment of the Rhine River in light gray and the catchment of the Alpine Rhine highlighted in dark gray. On the left panel there is a zoom on the study reach, reporting on the location of bends and ramps.

3.2 Study site and methods

3.2.1 The Alpine Rhine River

The Rhine river is one of the largest rivers of Europe, with a basin of $1.85 \times 10^6\,\mathrm{km}^2$ and a length of 1326 km. The upper part of the basin, between the confluence of Anterior Rhine and Posterior Rhine and the lake of Constance is called Alpine Rhine. This sub-basin is located in the eastern part of Switzerland, western Austria (the tributary Ill) and the whole territory of Liechtenstein (see Figure 3.1). The Alpine Rhine is 93 km long and its catchment area is $6123\,\mathrm{km}^2$.

We focused the analysis on a reach that is 41.7 km long and is located between the Landquart's confluence (km 23.3 of the Alpine Rhine, Landquart's drainage area: $618\,\mathrm{km}^2$) and the confluence with the Ill river

(km 65.0, Ill's drainage area: 1281 km^2). The whole reach was heavily channelized in the 19^{th} and 20^{th} centuries, with the last levees built in the 30s and 40s of the last century. These engineering works aimed at an increased flood protection and drastically simplified the original dynamic multi-channel morphology. Nowadays, the reach is characterized by a continuous sequence of alternate bars, which makes the Alpine Rhine the perfect site to study this morphological pattern.

The hydrological regime is pluvio-nival, characterized by snow-melt in spring and summer and by larger floods most probable in Autumn. The river is strongly affected by hydro-power production, with water release fluctuations superimposed along the whole year. Hydropeaking increases the discharge on average by 70-80 m^3s^{-1}, with a regular daily (and weekly) pattern. Since 2010, the pattern is much more irregular, due to new rules of the energy production management.

There are several available hydrometric stations in this reach. We used the daily data of the Austrian gauging stations in Bangs, Feldrik, and Lustenau for the period 1951 - 2010, and of the Swiss station in Diepoldsau for the period 1919 - 2012. For this last station, 10-min data were also available for the period 1984-2013. The average discharge upstream of the Ill's confluence is 150 m^3s^{-1} (dataset 1996-2010). The minimum flow is 40.3 m^3s^{-1} and the maximum registered flood peak (1988) is 2650 m^3s^{-1} (see Figure 3.2).

The cross-section of the channelized reach was designed with a classical trapezoidal shape, with a base width (W) that increases from 85 m in the upstream part up to 106 m downstream. No floodplain is present and the levees (with a transverse slope of approximately 35°) are composed of boulders that prevent any planform changes. Bed material is primarily composed of gravel, with a median grain size ranging between 60 mm upstream and 20 mm downstream [*Hunziker et al.*, 2001], with local variability caused by the alternate-bar grain sorting. Longitudinal bed slope decreases along the reach, from 2.9 ‰ upstream, to 1.3 ‰ downstream. *Hunziker et al.* [2001] suggested an annual sediment transport load in the range 1.7×10^4 m^3year^{-1} to 6.5×10^4 m^3year^{-1}. In order to take into account the downstream variation of the main morphological parameters, the study reach was divided into three sub-reaches, each having rather

homogeneous values of width, slope and median grain size (see Table 3.2).

3.2.2 Image database

The Landsat program started formally in 1972 with the launch of the first satellite Landsat 1 and represents the world's longest continuously acquired collection of multi-spectral images of the earth surface. This dataset provides an invaluable source of information for the study of several earth-surface processes, including large rivers, for which the 30 m spatial resolution (improved to 15 m in 1999 with Landsat 7) is often adequate (*Henshaw et al.* [2013], *Constantine et al.* [2014]).

Landsat imagery is freely available from the USGS Earth Explorer portal (http://earthexplorer.usgs.gov/). For this study, we used the available images acquired by Landsat 4-5 TM (30 m resolution), Landsat 7 ETM+ and Landsat 8 OLI (15 m resolution of the panchromatic band). The dataset covers a period of around 30 years, starting from 1984, with a partial interruption of the acquisition between 1991 and 1998. A total number of 58 images out of 78 available were downloaded and used for this study. Cloud cover and high discharge are the two main reasons for the filtering.

Figure 3.2 shows the temporal sequence of the available images, superimposed on the discharge record. Emerged gravel bars are visible on the Landsat images only for discharge values lower than $350\,m^3s^{-1}$. The full dataset of 78 images covers a discharge range from $64\,m^3s^{-1}$ to $540\,m^3s^{-1}$. Figure 3.3 shows three examples of Landsat images, taken at different discharges. The mirror alignment problem that affected Landsat 7 ETM+ sensor after 2003 (and produced the black strips visible in Figure 3.3b) did not affect our analysis in a significant way, as it was generally possible to locate the front and tail of most of the bar units. Furthermore, a more detailed aerial image (Google Maps ©) was used to accurately define the embankment line and the low-flow channel width (W).

3.2.3 Bed topography database

We used a complete cross-section dataset of the Alpine Rhine surveyed in 2005 by the IRR (International Rhine Regulation) to determine hydraulic

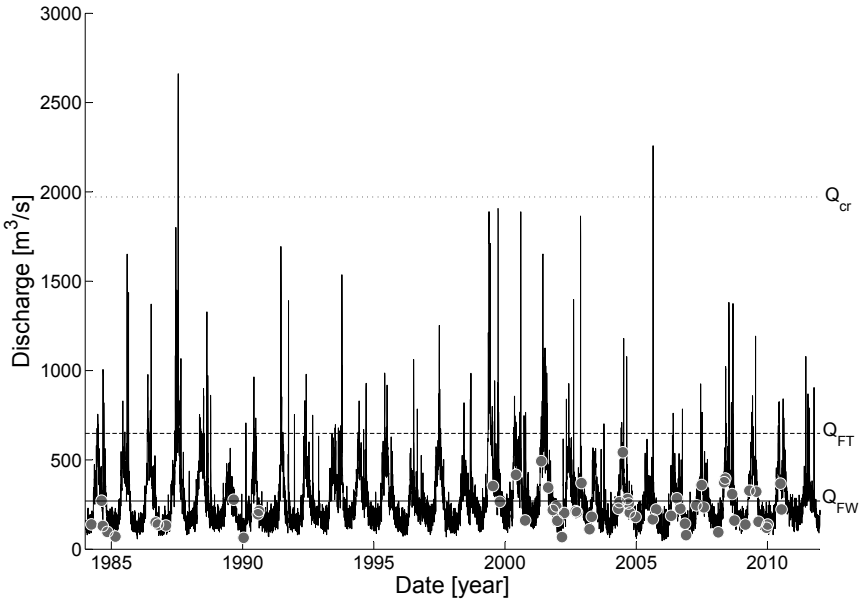

Figure 3.2: Discharge record for the period 1984-2012. Circles represent acquisition date and corresponding discharge value of the analyzed Landsat imagery. Horizontal lines indicate the fully wet discharge Q_{FW} (continuous line); the fully transporting discharge Q_{FT} (dashed line) and the critical discharge for alternate bar formation following *Colombini et al.* [1987], Q_{cr} (dotted line). See Table 3.2 for further details.

variables of the study reach. The survey is composed of more than 200 cross sections with a longitudinal spacing of approximately 200 m. Reach-averaged hydraulic conditions were determined for each of the three sub-reaches, as reported in Table 3.2.

Uniform flow conditions were computed in each cross section, considering a Manning coefficient for roughness in the range 0.025 - 0.030 $\mathrm{sm}^{-1/3}$, and the sub-reach averaged longitudinal slope. The analysis identified: i) the value of discharge that submerges all the bar deposits (fully wet discharge, Q_{FW}, equal to an average of 300 $\mathrm{m}^3\mathrm{s}^{-1}$); and ii) the discharge at which the full cross section is expected to actively transport bed material as bed load (fully transport discharge, Q_{FT}, equal to an average of 650 $\mathrm{m}^3\mathrm{s}^{-1}$). Transport conditions were evaluated considering a threshold

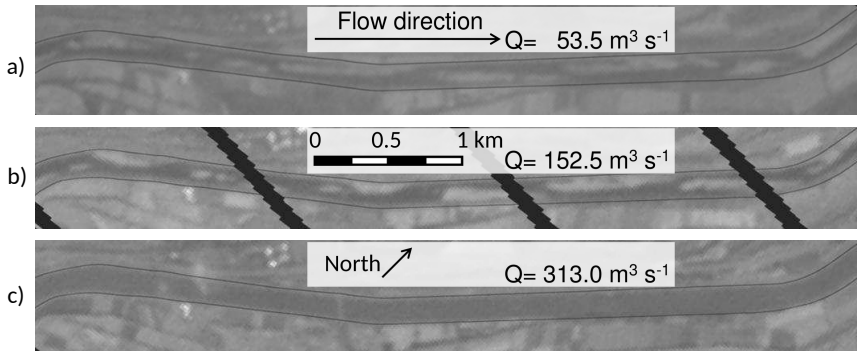

Figure 3.3: Three examples of Landsat images acquired at different flow stages. a) March 04, 2002, Q = 53.5 m^3/s; b) July 21, 2006, Q = 152.5 m^3/s; c) May 01, 2000, Q = 313.0 m^3/s;

on the dimensionless bed shear stress equal to 0.03 [*Parker et al.*, 2007].

3.2.4 Monitoring of bar properties

The 41.7 km long reach includes a series of approximately 40 bar units. Here we define bar unit as two consecutive bar deposits, one on the left and one on the right side. Satellite images were imported into Quantum GIS software (*QGIS Development Team* [2009]) and locations of bar fronts and tails were monitored in each of the 58 available images as the most downstream and upstream point of the emerged deposits. Figure 3.4 reports an example of the resulting vector map of the alternate bars. From this dataset of geographical coordinates, bar wavelength (L^*) and bar migration were computed. Bar wavelength is defined as the distance between two consecutive fronts (or tails) on the left (or right) bank (length of the

Table 3.2: Geometrical and hydraulic properties of the three sub-reaches of the Alpine Rhine. W^* is channel width, d_s^* a representative sediment diameter, s longitudinal slope, Q_{FW} is the fully wet discharge, Q_{FT} the fully transporting discharge, Q_{cr} the critical discharge for bar formation, following *Colombini et al.* [1987].

	Position	Geometry			Discharge		
Reach	from - to [km]	W^* [m]	d_s^* [mm]	s [‰]	Q_{FW}^* [m^3 s^{-1}]	Q_{FT}^*	Q_{cr}
Upstream	0.00 - 12.27	85	60 - 50	2.9	381	829	1845
Center	12.27 - 30.94	95	50 - 30	2.0	270	628	1942
Downstream	30.94 - 41.7	106	30 - 20	1.3	230	511	1880

bar unit). Bar migration is the temporal difference between the location of the front (or tail) of the same bar unit. A parameter called bar elongation was also computed as the wavelength difference of the same bar unit between two different Landsat images. Reference Landsat data for the difference in time are October 22, 1999 (Q= 149 m^{3}s^{-1}) and July 16, 2010 (Q= 154 m^{3}s^{-1}).

The high temporal resolution of the Landsat imagery ensured an easy recognition of the same bar structures on the images. Bars migrated no more than a few hundred meters (i.e. a few channel widths) even during the largest floods and we never observed a complete rearrangement of the bed topography, with disappearance of the bar structure and formation of a new sequence.

In the case of images acquired with largely different discharge conditions, locations of bar fronts and tails are affected by changes in the exposed area. This implies that the front (or tail) of the bar may appear to move upstream (or downstream) only because of a different water level. In order to minimize this effect, we performed a spatial average, combining front and tail results. A change in the water level is likely to determine an opposite movement of fronts and tails, thus resulting in a minimal effect on the bar average [*Adami et al.*, 2014].

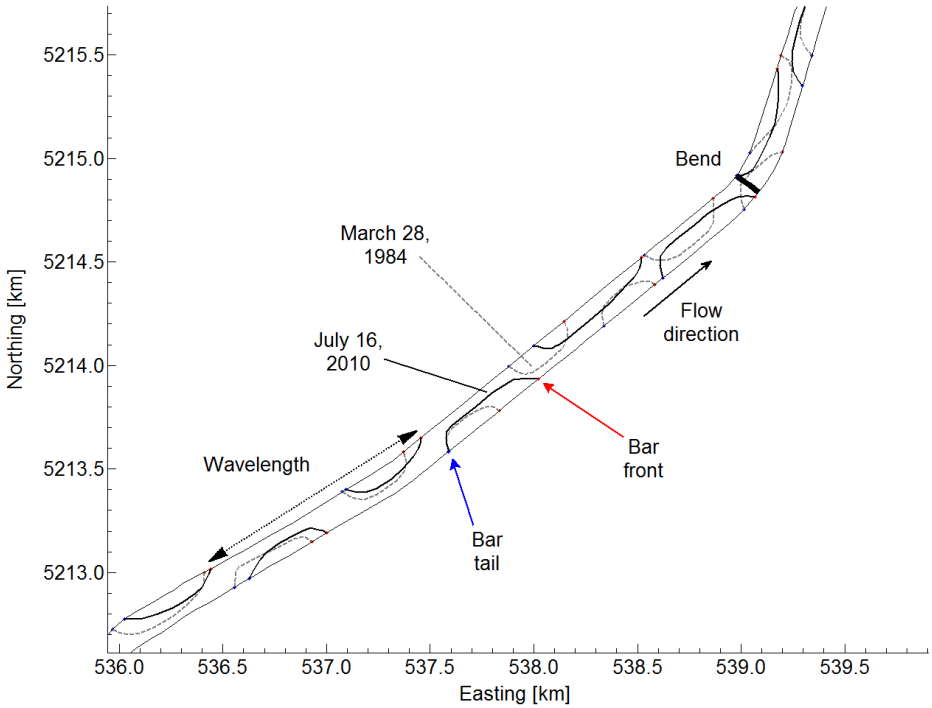

Figure 3.4: Example of digitized bars of a short reach, pointing out location and definition of bar fronts, bar tails, and bar wavelength. Dotted lines represent digitized bars of LANDSAT L4-5 TM, March 28, 1984, Q= 127 m^3s^{-1}; solid lines represent LANDSAT L7 ETM+, July 16, 2010, Q= 154 m^3s^{-1}.

Furthermore, we identified the presence of planform and bed elevation discontinuities, in the form of bends and ramps. Their location was marked in the vector map (see Figure 3.1 and Figure 3.4), in order to assess their potential impact on bar morphodynamics.

The cross-section dataset provided also information about bar amplitude, which is defined for each bar unit as the difference between the highest and the lowest bed elevation values over the entire unit. The relatively coarse longitudinal spacing between consecutive cross-sections in the available topographic survey (200 m) did not allow an exact computation of such parameter. For this reason, a parameter called "bar height" was computed as the difference between the lowest and the highest values of bed elevation in each cross-section. This bar height provides a reasonable, though underestimate, estimate of the actual bar amplitude, as the

highest and lowest bed elevation values over one entire bar unit may not occur at the same cross-section.

3.3 Results

Results of the Landsat imagery analysis are presented here in terms of bar wavelength, migration, and amplitude with focus on the longitudinal and temporal variations.

3.3.1 Bar wavelength

Bar wavelengths along the whole 41.7 km reach of the Alpine Rhine river are shown in Figure 3.5 for the period 1984-2013. Here, each point represents the wavelength of a single bar unit, as measured on one of the Landsat images. The presence of fourteen bends ($b_1, \ldots, b_{14}$) and two ramps (r_1, r_2) along the reach is highlighted in Figure 3.5 by dashed and continuous lines, respectively.

Overall bar wavelengths range in the interval 750 - 1700 m, which corresponds roughly to an interval 7 - 17 in terms of the wavelength normalized with the average channel width. Based on bar wavelength values, the study reach can be divided into two main sectors. In the upstream sector, which extends down to km 16 (bend 4), bars tend to be longer, with wavelengths in the interval 1200 - 1700 m (L/W = 12 - 17). Large fluctuations of the locally averaged wavelength are present along this first sector, with minimum values occurring close to the localized persistent planform discontinuities, as bend b_1 and b_2, and the first ramp r_1.

A sudden shortening is visible starting from bend 4, and shorter bars occur throughout the sector, with wavelengths generally in the interval 700 - 1200 m (L/W = 7 - 12). The local bar wavelength shows a more uniform spatial trend on average, but with a higher number of outliers, with bars as short as 500 m and longer than 1700 m. Overall, the mean behavior of the data cloud in Figure 3.5 appears to vary rather smoothly within the straight sub-reaches, while the presence of ramps, individual sharp bends, or sequences of nearly consecutive bends, is often associated with discontinuities in the spatial trend, inducing local elongation/shortening

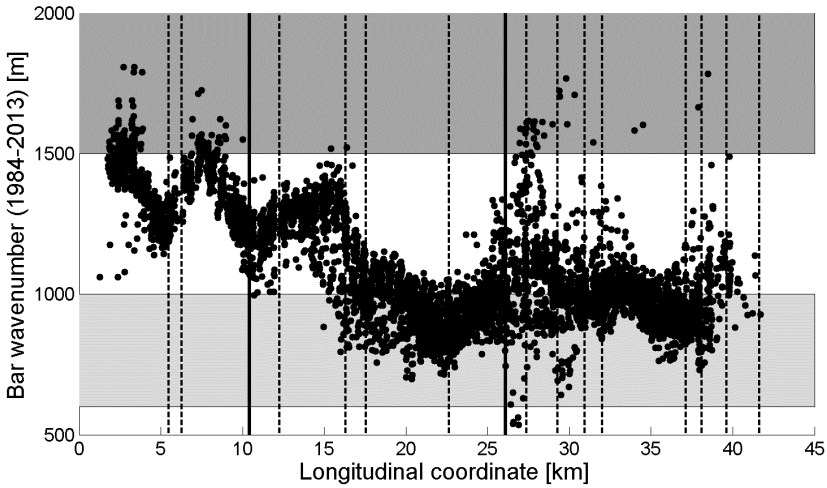

Figure 3.5: Bar wavelength of each monitored bar unit on the complete Landsat imagery dataset (1984-2013). Vertical lines represent bends (dashed) and ramps (continuous). The light grey area represents the theoretical wavelength range of free bars, while the dark grey area represents the theoretical range of forced bars.

of bars.

The local variability of alternate-bar wavelength in the 16 straight reaches is illustrated by the box and whisker plots of Figure 3.6. The whiskers have been computed as the limits of an interval extending $\pm 2.7\sigma$ from the median value of every sub-reach, with σ denoting the standard deviation of the local distribution. Besides the difference in median wavelength values that is evident also in Figure 3.5, the upstream and downstream sectors also show a different behavior between the 6 longer (1.9 - 5 km) and the 11 shorter straight reaches. Bar wavelength shows a much higher local variability in the three longer sub-reaches located in the upstream sector compared both to the shorter sub-reaches located in the same upstream sector and to the three longer sub-reaches located in the downstream sector. The opposite behavior occurs in the downstream sector, where the highest variability in local bar wavelength is observed in the short straight reaches located in between bends. Local wavelength variability in sub-reaches 2, 9, and 15 is the largest, with wavelengths that may differ up to 500 m.

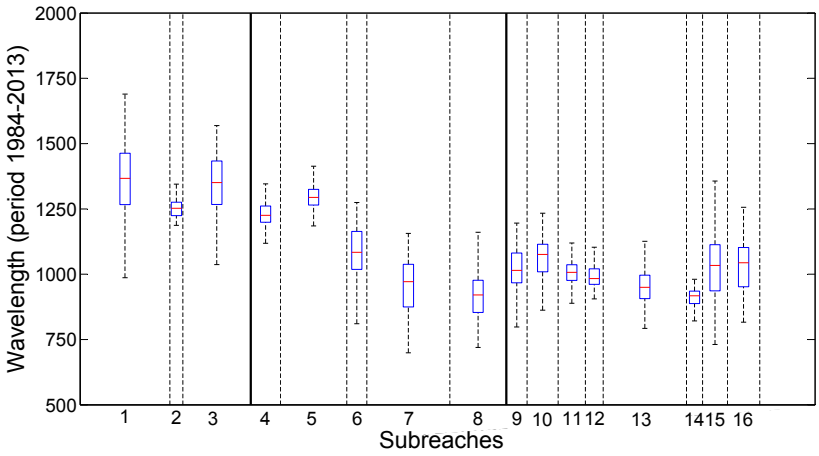

Figure 3.6: Boxplot of bar wavelength, divided in the 16 sub-reaches defined by bends (dashed lines) and ramps (continuous lines).

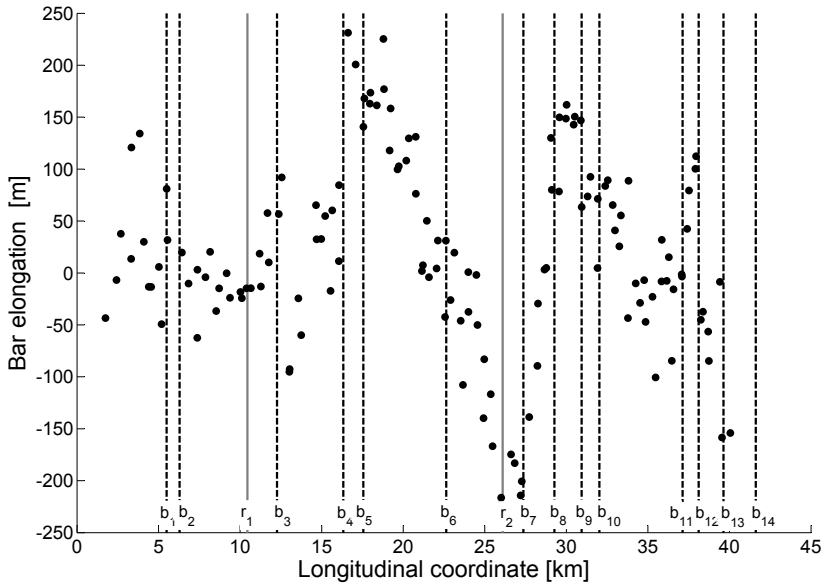

Figure 3.7: Bar elongation in the period 1999-2010. Longitudinal coordinate refers to bar fronts in 1999. Vertical lines represent bends (dashed) and ramps (continuous).

Cumulative values of bar elongation are reported in Figure 3.7, where the difference between values in the period 1999 - 2010 is shown. We chose to limit the analysis to this period, to avoid the long gap between 1990 and 1999, which hinders an accurate reconstruction of bar dynamics. During this time interval, maximum elongation as well as maximum shortening range around 200 - 250 m (approximately 2.5 - 3 times the river width). Upstream of bend 4, bar wavelengths tend to remain fairly constant in time, with total variations shorter than one river width. The larger variations are observed in the reach between bend 4 and bend 7, with bars experiencing an elongation of more than 200 m just downstream of bend 4, followed by an almost linear transition to a shortening of more than 200 m before bend 7. Close to bend 8, bars suddenly shifted to elongation (up to 150 m). Downstream of this, in the long straight sub-reach between bend 10 and 11, bars showed little variations, with a tendency to shorten towards the end of the reach. Also the longitudinal mean trend of bar elongation shows abrupt shifts in correspondence of some bends, as it has been observed in Figure 3.5 for bar wavelength.

3.3.2 Bar migration

The second parameter considered in the characterization of bar dynamics is their migration. In Figure 3.8 the spatial trend of the cumulative bar migration over the period 1999-2010 is presented. In this case, migration was computed as the longitudinal shift of each bar unit, averaged considering both the front and the tail of the exposed deposit. Maximum downstream migration is approximately 1000 m (about 9 - 10 river widths or one average bar wavelength in the case of the downstream part of the reach). Many bars showed very low values of migration, with only 3 bars over a total of 77 denoting a slight upstream migration (negative values). In analogy with bar wavelength (Section 3.3.1), two rather different bar migration patterns characterize the same upstream and downstream sectors of the study reach. Upstream of bend 4 bars are generally non-migrating (or "steady"), with total migration values lower than one river width in both straight and curved reaches. In a few km downstream of bend 4, migration reaches its maximum, with values around 1000 m. Along this second sector, bars tend to migrate downstream consistently, with several

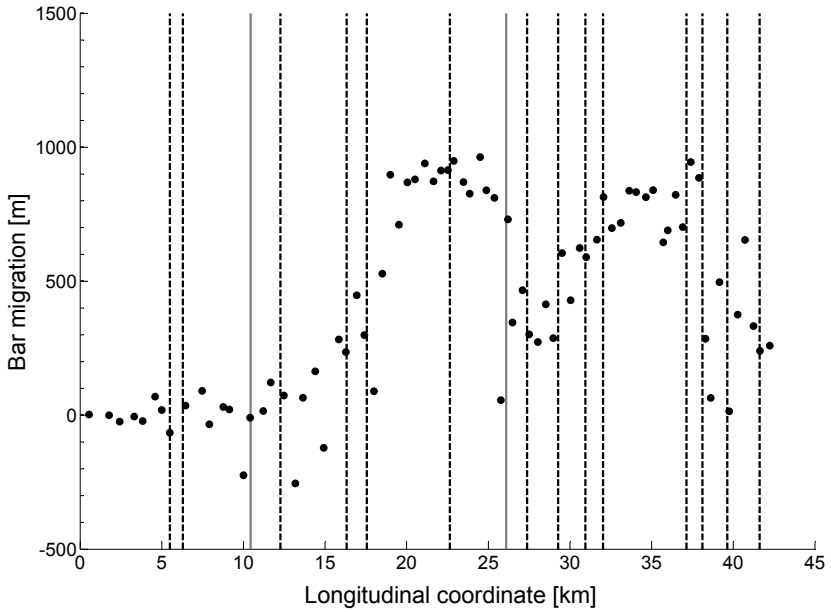

Figure 3.8: Cumulative bar migration in the period 1999-2010. Each point represents the total migration of single bars. Vertical lines represent bends (dashed) and ramps (continuous).

bar units moving downstream by 700 - 1000 m in most of the long straight subreaches 7, 8 and 13 (see Figure 3.6). The slowing effect of bends and ramps on alternate bars in the downstream sector is clearly visible. Close to bends 7, 8, 9 and 12, 13, 14, bars migrated less than half of the distance migrated by bars in the long straight sub-reaches. A few steady bars can be observed at the inner bank of bends 5, 12, and 13, and also close to the second ramp.

Bar migration is analyzed also at the time scale of the single flood event, by computing bar movement between each consecutive Landsat image. Two different sets of bars are presented in Figure 3.9, as representative of the different behavior of steady and migrating bars. A first set of bars (bar 36 and bar 30, located at km 5 and 12, respectively) was chosen to represent non-migrating bars (closed symbols in Figure 3.9). The second set of bars (bar 23 and bar 09, located at km 22 and 35, respectively) includes bars that are located sufficiently far from bends and ramps, so

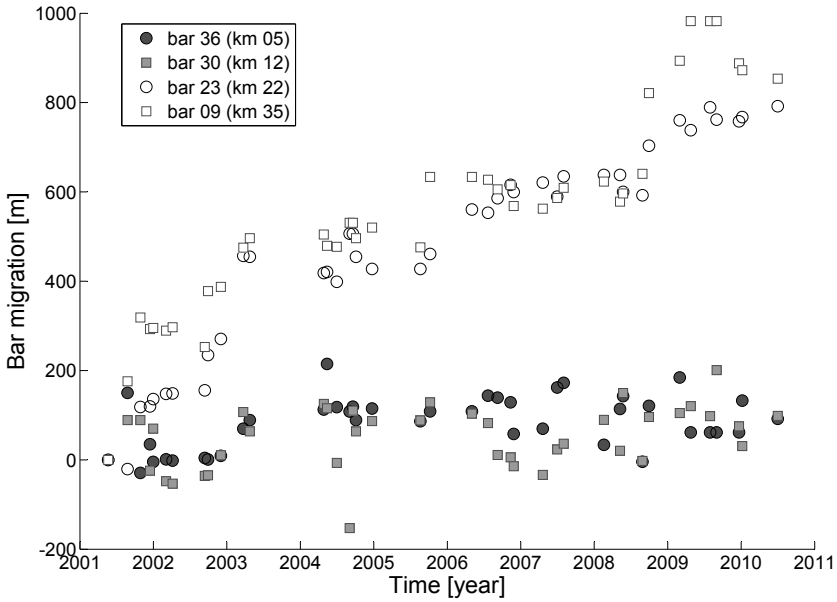

Figure 3.9: Four examples of bar migration as a function of time in the period 1999-2010. Open symbols refer to migrating bars, closed symbols refer to steady bars.

that they freely migrate downstream (open symbols). The step-by-step migration of these 4 bars shows that they move mainly during larger floods (see Figure 3.2 for a comparison). Periods without significant events (e.g., in 2006-2007) are characterized by barely no migration, also in the case of the migrating bars. Figure 3.9 shows also that steady bars (closed symbols) slightly moved upstream and downstream in a narrow range of about 2 river widths, and are not influenced by flood occurrence. These fluctuations around a fixed position may also be due to changes in the exposed area, as a consequence of the different discharges at which the Landsat images were acquired. This effect may also explain the few negative migration values plotted in Figure 3.8. However, this effect is not affecting the general pattern shown in Figure 3.9. Overall, the analysis on bar migration suggests that a migration threshold of a few channel widths (i.e., 200 m) can be used to discriminate between migrating and steady bars by comparing it with the decadal (1999 - 2010) cumulative migration

of each bar unit.

The effect of different floods on bar migration has been further analyzed for the entire period 1984-2012 by focussing on the bars in subreaches 7 and 13, which migrated the longest distance. Several floods were singled out by consecutive Landsat images, covering a range from $780\,\mathrm{m^3s^{-1}}$ to $2650\,\mathrm{m^3s^{-1}}$. The value of $780\,\mathrm{m^3s^{-1}}$ corresponds to the discharge with a return interval equal to 2 years (Q_2). This value was chosen as a morphologically relevant threshold, because it corresponds to conditions of fully transporting cross sections, and because no significant migration of bars was observed for floods with a lower peak discharge. The effect of different floods is reported in Figure 3.10 as a function of three potentially controlling factors on bar migration: i) the peak discharge value (Figure 3.10a); ii) the duration of flood events in which the discharge was higher than Q_2 (Figure 3.10b); iii) the total flood volume above Q_2 (Figure 3.10c). Overall, none of these considered flow parameters provide clear explanatory trends for bar migration.

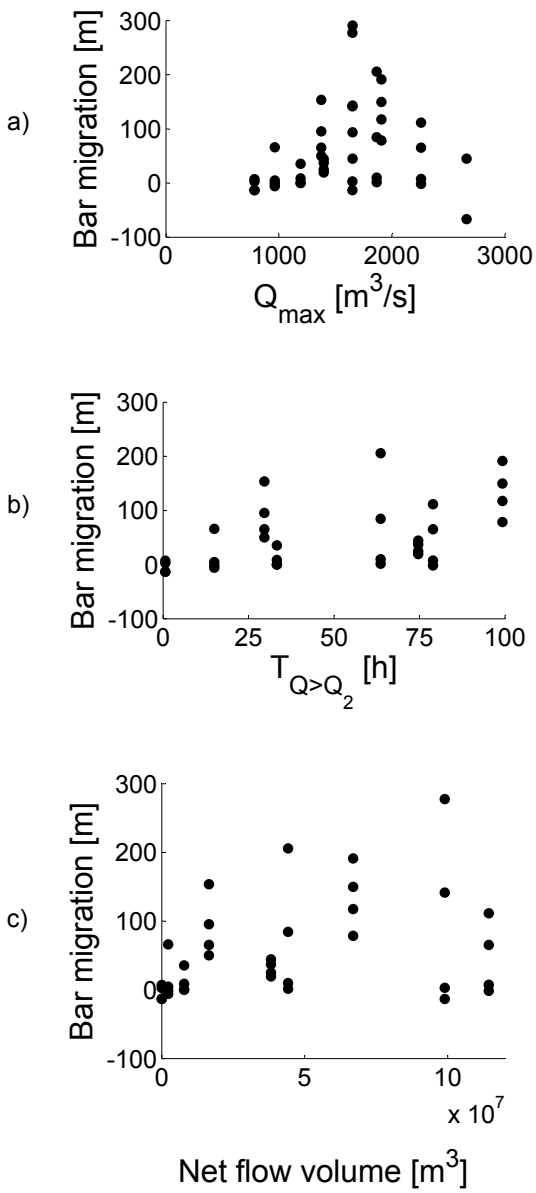

Figure 3.10: Bar migration during single floods as function of: i) peak flood discharge; ii) flood duration, considering a threshold equal to Q_2; iii) flood flow volume above the threshold discharge Q_2.

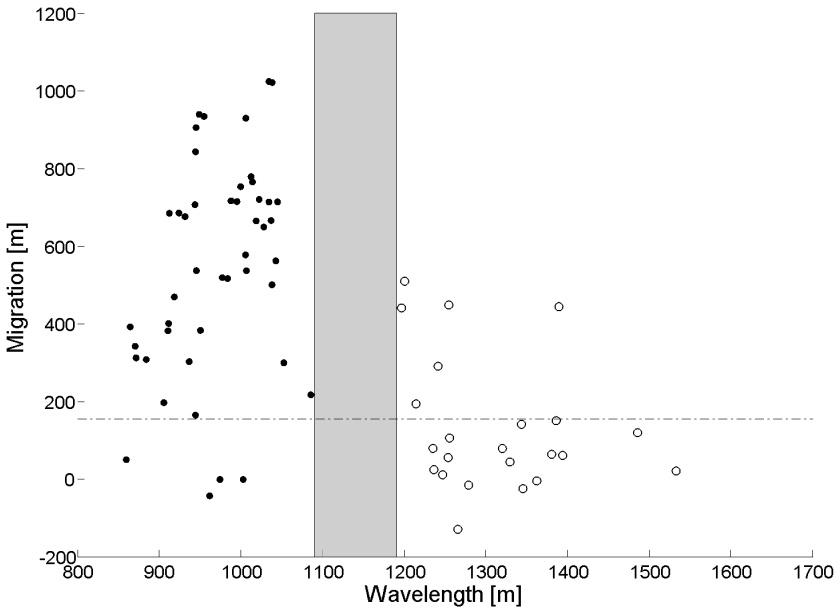

Figure 3.11: Cumulative bar migration in the period 1999-2010 as a function of bar wavelength.

There is a tendency of bar migration to increase for higher flood duration and flood volume, but the scatter of the data is high. Figure 3.10a shows an interesting pattern, although the points scatter. An ideal envelope of the point cloud attains a maximum migration value at a peak discharge up to roughly $1800\,\mathrm{m^3 s^{-1}}$, and then decreases again, reaching values close to 0 for the larger floods on record. This behavior can be related with the application of linear bar theories (section 3.4) and is further explored in the discussion.

The relationship between cumulative bar migration in the period 1999 - 2010 and bar wavelength is explicitly plotted in Figure 3.11. Differently from Figure 3.5, the wavelength value is obtained for each point in the plot as the average wavelength of the bar unit for which the comulative (1999 to 2010) migration has been computed. The migration threshold of 160 m used to discriminate between steady and migrating bars is represented through a horizontal dashed line. Several interesting information can be highlighted. Average bar wavelengths fall into two markedly different clus-

ters, resulting in a bar wavelength gap in the range 1090 m - 1190 m, where no bars plot. This allows to distinguish between "long" (i.e., > 1190 m) and "short" (i.e., < 1090 m) alternate bars. As already pointed out in Section 3.3.1, long bars can be found only in the upstream sector (open symbols), while short bars are found only in the downstream sector (closed symbols). A rather close relation between bar wavelength and cumulative migration appears: short bars are mostly migrating, whereas long bars are mainly steady. More precisely, 75% of long bars are steady and 90% of short bars migrate. Maximum migration of the shorter bars occurs within a wavelength range of $900 \div 1000$ m, though smaller migration values are possible in the same range. Only a few short bars show a different behavior, with much lower values of migration (10% of the short bars). These are generally bars close to bends or ramps, and their wavelength is strongly affected by these obstacles.

3.3.3 Bar amplitude

Values of bar height are reported in Figure 3.12, as a function of the longitudinal coordinate. They range between 2.5 m and 4 m and do not show any particular spatial trend. These values of bar height correspond to approximately $1 \div 1.5$ times the reach averaged water depth calculated with Q_2=780 $\mathrm{m^3 s^{-1}}$. In contrast to bar wavelength and migration, bar height is not significantly different for the upstream longer and steady bars compared to the downstream shorter and migrating bars. Bar height presents longitudinal fluctuations, often characterized by a minimum value in correspondence to bends and ramps. In particular, the second ramp has a strong effect, reducing bar height to 2 m.

3.4 Discussion

We discuss the results obtained in this study with reference to the main research goals stated in the Introduction. First we focus on the relevance of the developed dataset in comparison with existing ones, second we compare the observed alternate bar morphodynamics with previous field observations and finally we analyze to which extent analytical bar theories

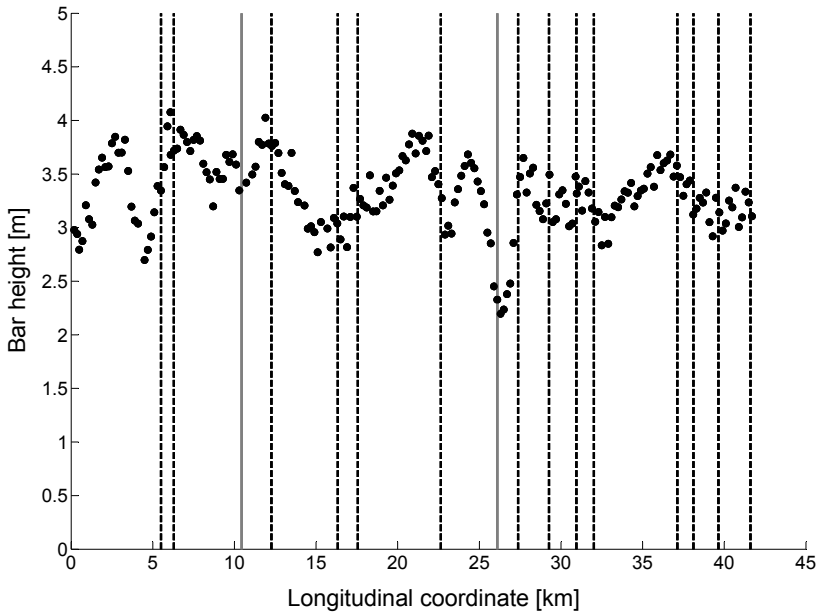

Figure 3.12: Bar height for each surveyed cross section as a function of the longitudinal coordinate. Vertical lines represent bends (dashed) and ramps (continuous).

prove to be useful in predicting and interpreting field observations.

3.4.1 The Alpine Rhine alternate bar dataset

The availability of a remotely sensed dataset of a 41.7 km long reach of the Alpine Rhine covering about 30 years allowed for a thorough investigation of the morphology and dynamics of 40 bar units. This is a valuable source of information to understand the controls on alternate bar formation and migration, which may greatly increase the possibility to evaluate and predict the evolution of these bed forms. Landsat imagery proved to be an excellent source of freely available data, in terms of number of images per year and pixel resolution, confirming the findings reported by *Henshaw et al.* [2013]. The possibility to choose among several images allowed for combining a multi-decadal analysis, with details on the effect of single floods. Such an approach can be replicated to study the dynamics

of bars (not only alternate bars) on river reaches of the same or of larger size worldwide.

The relevance of the developed dataset emerges in comparison to previous field studies, which generally considered a much smaller number of bars and a much shorter time period. The present study is the only multi-decadal study on alternate-bar dynamics in a river reach that includes about 40 bar wavelengths and based on an average of nearly 2 available surveys (i.e., Landsat images) per year. It has been possible to include such a high number of bars in the study thanks to the alternate bars reach being nearly 450 channel widths long. The reported results on the Alpine Rhine show that bar morphology and dynamics are variable in time and space. The effect of spatial discontinuities like bends, or temporal events like floods (or their absence) can have an impact on bar wavelength and migration on relatively long reaches. This has to be taken into account in order to improve our general understanding of these bedforms. Spatially and temporally long observations are even more relevant when the aim is to quantify bar migration. Very few field data on bar migration are available in the literature and this data set provides a valuable source of information for testing physical, numerical, and mathematical models.

Table 3.1 lists the main field observations reported in the literature in the last decades. Most of previous field studies are limited to short artificial channels (e.g., *Lewin* [1976]; *Welford* [1994]; *Ferguson et al.* [2011]; *Eekhout et al.* [2013]) or analyzed a relatively short time-scale (e.g., *Rodrigues et al.* [2012]; *Zolezzi et al.* [2012]; *Rodrigues et al.* [2015]). The only comparable cases in terms of space and time scale are the studies presented by *Church and Rice* [2009], *Ferguson et al.* [2011] and by *Jaballah et al.* [2015]. Though all these studies refer to alternate bars, their setting may slightly differ, suggesting that some care is required when comparing observations. For example, in the Fraser River [*Church and Rice*, 2009] channel width shows more pronounced spatial oscillations, which likely provide an additional forcing effect, enhancing the formation of steady bars [*Repetto et al.*, 2002]. This occurs also in the Arc River [*Jaballah et al.*, 2015], though to a much smaller extent and only before the engineering works that flattened the channel bed towards the middle of the observation period. In other cases, as in *Rodrigues et al.* [2012]

and *Rodrigues et al.* [2015], the relatively short reach length may produce significant local effects, imposed by the upstream and downstream morphological conditions. Moreover, in both the Fraser and Arc rivers vegetation is reported as a relevant factor that tends to affect bar dynamics by stabilizing them, stopping their migration, as well as by changing their wavelength and amplitude (*Bertoldi et al.* [2014]).

3.4.2 Observed bar morphodynamics: wavelength and migration

In terms of observed bar wavelength (as a function of channel width), the freely migrating bars of the downstream part of the Alpine Rhine show comparable results to those reported in previous field studies, ranging between the shorter bars monitored by *Church and Rice* [2009] (4 to 5 times the width) and the longer (9 to 10 widths) reported by *Ferguson et al.* [2011]. This range is comparable also to laboratory findings (*Ikeda* [1984], *Jäggi* [1984], *Tubino et al.* [1999]).

Few other studies report on data about bar migration. The Alpine Rhine shows an average migration of the free bars located in the downstream reach that is of the order of $0.8 \div 0.9$ times the average channel width per year. Previous studies on the same river reach, though based on a different methodology, indicate migration rates occurred in the 1960s and 1970s ranging between 1.5 and 3 times the average channel width per year (*Zeller* [1967] cited in *Jäggi* [1983], *Jäggi* [1983]). A close comparison between our estimate and previous estimates on the same river reach is barely possible because previous estimates were based on different observation time periods, and thus the discrepancy might be due to the effect of a few relevant flood events and not reflect a decade-averaged behavior.

An analogous result, with a value of 0.7 times the channel width per year, can be inferred from data presented by *Rodrigues et al.* [2012] on the Loire river, which has sandy bed material. Bar migration is a complex function of discharge (or sediment transport rate) and bar morphology, and is also strongly affected by grain sorting (*Lanzoni* [2000b]) and presence of obstacles. Therefore, it is difficult to compare bar migration among different rivers, and between field observations and flume experi-

ments, where the discharge is generally constant and the channel is perfectly regular and straight. *Crosato et al.* [2012] reported on long-term experiments on alternate bar dynamics, showing that there is a strong decreasing relationship between bar migration speed and bar wavelength, with bar migration reducing to half when the wavelength increases from 5 to 7.5 times the channel width. Our observations on the Alpine Rhine show a similar relation, although with a few differences. Figure 3.11 shows an increase of bar migration up to a wavelength of about 9-10 times the river width, whereas the much longer bars are steady, or migrate very slowly.

Crosato et al. [2012] also reported on the formation of steady longer bars (particularly in the upstream part of the flume), which are likely to suppress the migrating bars. It is not clear whether the systematic occurrence of steady bars in the upper reach of the Alpine Rhine may be explained in these terms, or whether they are caused by the occurrence of sharp bends which may induce the formation of forced bed forms (see *Zolezzi and Seminara* [2001]; *Zolezzi et al.* [2005]. The recent extensive study of *Jaballah et al.* [2015] on alternate bars dynamics in the Arc River, France, showed the existence of migrating bars, along with steady, longer bars affected by spatial constraints as a bend and a bridge. Similarly, *Ferguson et al.* [2011] reported the coexistence of steady and migrating bars in the Vedder Canal, though this was not the main focus of their analysis. *Jaballah et al.* [2015] pointed out the relevance of including flow unsteadiness, to better understand and predict river bar evolution. In particular, flow conditions falling under the full-transport discharge may be responsible for the creation of shorter mid-channel bars that contribute to a more complex pattern.

3.5 Conclusions

This chapter reports on the morphological dynamics of alternate bars in the Alpine Rhine, taking advantage of freely available Landsat imagery. The analysis resulted in the longest spatial and temporal field case study of river bars in channelized rivers with a temporal survey resolution allowing to investigate the effect of individual flood events, and provided

new quantitative data on bar wavelength and migration. Bars show a spatially selective behavior, with short, migrating bars occurring in distinct straight reaches with respect to longer, steady bars. A full range of bar wavelengths and more complex patterns occur in reaches with bends and ramps. Bar height obtained from cross section monitoring was found to be much more uniform. The temporally long dataset, including approximately 30 floods with different magnitude and duration, allowed the investigation of bar migration as a function of discharge, showing that bars migrate faster for intermediate floods, as larger discharges are probably responsible for a slight flattening of the bed forms.

3.6 Acknowledgements

Landsat data were available from the U.S. Geological Survey. The authors wish to thank Lukas Indermaur for providing the hydrological data from three gauging stations along the Rhine and David Vetsch for providing the cross sections of the Alpine Rhine.

Chapter 4

Application of analytical morphodynamic theories to observations on alternate bars in the Alpine Rhine

Analytical theories of free and forced bars in straight channels (e.g. the ones presented in Chapter 2) can provide useful information on alternate-bar geometry and dynamics and can also help interpret the physical processes at the basis of their occurrence. Studies that compare the outcomes of analytical alternate bar theories in straight channels with field cases are relatively few and recent (e.g. *Welford*, 1994; *Eekhout et al.*, 2013; *Rodrigues et al.*, 2015; *Jaballah et al.*, 2015). The present chapter proposes an application of linear and, to a lesser extent, weakly non-linear theories for migrating and steady bars in straight channels to the case study of the Alpine Rhine, for which alternate-bar dynamics have been extensively examined in Chapter 3 by means of a multi-temporal analysis of satellite images. The present chapter especially focuses on the comparison between theoretical predictions of wavelength and migration properties of alternate bars.

The main findings of the chapter can be summarized in two broad points: (i) an approach to apply analytical theories of alternate bars to a field case is proposed, which accounts for the differences in setting between

theories and real rivers; (ii) outcomes of analytical theories help developing interpretations and explanations for observed behavior in the field. Specifically, the application of the steady bar theory allows to interpret the observed difference in alternate-bar properties between the upstream and downstream sectors of the study reach. Remarkably, the interpretation appearing as the most consistent among the three developed ones suggests that such strong difference in behavior might be attributed to the phenomenon of 2D upstream and downstream morphodynamic influence occurring under sub- and super-resonant conditions. This is relevant because 2D morphodynamic influence was only validated through laboratory observations, without any field observation so far indicating how such phenomenon could manifest itself in real, albeit regulated, rivers.

The chapter is structured as follows.

In Section 4.1 the main differences in setting between analytical bar theories and the typical field case of a channelized river are reviewed, and an approach to apply analytical theories to a field case that copes with such differences is proposed.

In Section 4.2 the field case of the Alpine Rhine is summarized, by focusing on the key information related to the subsequent application of the analytical theories. A summary of the observed, consistent spatial variability of several bar properties is highlighted, which raises an important question related to its possible explanations.

Section 4.3 presents the application of several bar theories (see review in Chapter 2) to the field case, starting from the computation of the input parameters, the theoretical thresholds and then moving to the predicted bar properties; the insights emerging from such an application are immediately discussed. The analysis does not provide a straightforward interpretation of the observed spatially selective behavior whereby longer, steady bars essentially concentrate in the upstream sector while shorter, migrating bars can be found only in the straight reaches of the central and downstream sectors.

This particularly intriguing issue is dealt with in Section 4.4, where possible interpretations are developed and discussed in the light of the outcomes of the bar theories. The approach proposed in Section 4.2 provides support to such behavior being associated with a higher persistence

of super-resonant conditions in the upstream sector compared to the other ones, and to the corresponding bar dynamics being coherent with that of a super-resonant straight channel.

4.1 An approach for the application of analytical bar theories to field cases

Analytical bar theories can be viewed as simplified deterministic models, because they rely on a series of simplifying assumptions that aim to keep the mathematical problem at the lowest meaningful level of complexity, thus enabling to obtain mathematical solutions in closed analytical form. Their main advantages are the requirement of almost negligible computational time, the possibility to easily detect the key controlling parameters for the physical processes, and the ability to predict the related relevant spatial and temporal scales.

It is useful here to briefly recall the main features and outcomes of analytical bar theories that will be compared with the field observations on the Alpine Rhine River. The planform of the study reach can be viewed as a sequence of 16 straight longitudinal sections, connected by 14 short bends of constant curvature, and two ramps (see left panel of Figure 3.1). The most relevant bar theories for this case are therefore those for straight river reaches, which account for 83% of the whole reach length. As many other analytical models for river bars and meandering, most of these theories predict properties of alternate bars for given constant values of flow discharge, channel width, reach slope, and sediment grain size. Moreover, the model assumes flow conditions where the entire cross section is actively transporting sediments. This means that the channel width corresponds to the active width (*Ashmore et al.* [2011]; *Zolezzi et al.* [2012]).

Linear theories consider bars as small-amplitude perturbations of the bed topography, i.e., much smaller compared to the reach-averaged flow depth. They allow to predict the conditions of formation, wavelength, and migration of bars. Non-linear theories (*Colombini et al.* [1987]; *Schielen et al.* [1993]) are needed to predict the amplitude of bars although they also assume small amplitudes a priori. In straight channels, linear theories

predict free alternate bars to be downstream migrating and forced alternate bars to be non-migrating. In the same setting, forced steady bars are predicted to be about twice as long ($L/W \sim 15 \div 20$) compared to free migrating bars ($L/W \sim 6 \div 10$). Comparable length scales are predicted by non-linear theories, while migration speed is largely overestimated by linear theories [*Colombini et al.*, 1987].

This section describes in detail the hypotheses on which the free and forced steady bars in straight channels are based (4.1.1) and how these hypotheses differ from the real setting of a field case (4.1.2). The computation of theoretical parameters, like those defining *critical* and *resonant* alternate bar conditions, in the setting of a typical field case for a regulated river are dealt with in 4.1.3.

4.1.1 Theoretical setting

Aim of the analytical bar theories is to describe the formation and initial development of alternate bars in straight channels with erodible beds. The underlying approach seeks to find exact solutions of simplified mathematical problems in which only the main physical processes are retained in the solved equations. Even a straightened regulated river reach presents a higher level of complexity compared to the one accounted for in analytical models. Such difference needs to be carefully accounted for when aiming at using theoretical morphodynamic models for real cases. The present section therefore starts by reviewing the most important hypotheses on which the analytical bar models are based.

Depth-averaged mathematical models. The mathematical system solved in most bar theories [*Olesen*, 1983; *Struiksma et al.*, 1985; *Colombini et al.*, 1987; *Tubino*, 1991; *Schielen et al.*, 1993; *Tubino et al.*, 1999; *Zolezzi and Seminara*, 2001; *Crosato and Mosselman*, 2009] is based on equations averaged over the water depth, based on the assumption that the ratio between the width and the depth is large enough to treat the flow as two-dimensional. The linear free bar theory based on the three-dimensional model presented by *Tubino et al.*, 1999 shows that the 2D solution does not differ substantially from the 3D solution in terms of the linear stability of free bars, under bed-load-dominated conditions. Secondary flows play in this process a minor role.

Infinitely long channel. Theories for free and forced bars are written for a sufficiently long straight channel (strictly speaking, infinitely long). The role of streamwise boundary conditions in the solution is considered only in the theory of steady bars, which amplitude can vary in space. The steady bar theory often assumes a channel that is bounded on one end, and that is infinitely long on the opposite end, i.e. it can be named as "semi-infinite". On the contrary, streamwise boundary conditions are periodical in the free bar theories, which is equivalent to assume an infinite straight channel domain.

Quasi-steady flow field. Most theories for alternate bars assume a constant discharge Q and also assume that the flow field can be considered in equilibrium with a bed that slowly adapts in time. The role of flow unsteadiness in influencing the alternate bar development is addressed in *Tubino* [1991].

Uniform slope. A condition of constant longitudinal slope as well as of initially horizontal transverse slope is considered.

Uniform width. As for longitudinal bed slope, the width of the channel is set as constant in time and in space. The case of sinusoidally varying width in space in straight channels is analysed by *Repetto et al.* [2002], while *Zen et al.* [2014] investigate the role of width variability in time.

Rectangular cross section. The reference flow that is used as basic state is the uniform flow occurring in the straight channel with a rectangular cross section; as a consequence, when bar perturbations are infinitesimal, for every value of the discharge $Q > 0$, the cross section can be considered as fully wet.

Uniform grain size. The bed is modelled with uniform grain size. Sediment porosity is also constant.

Dominant bed-load transport. Sediment transport is considered to occur mainly as bed load by most analytical bar theories. The role of suspended transport, relevant for large values of the parameter θ, and in sand-bed rivers has been investigated by *Talmon* [1992], *Tubino et al.* [1999] and by *Federici and Seminara* [2006].

Fully transporting cross-section. Analytical bar theories assume a fully transporting cross-section, i.e., that sediment transport occurs across the whole considered channel width. Since the reference cross section is rect-

angular and wall effects are neglected, using a bed-load transport formula with a lower threshold for incipient motion (e.g. *Meyer-Peter and Müller* [1948], *Hunziker and Jäggi* [2002], *Wong and Parker* [2006], *Huang* [2010]) implies that the following two cases can occur:

- **partial or no transport**: for low values of the discharge Q, the Shields parameter θ remains below the critical threshold θ_C for sediment motion in at least part of the cross section, with no solid transport theoretically occurring in that part of the cross section;
- **full transport**: for higher values of Q, the condition $\theta > \theta_C$ is satisfied in the whole cross section, which is fully transporting sediments, thus fitting with the assumption of the theories.

It is important to note that for sediment transport to occur across the whole cross section, the condition $\theta > \theta_c$ might be too restrictive, because sediment may be locally transported for short distances even when such condition is not strictly satisfied.

Linear and weakly non-linear approach. Bar theories, like most morphodynamic theories that investigate regular patterns, assume patterns to be of "small" amplitude (ϵ) with respect to the magnitude of a basic state that is typically a uniform flow occurring in the same straight channel. Mathematically, this allows to seek approximate, asymptotic solutions of the governing equations Linear solutions retain only terms up to order $O(\epsilon)$ (e.g. 2D *Blondeaux and Seminara* [1985]; *Zolezzi and Seminara* [2001], 3D *Colombini and Stocchino* [2012]), while weakly non-linear solutions (e.g. *Colombini et al.* [1987]; *Tubino* [1991]; *Seminara and Tubino* [1992]; *Schielen et al.* [1993]) solve the basic state and higher order of approximation, $O\left(\epsilon^{1/2}\right)$, $O(\epsilon)$, $O\left(\epsilon^{3/2}\right)$. *Colombini et al.* [1987] present the weakly non-linear solution in the neighbourhood of the critical conditions ($\Omega = 0$, $\beta = \beta_C$, $\lambda = \lambda_C$), *Seminara and Tubino* [1992] developed the weakly nonlinear theory for steady bars in straight channels (also named "spatial bars" therein), through a weakly non-linear perturbation expansion in the neighbourhood of the resonant conditions ($\beta = \beta_R$, $\lambda = \lambda_R$).

Effect of dunes and ripples. Effect of smaller-scale bed-forms like dunes and ripples is included in bar theories in a parametrized way through empirical formulae that account for their additional roughness. Dunes can

coexist with alternate bars most commonly in sandy rivers. *Colombini and Stocchino* [2012] using the 3D Reynolds-Averaged Navier Stokes equations to study the stability of bars, dunes and ripples within the same unifying theoretical framework, investigate the linear stability of a uniform flow in an infinitely wide erodible channel with longitudinal and transversal periodical disturbances at multiple spatial scales.

Role of riparian vegetation. Analytical theories mainly do not include formation and development of vegetation, limiting the analysis to the interaction between flow field and bed dynamics. A recent novel contribution has been proposed by *Bärenbold et al.* [2016].

4.1.2 Corresponding setting in a field case

Here the hypotheses described in 4.1.1 are point by point discussed in relation to a typical setting of a channelized, regulated river, with specific reference to the field case of the Alpine Rhine river, widely described in Chapter 3.

Depth-averaged mathematical model. The planform configuration of the Alpine Rhine river, in the reach between Landquart and Ill confluences, is characterized by a trapezoidal cross section in which the width is always much greater than the water depth, so the hypothesis of width large enough for the flow to be modelled as two-dimensional is still valid. Nevertheless, (i) along the reach, planform discontinuities like bends, ramps and bridge piers influence locally the leading 2D regime, with three-dimensional effects and (ii) presence of alternate bars in the whole reach also influences the flow field generating vertical velocity components. For the analysis at the bar scale, however, these issues do not pose relevant limitations.

Infinitely long channel. The Alpine Rhine domain is composed by a series of straight channels with finite lengths and bends with different lengths and radius of curvature. The length of straight channels is variable from a few times the river width to $40 \div 50$ times the width, in which $4 \div 5$ free bar wavelengths or $2 \div 3$ forced bar wavelength can be contained. This assumption will always set a difference between theory and real cases, that must be reflected in the interpretation of the results.

Quasi-steady flow field. The discharge of every regulated and un-

regulated river reach, like the Alpine Rhine reach, is not constant in time. For alpine rivers, the natural hydrograph follows two main regimes: snow-melting in late spring and summer and floods especially in spring and autumn. Hydro-power production is also present upstream the chosen reach, influencing with hydropeaking the low-flow hydrograph of the Alpine Rhine.

Uniform slope. Longitudinal slope varies locally in the whole reach (Fig. 4.2). In particular the reach of the Alpine Rhine presents three different average values of longitudinal slope, decreasing from upstream to downstream. The control points of the different sectors are represented by one bend (b_4) and one unstructured ramp (r_2) along the reach.

Uniform width. Even if the river has been straightened and the width regularized, the value of the channel width is still slowly dependent on the streamwise coordinate, ranging between 86 m and 106 m (Fig. 4.1).

Rectangular cross sections. The designed cross section of the Alpine Rhine is trapezoidal, with fixed levees composed of boulders that prevent planform changes, so the hypothesis of a rectangular cross section is nearly respected. The actual cross section dataset shows riverbeds modified by the presence of scours and deposits of alternate bars. This means also that, with respect to flat rectangular sections, there is a threshold discharge for which the cross section can be considered fully wet. Values of fully wet discharges, reported also in Table 3.2, are in the range $230 \div 380\,\mathrm{m^3 s^{-1}}$. Also, channel width almost does not change with flow discharge.

Uniform grain size. The riverbed is composed of heterogeneous sediment diameters, with local variability between thalweg and bar tops and fining effect in the longitudinal direction. Average values range between 0.06 m in the upstream sector and 0.02 m in the downstream sector [*Hunziker et al.*, 2001].

Dominant bed-load transport. The field case of the Alpine Rhine river is a case of a gravel bed river in which the value of the parameter θ, see Figure 4.9, rarely exceeds values of about 0.20 for values of discharges with a return interval of 100 years. This range of values is consistent with the case of sediment transport due mainly to bed-load.

Fully transporting cross-section. As the alignment of rivers is rarely straight, their beds are rarely flat. So a fully transporting section is

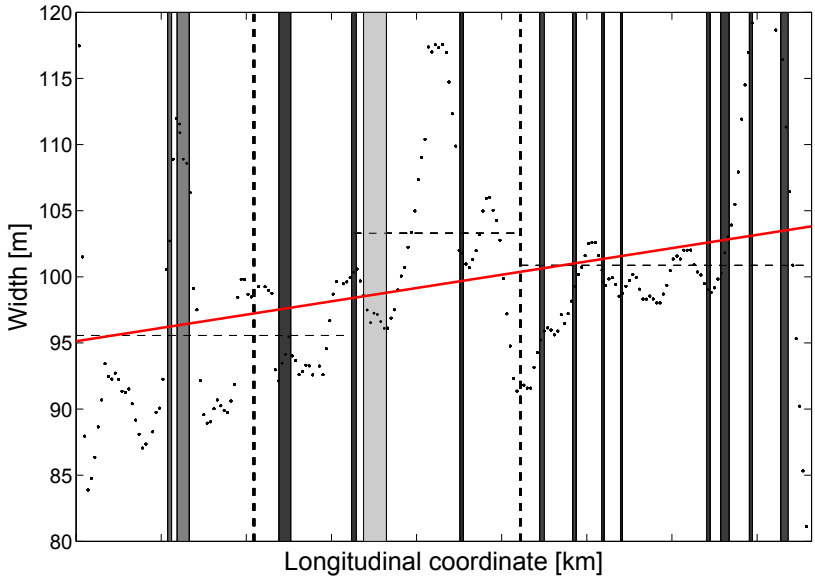

Figure 4.1: Width of the Alpine Rhine. Dots represent the original data, horizontal lines the sector averages, the red line the linear regression of the data. Bends and ramps are also shown as vertical stripes. In particular bends are reported in terms of their length (the width of the vertical band) and of their radius of curvature (darker band means smaller radius).

reached for a greater discharge (Q_{FT}) than the flat-bed section with the same width. In figure 4.3 the partially and fully wet sections (the latter corresponding to Q_{FW}) and the fully transporting depth (corresponding to Q_{FT}) are shown.

Linear and weakly non-linear approach. This represents an intrinsic limitation of the theories. Its role can be partially investigated by means of numerical models (see Chapter 5).

Effect of dunes and ripples. The effect of dunes and ripples is thought to have a very limited relevance in a gravel bed river.

Role of riparian vegetation. Most gravel bars in the Alpine Rhine reach have no vegetation. The causes of this are still under investigation and might be associated to the hydrological regime with snow-melting that causes an increase of the water depth from late spring to late summer

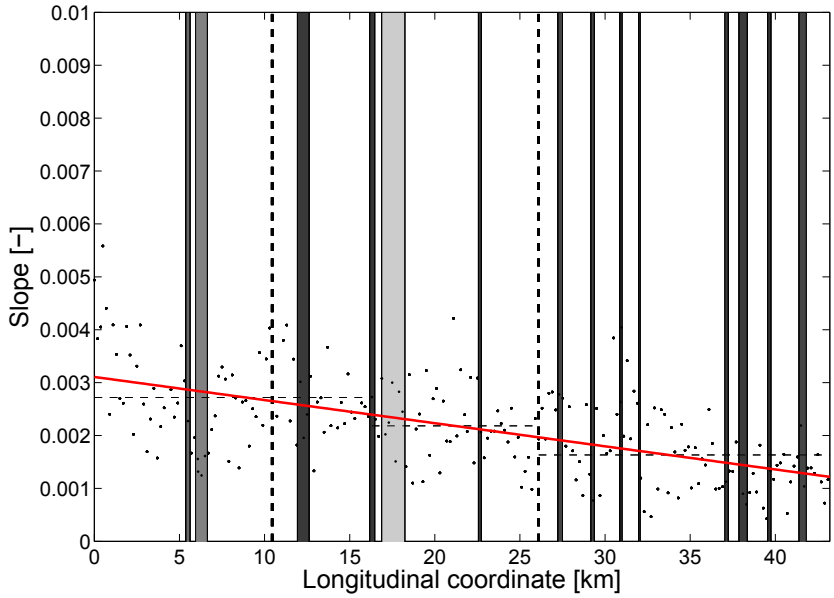

Figure 4.2: Slope of the Alpine Rhine. Dots represent the original data, horizontal lines the sector averages, the red line the linear regression of the data. Bends and ramps are also shown as vertical stripes. In particular bends are reported in terms of their length (the width of the vertical band) and of their radius of curvature (darker band means smaller radius).

that commonly covers the top of the deposits. Therefore, the role of the vegetation in the development of alternate bars [*Bertoldi et al.*, 2014] has not been considered as relevant for the field case.

4.1.3 The proposed approach

Here the approach developed in the present chapter is briefly summarized in a general fashion. Its application to the case study of the Alpine Rhine river is further described in Section 4.2, and the results of this exercise are described and commented in Section 4.3.

The first step is the analysis of the most relevant differences between the theoretical setting and the setting in the field case of interest, following the template presented in the previous section (4.1.2). In the case of the Alpine Rhine and, probably, in analogous channelized and regulated river

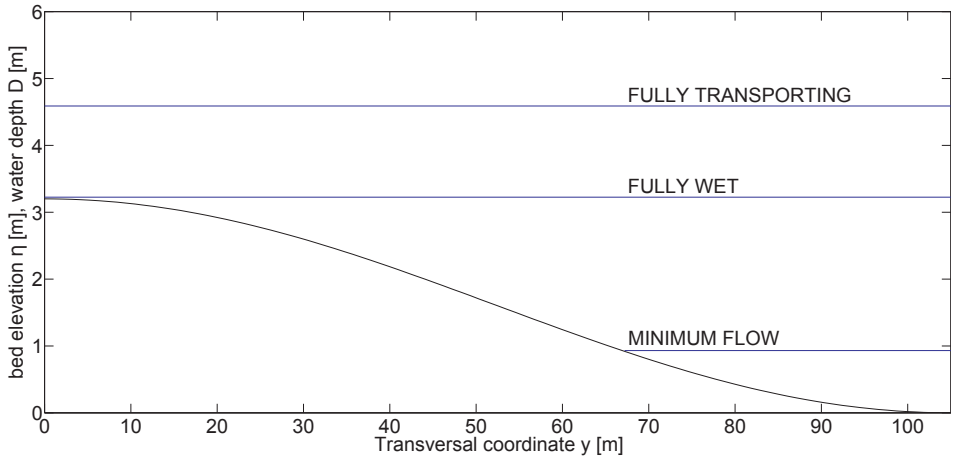

Figure 4.3: Scheme of the cross section with a cosine behaviour of the bed. Three water levels are indicated: minimum flow (Q=24 m^3/s), fully wet (corresponding to Q_{FW}) and fully transporting (corresponding to Q_{FT}).

reaches, the most relevant difference lies in the temporal variability of the discharge, whereas most theories assume a constant, "bar-forming", streamflow value. Other sources of differences are the spatial heterogeneity in grain size, longitudinal slope and channel width. These differences can be partially dealt with by partitioning the study reach of interest in sub-reaches (or sectors, as they are called in the present thesis) where such quantities can be considered sufficiently homogeneous. This does not guarantee a full compliance between the theoretical and field settings, but it should make them more closely comparable.

An important spatial heterogeneity is related to the grain size distribution of the river bed. Within the context of gravel-bed rivers, and more in general of bedload-dominated rivers, analytical bar theories cannot be considered to have been developed at an enough mature stage to comprehensively examine the effect of this type of variability, though the theory of *Lanzoni and Tubino* [1999] might provide useful indications in this respect.

In the case of channelized rivers, moreover, it must be noted that the channel width only displays a weak variability with river discharge and, therefore, with flow stage, which allows, in most cases, to assume that channel width is constant in a broad spectrum of representative discharge

values for a given reach. In rivers that are laterally unconstrained, conversely, the computation of channel width has to take into account its dependence from the flow discharge, when computing the input parameters for the theory.

The differences described above are mainly reflected in the computation of the input parameters for the analytical theories.

For the reasons described above, discharge variability will therefore be used as the main difference in setting between theories and the field case of interest. Coping with this implies to address a fundamentally unanswered question so far: is it possible to define or compute a discharge value that is fully equivalent to the actual hydrograph in terms of the observed bar properties of a river reach? The next steps of the presented approach represent a workable option in this direction.

Another key difference, which will always characterize a field setting with respect to analytical theories, is the length of the spatial domains of interest, which are always finite in reality. Such difference is mainly reflected in the interpretation that can be made of the results of the application of the theory of free and forced bars in straight channels.

The second step of the presented approach consists of computing the input parameters of the analytical theories. Those input parameters (Chapter 2) theoretically consist of reach-averaged values of several hydraulic characteristics of the reach, and should characterize a theoretical uniform reference flow occurring in the same reach with a flat bed. A locally uniform flow approach can therefore be taken, using available topographic, grain size and streamflow data for the homogeneous sub-reaches (sectors) that have been identified in the previous step.

When discharge variability is identified as the most important difference between the theoretical and the field setting, the relevant dimensionless input parameters of the analytical theories can be computed in principle for every value of the flow discharge, thus resulting in a series of "rating curves" whereby each of the parameters (β, θ, d_s) is plotted as function of the flow discharge.

The third step of the approach foresees to apply the theories of interest for every streamflow value within the relevant discharge range for the chosen reach. For every discharge value, and within each identified

homogeneous river sector, this yields a series of theoretical parameters like the critical and resonant aspect ratios (β_C and β_R), the corresponding wavenumbers (λ_C and λ_R) and many other ones.

In channelized river reaches, where channel width does not relevantly change with discharge, such exercise would typically yield a decreasing behavior of the aspect ratio β with discharge, and an increasing trend of both the Shields parameter θ and of the relative roughness d_s, because of the underlying uniform flow assumption. As a consequence of the typical variability of the critical and resonant values of the channel aspect ratio β, which increase with the Shields parameter θ and decrease with the relative roughness d_s, it is possible to define two key discharge values, named Q_C, Q_R in the following, for which the relations $\beta = \beta_C$ and $\beta = \beta_R$ hold, respectively. In addition to this, another key discharge value can be quantified: it is the value corresponding to the conditions of a fully sediment transporting cross-section, named Q_{FT} in the present work, which sets the lower discharge limit of the applicability of the analytical bar theories.

The last step of the approach is aimed at establishing in which region of the theoretical parameters space the river reach of interest is dominantly located, given the discharge variability that invariably characterizes it. The following is a possible way to cope with the unanswered fundamental question posed above, about the possible existence of an equivalent, representative discharge value with which it is possible to predict the observed bar properties of a given reach of a (channelized) river.

In Figure 4.4 the neutral curve in which the $\Omega = 0$ and $\omega = 0$ curves are plotted along with three regions in which bars are theoretically expected with different behavior. In Figure 4.5 the same regions are highlighted with the same colours as a function of the discharge during a schematic flood wave. The green stable region ($\Omega < 0$, free bars are damped in time) of Figure 4.4 corresponds to the peak of the discharge in Figure 4.5. The red and blue regions of Figure 4.4 correspond to the unstable region ($\Omega > 0$) in which free bars tend to increase their amplitude in time. The red regions represent the sub-resonant, bar-unstable conditions ($\beta < \beta_R$), while the blue regions correspond to the super-resonant, unstable conditions ($\beta > \beta_R$). In terms of the width ratio β the three regions are

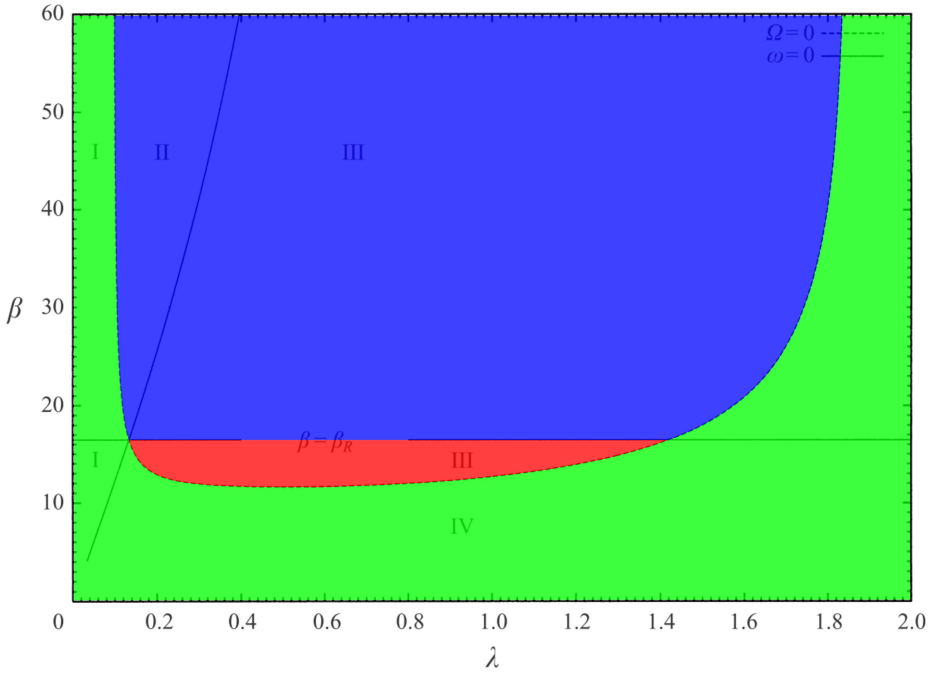

Figure 4.4: Neutral curves ($\Omega = \omega = 0$) of linear theory of free alternate bars in straight channels. The figure shows three different regions in which markedly distinct bar properties are predicted: sub-critical (green, flat bed, no free bars), super-critical and sub-resonant (red), super-critical and super-resonant (blue).

defined as:

1 - blue super-resonant and super-critical region: $\beta > \beta_R > \beta_C$. Free bed perturbations tend to grow in time and 2D morphodynamic influence, which displays itself in the form of forced steady bars, can also occur upstream of localised planform discontinuities;

2 - red sub-resonant and super-critical regime: $\beta_R > \beta > \beta_C$. Free bed perturbations tend to grow in time and 2D morphodynamic influence occurs only downstream of local persistent discontinuities and vanishes in space after a few steady bar wavelengths.

3 - green sub-resonant and sub-critical configuration: $\beta_R > \beta_C > \beta$. Free bed perturbations are damped in time, so free bars tend to be flattened under this flow regime.

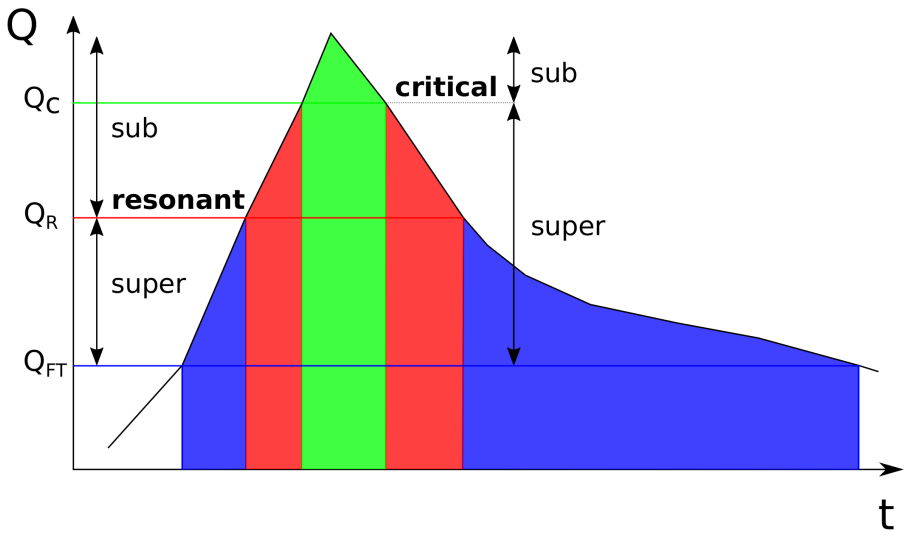

Figure 4.5: Schematic flood wave in which the three regions of Figure 4.4 are evidenced along a time axis. The super-resonant regime (in blue) opens and closes the idealised wave, the sub-critical regime (in green) is present in correspondence of the flood peak, while the sub-resonant regime (in red) connects the other two.

The values of discharge corresponding to the critical (Q_C) and resonant (Q_R) condition are shown in Figure 4.5 together with Q_{FT}. β decreases when increasing Q, so that the super-resonant condition is ideally always the starting and ending condition of a flood event, while the sub-resonant case is the intermediate condition. This occurs if the condition $Q_R > Q_{FT}$ is met. Otherwise, the super-resonant condition would not occur during the flood-wave. In case of flood peaks in which the conditions are never above Q_C, floods have an exclusive destabilizing role in terms of free alternate bar dynamics, while the greater the sub-critical green region is, the greater should be the corresponding volume of sediment flushed from bars towards a flat bed condition.

The concept illustrated in Figure 4.5 represents a possible way to tackle the unsolved "equivalence" question about the dominant positioning of a river reach (characterized by variable discharge) in the theoretical parameters space (characterized mostly by constant discharge). The time length

of the three regions can indeed be used as an indicator of "how long" the study reach keeps within each of the three theoretical regimes, under which theoretically different free and forced bars behavior can be expected in straight channels.

4.2 The field case: Alpine Rhine river

Here the case of the Alpine Rhine river is presented with features of two separate but adjacent individual reaches, the former with alternate bars, the latter without.

4.2.1 Alpine Rhine river

The Alpine Rhine river has been completely straightened in the past two centuries. Nowadays two main reaches can be described: the upstream one is located between the confluence of the Landquart river and of the Ill river and present a continuous sequence of alternate bars, as already shown in Chapter3. The downstream reach is located between the confluence of the Ill river and the lake of Constance. In this downstream reach, herein called 'Downstream Ill', channel width is smaller (average of 60 m), slope is comparable with the downstream sector of the upstream reach (s=0.001), as well as mean sediment size d^*_{50}. The hydrograph of Downstream Ill sums the contributions of the upstream reach and of the Ill basin. The contribution of the Ill basin represents 28% of the total volume of water entering into the Lake of Constance.

4.2.2 Data and methods

A complete dataset of cross sections of the Alpine Rhine between the Landquart river and the lake of Constance surveyed in 2005 is used to determine hydraulic variables of the reach. The survey covers almost 70 km, from km 23.3 (Landquart confluence, km 0 of the x-axis of Figure 4.6 and Figure 4.7) to km 93 (lake of Constance) in which cross sections are taken on average with a longitudinal spacing of 200 m, for an approximate total of 350 cross sections. Uniform flow conditions are computed in each cross section, in a range of discharges between 50 m^3s^{-1}, and 3000 m^3s^{-1}.

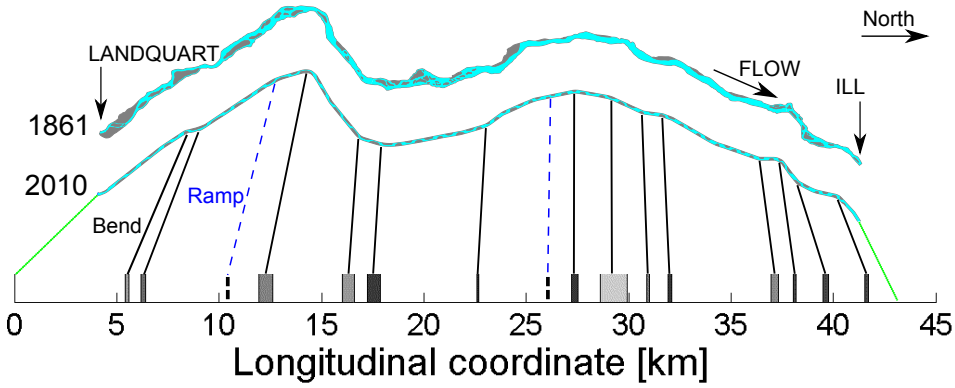

Figure 4.6: Alpine Rhine River, reach between Landquart River and Ill River. The upper part shows the reach in 1961, before the rectification, and the present situation. The lower part of the picture is the longitudinal centerline of the river in which the bends and ramps are described. In particular, bends are reported in terms of their length (the length of the vertical band) and of their radius of curvature (darker is smaller).

An Engelund method is used to evaluate uniform flow conditions for each cross section, considering a sediment diameter d_{50} linearly decreasing from 0.06 m at the Landquart confluence to 0.02 m at and after the Ill confluence. Width is calculated using data of the cross sections and averaging with the Landsat images. Slope is considered constant per sector. The reach shown in Figure 4.6 is divided in three sectors, where the bend b_4 represents the end of the first sector, while ramp r_2 represents the limit of the second sector. The analysis allowed to determine the fully wet discharge (Q_{FW}) as the discharge that fully submerges all the bar crests and the fully transporting discharge (Q_{FT}) as the discharge at which the cross section is expected to fully transport material as bed load.

Discharge values corresponding to $\beta_{critical} = \beta_C$ and $\beta_{resonant} = \beta_R$ have been calculated using the analytical solution of free bars in straight channels of *Colombini et al.*, 1987.

4.2.3 Summary of the observed properties of alternate bars and of the emerging research questions

The reach between the Landquart and Ill confluences includes approximately 40 bar units and, through the high temporal and good spatial resolution of the Landsat dataset, their recognition is unambiguously determined (Chapter 3). In the case of images taken with different discharge conditions, bar exposure is largely changing, up to the limit case of images taken with complete coverage of water [*Adami et al.*, 2014]. The presence of ramps and bends along the reach plays a role in determining the bar properties as presented in Figure 4.7.

Figure 4.7 shows three different properties of bars expressed in dimensionless form, as a function of the longitudinal coordinate of the river reach. In detail, Fig. 4.7a shows observed spatial variability of the dimensionless bar wavelength L/W along the alternate bar reach. According to the observed behavior of L/W, the reach can be divided mainly in two sub-reaches, one upstream down to bends four and five, the second one downstream these bends until the Ill confluence. In the upstream sub-reach bar wavelength is larger ($L/W = 12 \div 17$, $\lambda = 0.18 \div 0.26$), with some wavelength oscillations in correspondence to bends or ramps. Fig. 4.7a reports all the bar wavelengths of each image of the Landsat dataset 1984-2013 so that the vertical oscillation of the data can be referred to the bar elongation or shortening in time as well as to the discharge effect already mentioned. The central and downstream sectors are generally characterized by a lower bar wavelength, with values in the range $L/W = 6 \div 12$ ($\lambda = 0.26 \div 0.52$).

Fig. 4.7b presents the ratio between the bar elongation and the river width ($\Delta L/W$) in the period 1999-2010. As for the previous case, according to the observations on bar elongation, the reach can be divided in two main sub-reaches with the same boundaries as above. The upstream sub-reach is characterized by vanishing or small elongation, with relative maxima and minima in correspondence to bend 3 and bend 4. The values are almost always in the range -1 ÷ 1. In the central and downstream sectors, greater elongation and shortening are present. In particular, af-

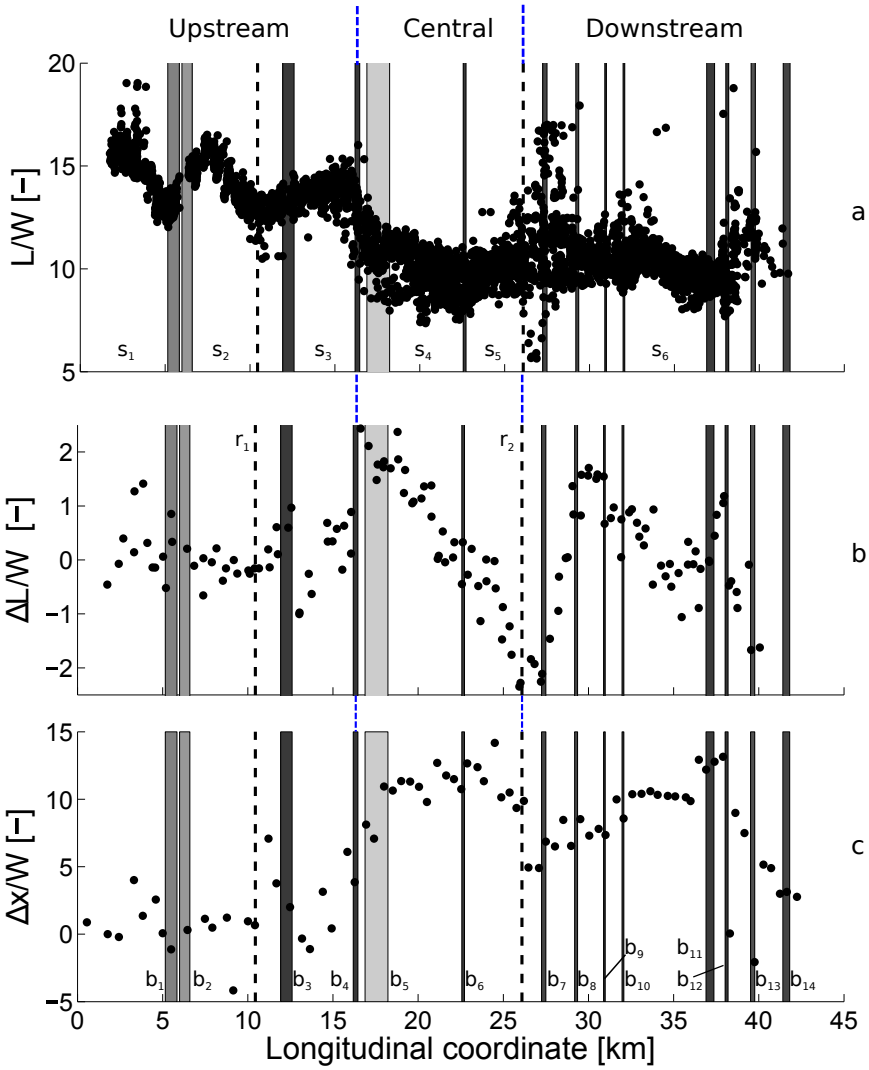

Figure 4.7: Different alternate bar properties as a function of the longitudinal coordinate of the Alpine Rhine reach shown in Figure 4.6. From up to down are shown respectively the ratios of the bar wavelength over the width, the bar elongation over the width and the bar migration over the width.

ter bend 5 maximum elongation is shown with values on the order of $\Delta L/W \approx 2$. For a channel length of approximately 8 km downstream a nearly linearly decreasing trend of bar elongation is present until ramp

2-bend 7 up to values of -2.

A sudden change is brought by a series of planform discontinuities located immediately downstream ramp 2 (r_2), after which elongation again recovers values near 2 downstream bend 8. Further downstream, elongation shifts to values near zero. The last part of the downstream sub-reach has again elongation values oscillating in the range -1 $\div$ 1, with relative maxima in correspondence to the last series of nearby bends.

Fig. 4.7c shows the longitudinal variation of the bar migration scaled with the river width ($\Delta x/W$) in the period 1999-2010. The main reach can again be divided in two main sub-reaches, with bend 3 setting the main divide between the upstream and downstream sub-reaches. In the former, migration is nearly zero, with few outsiders. Downstream bend 3 migration rapidly grows, up to values $\Delta x/W = 10 \div 15$. Downstream bar migration is nearly homogeneous in space, in this downstream sub-reach, apart from a slight local reduction that is observed in the neighbourhood of river km 30 and 40, where two distinct sequences of nearby bends are present and the straight reaches are relatively short.

4.3 Results: application of bar theories

4.3.1 Computation of theoretical parameters

Dimensionless parameters β, θ, d_s have been calculated as a function of the discharge in order to obtain the range of variability of each parameter with the discharge. In particular β and d_s are decreasing with discharge, while the Shields parameter θ, expressing the shear stress, is proportional to the value of discharge. In Figure 4.9 each parameter is shown in three different sub-reaches of the Alpine Rhine river. Furthermore these parameters are calculated on the base of the theoretical hypothesis.

Landsat images taken on different dates and with different stage flows can be used as base to define a flow rate curve per point. The available dataset allows to distinguish sections partially wet from sections fully wet, as it is reported in Figure 4.10. This analysis can provide a first estimate of wet width, directly from image analysis, and of bar amplitude, indirectly as described in the following sections. Once the amplitude is

Figure 4.8: Two different reaches with alternate bars in the Alpine Rhine river. The upper one shows alternate bars of the upstream reach of Figure 4.6 (*Source:* "Alpine Rhine":, 47Âř1'58.75"N, 9Âř29'32.43"E. **Google Earth.** February 04, 2012. January 7,2016) the lower one refers to the central part of the reach (*Source:* "Alpine Rhine":, 47Âř7'10.92"N, 9Âř30'54.28"E. **Google Earth.** February 04, 2012. January 7,2016). Different bar wavelengths and different shapes are visible from the aerial images. Water flows from left to right, width of the river is around 95 m in both the images.

estimated, the corresponding fully transporting discharge is obtained. In Figure 4.10 the role of the real cross sections in determining a region of partial transport is shown. With respect to rectangular sections, in which we are always in fully wet conditions,, there is a first stage in which only a partially wet section is present. The fully wet stage (Q_{FW}) corresponds to a partially transporting section. Fully transporting section is defined as the section in which more than 90% of the wet section is transporting material as bed-load. The threshold of fully wet and fully transporting section is different assuming rectangular or real cross sections. Herein, the threshold of the fully transporting discharge refers to the case of real cross sections, in particular the Q_{FW} and Q_{FT} thresholds are lower for the case of rectangular cross sections. To calculate this value, a partition method, or Engelund/Lotter method [*Lotter*, 1933] is adopted. The Meyer-Peter and Müller formula [1948] has been used as a reference for the threshold value of θ_{cr}, the critical Shields parameter.

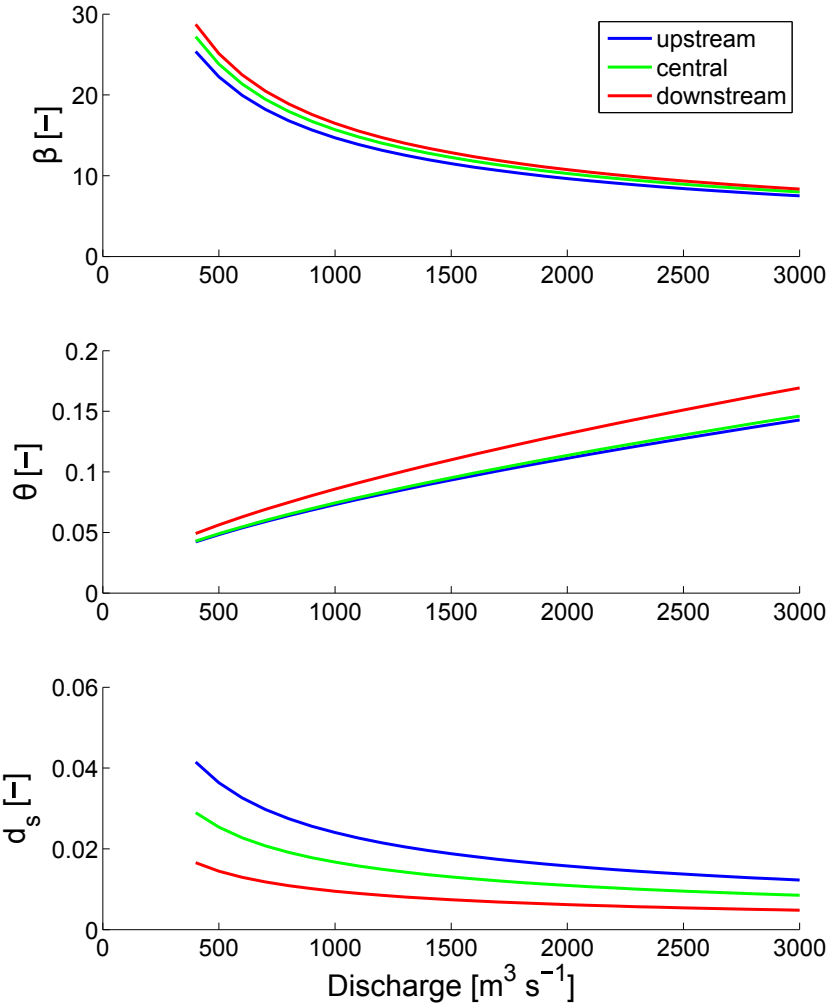

Figure 4.9: The three theoretical parameters β, θ, d_s as a function of the discharge. Each plot contains three curves, respectively representing the representative values of the upstream, central, and downstream sectors of the Alpine Rhine study reach.

Critical and resonant values (shown in Figure 4.11) of wavenumber λ and width ratio β have been evaluated for each sector described in Table 3.2. Different discharges have been used, starting from the fully wet one

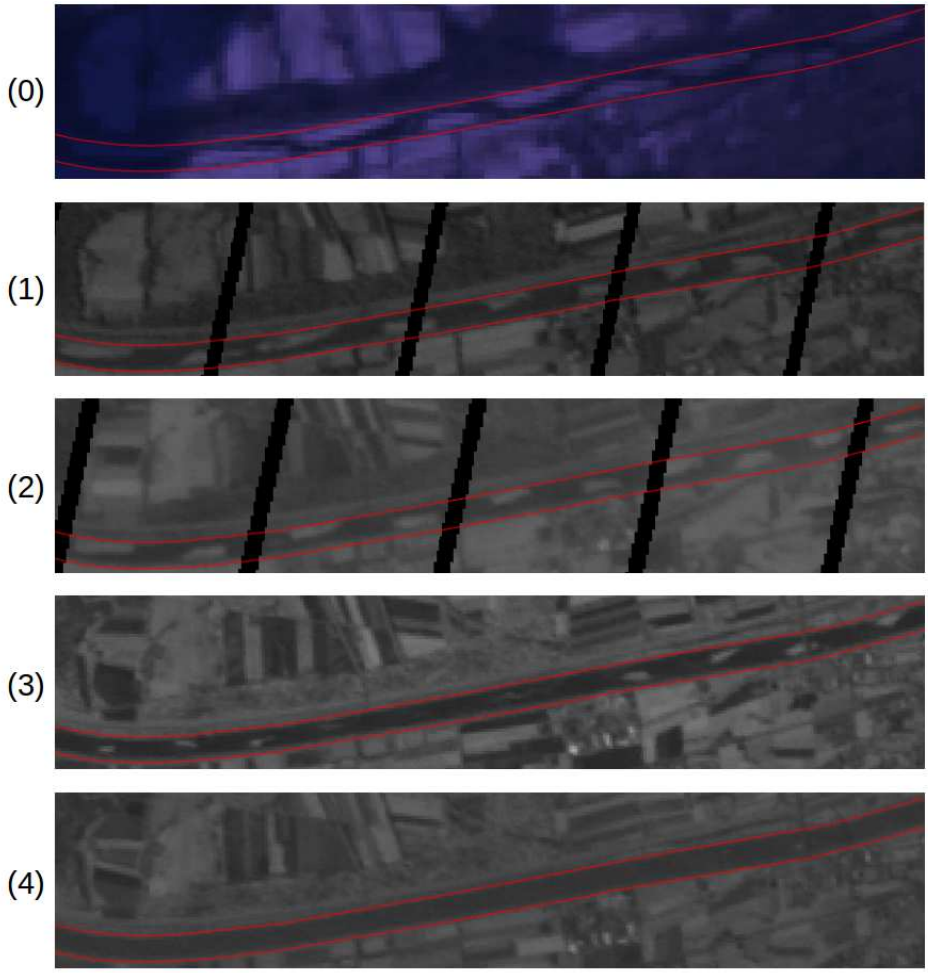

Figure 4.10: Comparison of Landsat images taken at different discharges. Image (0) is the minimum discharge of the Landsat dataset (L5 1990 Gen 14 Q=27 m^3/s). Image (1) to (4) present respectively Q=101 m^3/s (L7 2005 Oct 10), Q= 190 m^3/s (L7 2006 Jul 05), Q=287 m^3/s (L7 2000 Jun 02), Q=461 m^3/s (L7 2000 May 17).

(Q_{FW}) to the 2-year flow (Q_2). Critical and resonant values are then calculated up to the 100-year flow (Q_{100}=2160 $\mathrm{m^3 s^{-1}}$). Increasing values of discharge, critical values of λ increase from 0.32 and 0.40 ($Q = Q_{FW}$), respectively in the upstream and central-downstream sectors, to 0.45 ($Q = Q_2$). In the interval $Q_2 \div Q_{100}$, λ_C shows a relative maximum near 0.46. The difference between two successive critical points $((\lambda_{cr}, \beta_{cr})(Q_{i+1}) -$

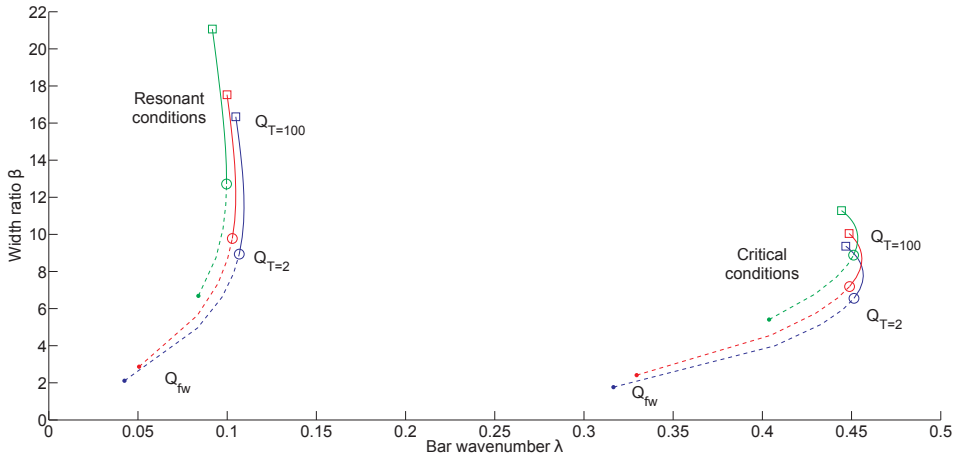

Figure 4.11: Analysis of the behaviour of the critical and resonant values of wavenumber λ and aspect ratio β for the three cases described in Table 3.2 for different discharges. Dashed lines represent the interval of discharges from the fully wet case (Q=450 m^3s-1) to the formative case (Q=905 m^3s^{-1}, T= 2 years). Continuous lines represent the interval of discharges from T=2 years to T=100 years (Q=2159 m^3s^{-1}). Blue lines represent the Rhine Upstream, red lines the Rhine Central, green lines the Rhine downstream.

$(\lambda_{cr}, \beta_{cr})(Q_i))$ decreases with increasing Q of a same quantity ΔQ.

Similar results are shown for the case of resonant values of λ and β. Increasing discharge, resonant values of λ increase from 0.05 (Rhine upstream and Rhine central) and 0.08 (Rhine downstream) for the fully wet discharge to around 0.10 (all the cases) for the 2-year case In the interval from 2- to 100-year discharge, λ shows a relative maximum around 0.11.

The domain of β is double for the resonant case compared with the critical one so that the sub-resonant region $\beta_{res} > \beta > \beta_{cr}$ tends to increase with increasing discharge.

4.3.2 Application of bar theories

The following bar theories were applied to predict bar properties and to support interpretation of the field observations: the linear theories for free migrating bars, and for forced steady bars, in the versions proposed by *Colombini et al.* [1987] and by *Zolezzi and Seminara* [2001]; the non-linear

theories for free migrating bars of *Colombini et al.* [1987] and of *Tubino* [1991].

First of all, the reach-averaged lower discharge limit for fully transporting cross-sections was computed to establish the meaningful discharge range for theory application. The fully transporting discharge Q_{FT} ranges between $500\,\mathrm{m^3s^{-1}}$ and $800\,\mathrm{m^3s^{-1}}$ in the different sub-reaches (Table 3.2).

The linear theory for free migrating bars is applied to predict the conditions of free bar occurrence and their wavelength. This theory predicts free bar instability whenever the width to depth ratio β is higher than a critical threshold β_c, which depends on the shear stress and the average grain size roughness, and which generally ranges between 10 and 20. We computed the discharge value Q_{cr} that determines critical conditions ($\beta = \beta_c$), for each of the three reaches. According to the theory, discharge values below this threshold are likely to induce bar formation. Values range between $1850\,\mathrm{m^3s^{-1}}$ and $1950\,\mathrm{m^3s^{-1}}$ (see Table 3.2). This is the second relevant discharge threshold that sets the flow conditions under which alternate bar formation is expected. These two thresholds (Q_{FT} and Q_{cr}) are depicted in Figure 3.2, considering the values for the center sector. The figure shows that almost every flood is characterized by a peak value that falls in the area where alternate bars should form, according to *Colombini et al.* [1987]. During the considered time interval of 30 years, only two floods peaked above the critical threshold Q_{cr}. Overall, for 99.9% of the time when discharge exceeded the fully transporting threshold, the study reach was in a condition of free-bar instability ($\beta > \beta_{cr}$).

Results from the linear theory show that the most unstable wavelength for free migrating bars is approximately 750 m and remains almost constant along the study reach, despite varying sediment size and slope. Such predicted value is slightly shorter than the measured wavelengths of the alternate bars that were observed to migrate, which range from 750 to 1000 m. On the other hand, the computed wavelength of forced steady bars ranges between 2000 and 3200 m, i.e. almost twice as much as the observed wavelength (1200 to 1500 m) of the bars that have been classified as non-migrating in our analysis, which mostly occurred in the straight reaches of the upstream sector.

Values of bar height presented in Figure 3.12 were compared to the val-

ues of the free migrating bar equilibrium amplitude predicted by *Colombini et al.* [1987] and also by the empirical formulation proposed by *Ikeda* [1984], which estimates bar height as a function of sediment diameter and the width to depth ratio. In the *Colombini et al.* [1987] weakly non-linear theory with steady flow conditions, bar height is a function of flow and sediment characteristics, and of the distance from the critical conditions for free bar instability ($\beta - \beta_{cr}$). The two formulations give similar results, with bar height decreasing from upstream to downstream (ranging from 6.2 m to 4.8 m for $Q = Q_2$), and decreasing for higher discharges until disappearing when Q approaches Q_{cr}. Overall, the predicted range shows a fairly good agreement with the bar height values computed from the cross-sectional survey.

Finally, an application of Tubino's (1991) theory for free bar evolution under unsteady flow conditions was attempted. The predicted bar amplitude values by the *Colombini et al.* [1987] model assume that an equilibrium condition in time is reached. In a real river bars develop under a sequence of floods. Therefore, we assessed to which extent flow unsteadiness can affect the results of bar theories. The analytical non-linear model of *Tubino* [1991] allows the comparison of the relevant time scales of the morphological evolution and of the flood duration, through the dimensionless parameter U. The value of U computed for several floods occurred in the last 30 years in the Alpine Rhine is approximately 20, therefore falling in the case $U \gg 1$. This means that floods are short with respect to the time needed by free bars to grow to their equilibrium height. Moreover, this result suggests that the two floods (in 1987 and 2005) that peaked at a discharge larger than Q_{cr} did not have enough time to flatten the riverbed, resetting the bar configuration. This confirms our observations, which exclude the possibility that the alternate bars were flattened during the 2005 flood, as the bar configuration before and after the flood was remarkably similar, with most bars only slightly moving downstream (see also Figure 3.10a).

From the theory of *Struiksma et al.* [1985], *Crosato and Mosselman* [2009] derived a predictor for the bar mode m that describes the number

of bars per cross-section. The predictor reads:

$$m = \frac{\beta}{\pi}\sqrt{(b-3)\, f\,(\theta_0)\, C_f}, \tag{4.1}$$

where b is the degree of non-linearity in the relation between sediment transport and depth averaged flow velocity. *Crosato and Mosselman* [2009] suggest that the nearest integer of bar mode m indicates the most probable number of bars per cross-section. The case of alternate bars is then predicted for values of m in the range $0.5 \div 1.5$. In the case of gravel bed rivers *Crosato and Mosselman* [2009] suggest $b = 10$. Using value of discharge in the neighbourhood of $Q_2 = 780\,\mathrm{m^3 s^{-1}}$, the predictor results in the range $0.89 \div 0.94$, respectively in the downstream and upstream sectors, matching well the case of alternate bar presence. A further analysis is performed for the sector downstream the confluence of the Ill river, where no bars are present. Using the same data of slope and d_{50} of the downstream sector with $W = 60\,\mathrm{m}$, the value of predictor m is 0.34, correctly out of the range of the existence of alternate bars.

To evaluate the length over which forced steady bars are linearly damped, or non-linearly under sub-resonant conditions, we apply the solution of *Zolezzi and Seminara* [2001] and derive linearly the damping ratio between the amplitude ($A(0)$) at the section of the permanent perturbation ($x = 0$) and the amplitude ($A(L)$) at $x = L$.

$$\begin{aligned} A(x) &= A_0 e^{\lambda_r x}, \\ A(0) &= A_0, \\ A(L) &= A_0 e^{\lambda_r L}, \end{aligned} \tag{4.2}$$

where λ_r is the real part of the eigenvalues λ_3 and λ_4.

The number of theoretical bar wavelengths ($2\pi/\lambda_i$), denoted with N_L in Eq. (4.3) over which the initial amplitude $A(0)$ is reduced to a fraction δA (with $0 < \delta A < 1$) can be computed as:

$$\begin{aligned} N_L &= \log \delta A \frac{\lambda_i}{2\pi\lambda_r}, \\ \delta A &= \frac{A(L)}{A(0)}. \end{aligned} \tag{4.3}$$

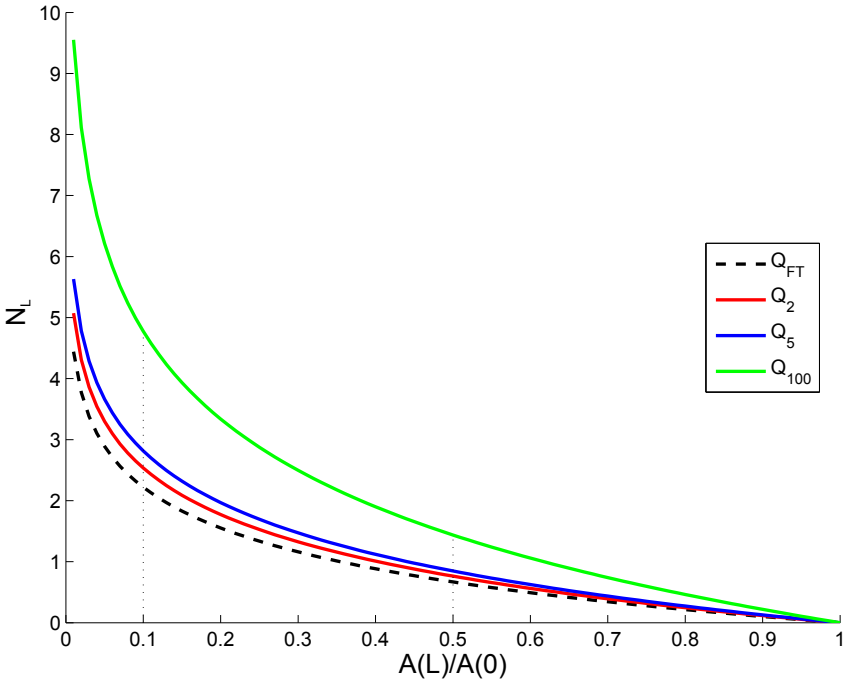

Figure 4.12: Length of the damping rate in number of wavelengths for different values of discharges.

where λ_i is the imaginary part of the eigenvalue λ_4. Fig. 4.12 shows the behaviour of the damping length in terms of the number of wavelengths N_L for different values of discharge (from $Q = Q_{FT}$ to $Q = Q_{100}$). Values of λ_r and λ_i are calculated using geometrical values of the central sector of the Alpine Rhine. The number of wavelengths is not changing much in the range $Q_{FT} \div Q_5$. Ratio $A(L)/A(0) = 1$ means no damping rate, while values of the ratio $A(L)/A(0) < 1$ correspond to $N_L > 0$ in the streamwise direction. A damping rate of $0.5A_0$ corresponds to nearly one theoretical steady bar wavelength, while a damping rate of $0.9A_0$ corresponds to $2 \div 3$ wavelengths. A comparison with field data is taken downstream bend b_4, where conditions shift from non-migrating to migrating and from longer to shorter bars. A damping rate of $0.9A_0$, nearly 3 wavelengths, with the data of the Alpine Rhine, corresponds to nearly 5 km.

4.3.3 Insights emerging from the application of the bar theories

The results of the present work show that several bar properties occurring over a 3-decade period in a long ($>$ 400 channel widths) reach of the Alpine Rhine are correctly predicted by analytical bar theories. Four main findings can be highlighted in this respect: (i) alternate bars are always found in straight reaches where linear theories predict both free migrating and forced steady bars to occur; (ii) there is a quite clear distinction between a nearby group of "long" bars always occurring in the upstream sector and other nearby groups of "short" bars, occurring in the longest straight reaches of the downstream sector. The long bars are steady, while the short bars migrate (see Figure 3.11), in agreement with linear theories for both free and forced bars in straight channels; (iii) the wavelength of migrating bars is well predicted by the linear theory for free bars in straight channels; (iv) the observed bar amplitude is consistent with the prediction of the weakly non-linear free bar theory.

At the same time, discrepancies between observations and predictions can be highlighted. These may help understand to which extent simplifying assumptions used in theories may limit their predictive ability. According to linear theories both free migrating and forced steady bars can occur in the upstream and in the downstream sectors of the study reach, while observations suggest a spatially selective behavior, whereby long steady bars occur upstream and short migrating bars only downstream. Moreover, the observed length of steady bars in the upstream straight reaches is shorter compared to the predictions of the linear theory for forced steady bars. We suggest that such discrepancy may be related to the effects of some of the assumptions on which the theories are built, which simplify the actual complexity of the real systems and allow focusing on "key" physical effects supposed to act as major controls on bar morphodynamics. Clarifying what theories can and what they cannot predict is important to better illustrate how they effectively can be used to interpret field observations. In the following we focus on: (i) the unsteadiness of the flow; (ii) the finite length of straight reaches and (iii) the heterogeneity of the grain size.

Flow unsteadiness. Application of *Tubino* [1991] non-linear theory for

free migrating bars in straight channels indicates that the time scale of flow unsteadiness is much shorter compared to the morphological time scale needed for free bars to reach their equilibrium amplitude. This underpins the possibility to use the assumption of steady flow. Under this hypothesis, the linear free bar theory correctly predicts the wavelength of migrating bars, which is also known to be almost unaffected by non-linear effects (*Colombini et al.* [1987]), and does not show significant changes during the 30 years of observation. Therefore, despite the observed alternate bar configuration was generated by the action of a long lasting ($>$ 150 years) sequence of unsteady flows, the present analysis strongly suggests the validity of assuming a constant, rather a narrow range of bar-forming values of discharge to predict the condition of occurrence and the wavelength of migrating bars. On the other side, floods with the same intensity and duration can determine different migration properties of the same bar units: flow unsteadiness might then be relevant at shorter time scales (i.e. flood event), in locally reshaping and moving individual bars.

Finite reach length. The linear theory for free migrating bars is obtained referring to an infinite channel length, where a periodical analytical solution is derived in the streamwise direction. An analogous assumption characterizes the linear theory for forced steady bars, where the channel length is assumed infinite only in one direction, with an upstream (or downstream) boundary where a local persistent perturbation of the straight, equiwidth channel geometry is present. The reported observations may help define a minimum reach length that can satisfy the (semi) infinite length condition. Our study site included a total of six straight reaches (three in each main sector) longer than approximately 2 km, i.e. 3 times the predicted free bar wavelength. Every straight reach is bounded upstream and downstream by local planform perturbations consisting of bends, ramps, confluences, which force steady bars in the nearby straight reaches. Only in some of the straight reaches, namely the three ones located in the downstream sector, migrating bars can be observed. *Jaballah et al.* [2015] observed migrating bars in a 2.3 km long ($\sim$ 45 channel widths, or $\sim$ 4 times the longest bar wavelength) straight reach of the Arc River in France, bounded by an upstream bend and by a downstream asymmetrical bridge pier. In their study, the number of migrating bars decreased with

time. The migrating bars observed by *Eekhout et al.* [2013] occurred in a longer straight reach (in terms of bar wavelengths), while the secondary channel of the Loire River where alternate bar migration was observed by *Rodrigues et al.* [2015] is not longer than 2 bar wavelengths. The above observations suggest that a straight reach length of several times the free migrating bar wavelength might be a necessary though not a sufficient condition for migrating bars to occur.

Sediment size heterogeneity. Another simplifying assumption in the examined theories is the uniformity of grain size. The mathematical modelling and experimental works by *Lanzoni and Tubino* [1999] and *Lanzoni* [2000a] showed that graded sediments cause migrating-bar elongation, as well as a decrease of the migration speed. Indeed, we observed also a much slower migration rate than that predicted by linear theories. In addition to the previous points, bar migration is affected also by non linear effects caused by bar amplitude. As a result, bar migration cannot be accurately predicted by linear theories, and weakly non-linear theories or numerical models are needed.

The awareness of how much the simplifying hypotheses of the theories may limit their applicability allows a more critical use of theories to interpret field observations. All of the observed bar wavelengths fall within the two limits set by linear theories for free migrating and forced steady bars in straight reaches. The range of variability of these limits is relatively narrow, when considering meaningful ranges for discharge, grain size, and channel slope (*Adami et al.* [2014]). Such analytically derived limits may therefore be viewed as the lower and upper boundaries of what can be actually observed in the corresponding real setting of straight river reaches. The alternate bars observed in the Alpine Rhine are likely to be the result of a non-linear interaction between the two types of bars (free and forced) predicted by the theories. This is in agreement with the experimental and numerical results of *Crosato and Mosselman* [2009] and *Crosato et al.* [2011] and with the analytical studies referring to weakly meandering channels with constant width (*Kinoshita and Miwa* [1967], *Tubino and Seminara* [1990]) and to straight channels with spatially oscillating width *Repetto and Tubino* [2001]. We argue that the result of such non-linear interaction would eventually result into bars with wavelengths falling within

the limits predicted by linear theories. Interestingly, in the Alpine Rhine the observed migrating and steady bar lengths are closer to the computed limits for free and forced bars, respectively, which further supports this hypothesis. While the broad tendency can be therefore attributed to the physical processes already retained in the linear theories, further developments on the non-linear free-forced bars interaction in straight channels are needed to provide a complete picture of the controlling parameters and of the dominant effects.

4.4 Steady and migrating bars in the Alpine Rhine: why a spatially selective behavior?

4.4.1 Synthesis of observations

Figure 4.7 shows a markedly different behaviour between the upstream sector and the central and downstream sectors in terms of bar wavelength, migration and elongation. The spatial trends of these parameters also point out the role of bends and ramps, which can be viewed as persistent local perturbations connecting relatively long straight reaches.

In the long straight reaches ($s_4 \div s_6$) of the central and downstream sectors, bars migrate downstream (4.7c), change their length over time (4.7b) and their wavelength (4.7a) remains consistently shorter compared to the upstream sector, where bars are fundamentally steady, because they neither migrate nor modify their wavelength.

Planform discontinuities, especially bends, also seem to have different effects in the three sectors on the spatial trends plotted in Figure 4.7. The three bends of the upstream sector do not seem to affect much the observed bar migration and elongation, despite that some local scatter can be observed in the data. The local mean value of bar wavelength displays some spatial oscillations in the upstream sector but local minima and maxima almost never coincide with the presence of bends. Only the second minimum is located in correspondence of ramp r_1, which is high enough to literally separate subsequent bar units. In the central and

downstream sectors, after a localized reduction immediately downstream of bends b_4 and b_5, the mean bar wavelength remains almost constant. In correspondence of the two groups of nearby bends located upstream and downstream the (sixth) long straight reach, the spatial variability of the bar wavelength locally increases (4.7a). The same two groups of bends are also associated with a local reduction of bar migration (4.7c). Also bar elongation shows a similar trend in the central and downstream sectors: bars tend to elongate immediately downstream of a significantly numerous group of nearby bends (like bends 4-5 and $6 \div 9$); such elongation gradually reduces along straight reaches and eventually turns into shortening (e.g. long straight reach 5). This trend is interrupted at the end of the long straight reaches.

4.4.2 Development of possible interpretations

We now develop possible explanations for the observed differences in bar morphodynamics between the upstream and the central-downstream sectors.

The study site is characterised by rather homogeneous conditions in the streamflow and sediment supply regimes and no differences are evident in terms of river bed and sediment management along the study reach in the considered 30 years. This suggests to look for possible explanations in terms of predictions of analytical theories for river bars, which allow to estimate the variability of bar properties under different hydraulic conditions.

Free and forced bars theoretically develop in long straight reaches in which the bed is at least locally transporting sediment (as bed-load). A further condition for the development of free bars is that the width ratio is larger than the threshold value β_C. This fix as the lower (Q_{FT}) and upper (Q_C) limits of the water discharge within which free bars can develop (see Fig. 4.5 for an ideal case and Fig. 4.13 for the case of the Alpine Rhine in two distinct regions: upstream and downstream the confluence of the Ill river). Forced bars need a further ingredient determined by the presence of a fixed obstacle in the straight reach. Long straight reaches (say $L/W > 20$) are present in all the three sectors, as well as fixed obstacles like ramps (see Fig. 4.7a,b). From the outcomes of the bar

theories presented in Section 4.3.2, it appears that both types of bars can theoretically be present in every sector.

As already described in Ch. 3, the relations between bar migration and wavelength in the upstream and central-downstream sectors are in general agreement with the predictions of the linear theories for migrating and steady bars in straight channels. On the opposite, from the analysis of the field data, the upstream sector seems to be characterized by forced steady bars, and central-downstream sectors by free migrating bars. How can this be explained, if they both can exist in all sectors?

The length of straight reaches plays an important role for both free and forced bars: the shorter the reach is, the less the probability to find free bars and, on the opposite, the higher the likelihood to see forced bars in both sub- and super-resonant conditions. Also hydraulic conditions (β, θ, d_s) must play a role because both free and forced bar properties depend on them: they set the limit of bed-load transport and the thresholds for sub- and super-critical and sub- and super-resonant conditions). Since we are always in super-critical conditions for free bars (see the limit between the green and red band of Fig. 4.13a,b), the most important limit appears to be that on the properties of forced bars, because this theoretically sets two markedly different morphodynamic regimes that characterise the channel behavior under sub- and super-resonant conditions.

On the basis of this, we formulate 3 hypotheses as possible explanations:

1. **differences in channel geometry.** The presence of forced bars in straight channels is related to the presence of local persistent perturbations that alters the planform flow pattern. Bends with different curvature and length are present with similar characteristics in the three sectors. If lengths of straight reaches would be much different among the sectors, this could result in different morphological behavior: free bars theoretically develop sufficiently far from a persistent perturbation and a single wavelength is nearly 7 $\div$ 10 times the channel width. The minimum length that therefore allows the presence of a complete free bar wavelength for the case of the Alpine Rhine is then between 0.7 km $\div$ 1.0 km. The length of straight reaches depends on the position of bends, but both in

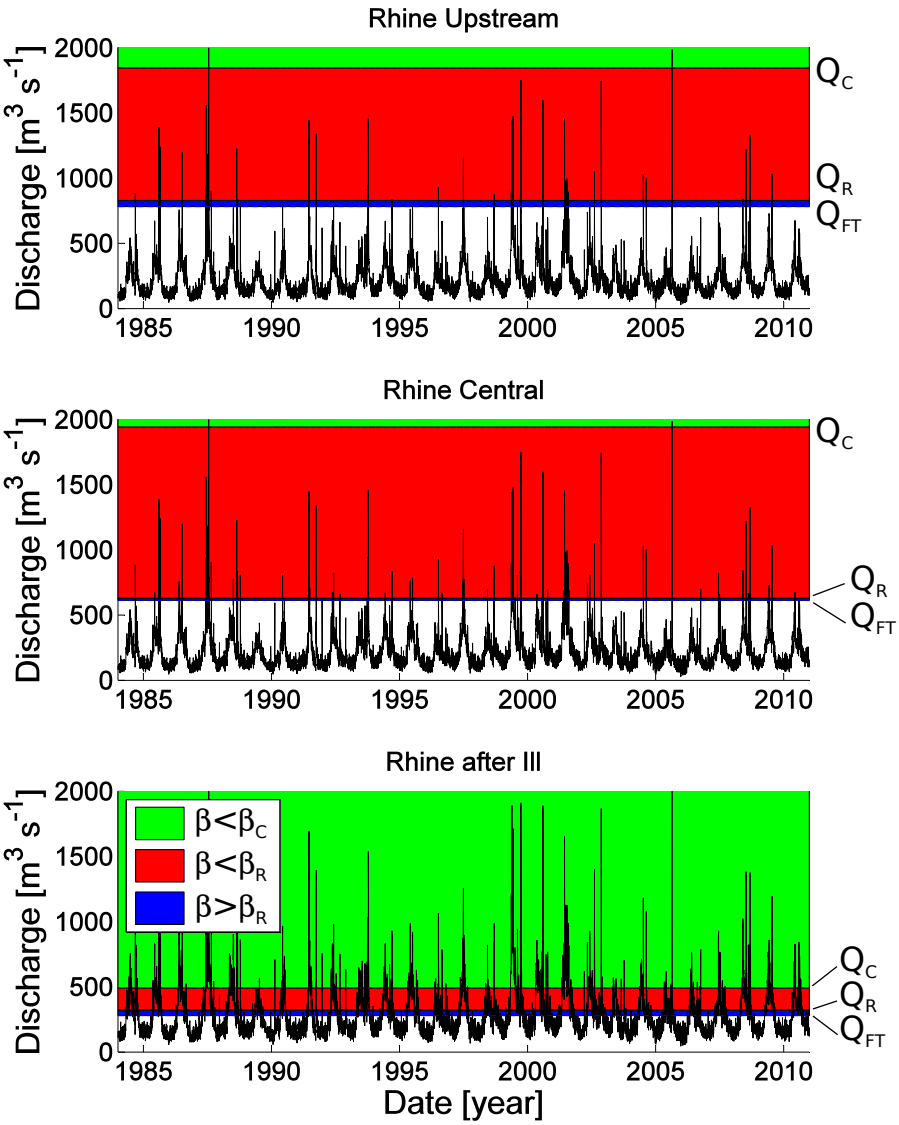

Figure 4.13: Sub-critical, sub- and super- resonant regions, respectively in green, red and blue, as function of the real hydrograph of the Alpine Rhine in three different cases: upstream sector (a), central sector (b) and downstream the confluence of Ill river (c).

the upstream, central and downstream sectors, the existing straight reaches have similar length, the longest being around km 3, km 20 and km 35. In particular, in the 42 km studied reach, we focus the attention on 6 straight reaches, defined in Fig. 4.7a. Following this line of reasoning, this hypothesis does not seem to provide a consistent explanation of the observed spatially selective behavior of bars.

2. **differences in properties of free bars.** The computed properties of free bars are rather homogeneous along the three sectors. From the results of the linear theory of free alternate bars, the most unstable wavenumber (relative maximum of growth rate Ω in Fig. 2.3), is nearly $0.4 \div 0.5$ for the three analysed sectors of the Alpine Rhine. It corresponds to downstream migration ($\omega > 0$) in the whole reach. Analysis of field data reflect scorrectly this behaviour only downstream bend b_5 in which the mean of the ratio L/W is nearly 10 and migration, in terms of the ratio downstream movement over width per year, is nearly 1 in the straight reaches s_4, s_5, s_6. Migration and wavelength of the reach upstream b_5 are respectively near zero and in the interval $13 \div 17$. Despite similar, theoretically predicted, free bar properties, therefore, bars display different migration properties in the upstream sector compared to the downstream and central sectors. The spatially selective behavior does not seem to be coherent with differences in free-bar properties among the reaches.

3. **differences in properties of forced bars.** The main parameter for a change in behaviour of forced bars is associated with the resonant conditions. Here two different cases are considered: the first one describes the streamwise behaviour of the parameter $(\beta - \beta_R)/\beta_R)$ for different values of discharge; the second one considers an analysis of the temporal persistence of each sector under the following conditions: sub-critical, sub-resonant and super-resonant.

   The former analysis, see Fig. 4.16, describes the behaviour of the parameter $(\beta - \beta_R)/\beta_R$, that gives a magnitude of the length of spatial influence (in the streamwise direction) of a permanent perturbation. The influence can be thought to be higher when such ra-

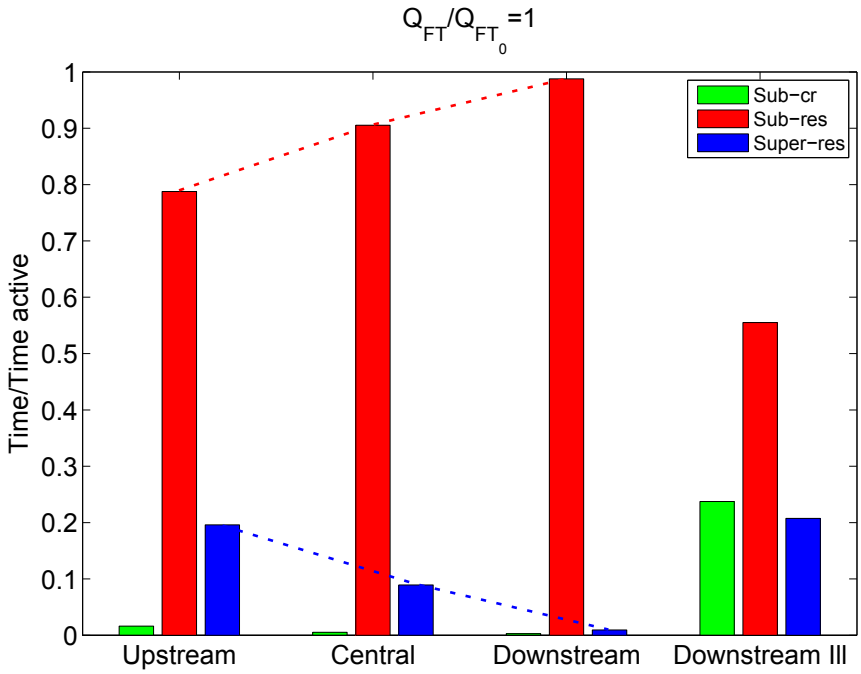

Figure 4.14: Histograms of the persistence under sub-critical conditions ($Q > Q_C$, in green), sub-resonant conditions ($Q > Q_R$, in red) and super-resonant conditions ($Q < Q_R$, in blue). Time is scaled with total active time of the 30 years hydrograph.

tio approaches zero (strictly infinite), while a perturbation decades rapidly for values of $(\beta - \beta_R)/\beta_R$ far from zero. In Fig. 4.16 the parameter is plotted for different discharge values. Q_{FT} and Q_5 produce values of the parameter respectively super- and sub-resonant in the whole domain, but without changing much between different sectors. The same behaviour is evident when a discharge near the resonant condition is chosen. This approach does not seem to be enough informative for the purpose of the analysis.

The second analysis aims to evaluate the cumulative temporal persistence of each sector under sub-critical, sub- and super-resonant conditions in the considered timeframe (1984-2013). In Fig. 4.14 and Fig. 4.15 such temporal duration (i.e., cumulative persistence) is scaled with the morphological time scale that comes from the Exner

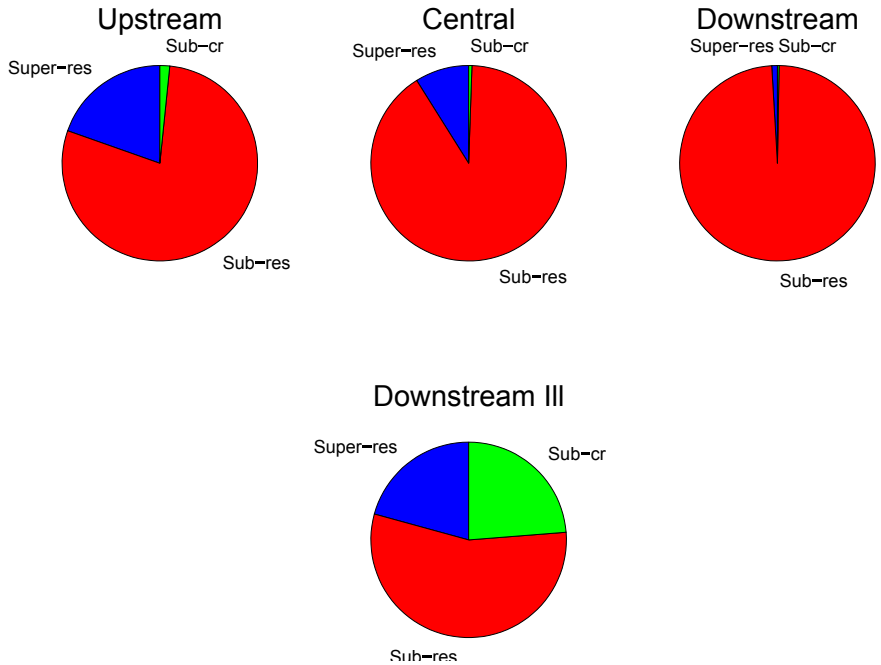

Figure 4.15: Proportions of the persistence under of sub-critical conditions ($Q > Q_C$, in green), sub-resonant conditions ($Q > Q_R$, in red) and super-resonant conditions ($Q < Q_R$, in blue). Time is scaled with total active time of the 30y hydrograph.

equation at the instantaneous flood discharge value, (Eq. 4.4). Temporal persistence under sub-resonant conditions (red) increases from upstream to downstream, while super-resonant temporal persistence (blue) decreases in the downstream direction. Sub-critical persistence (green) is almost negligible for the three sectors. This trend appears to be coherent with the observed bar behaviour in the field, in which the upstream sector presents steady bars with an amplitude and a wavelength close to those theoretically expected under super-resonant conditions, while central and downstream sectors present a behaviour coherent to what could be theoretically expected under sub-resonant conditions. In fact, sub-resonant conditions imply a streamwise downstream decay of the amplitude imposed by the persistent geometrical perturbation generated by bends. While super-

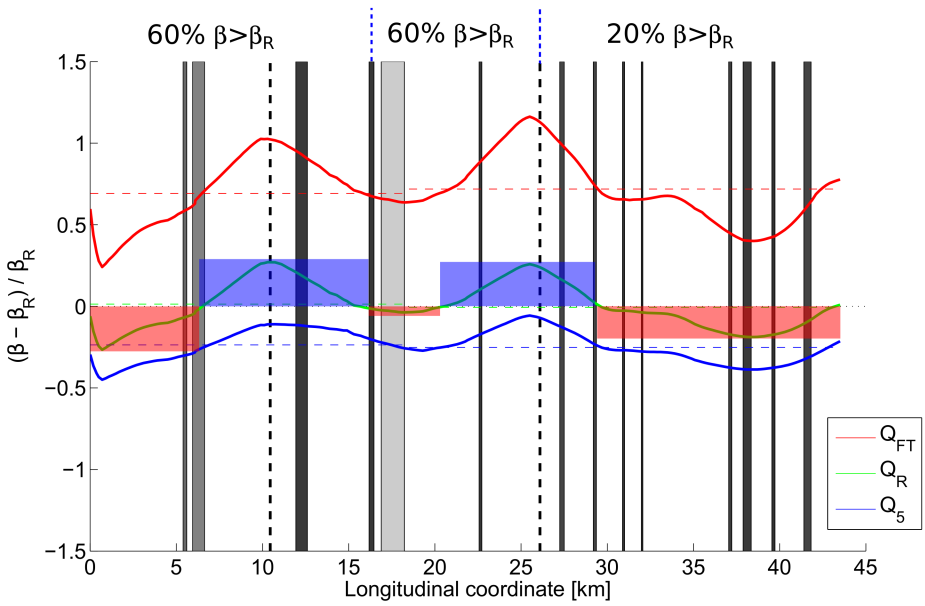

Figure 4.16: Behaviour of the parameter $(\beta - \beta_R)/\beta_R$ for 3 different values of discharge: Q_{FT}, Q_R, Q_5 in the Alpine Rhine reach. Red and blue regions represent respectively sub- and super-resonant conditions.

resonant conditions would imply a tendency towards an equilibrium amplitude of steady bars in space, 'forced' in the same straight reach by bends located both at its upstream and downstream end. This overall should 'fix' the whole bar geometry of the straight reach, which therefore would be subject to a steady bar behavior along the whole of its length, differently from its downstream straight reaches, where longer lasting sub-resonant conditions would determine shorter channel length along which the (downstream only) influence of upstream local perturbations is felt in the form of steady bars, thus leaving more space to the migrating bars that are actually observed. This behaviour is evident looking at the wavelength of bend b_4, streamwise decreasing up to wavelengths typical of free bars.

The total time for which $\theta > \theta_C$ (that corresponds to $Q > Q_{FT}$) has

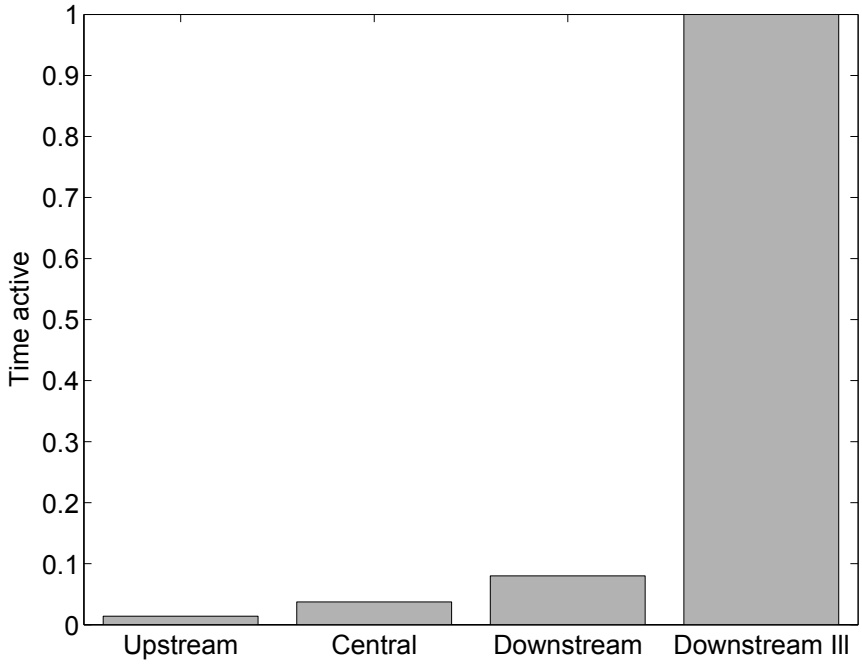

Figure 4.17: Histograms of the active time for the considered sectors and downstream Ill's confluence.

been calculated as:

$$Time\ active = T_a = \sum_i t_i \left(Q > Q_{FT}\right) \tag{4.4}$$

T_a scales the three times plotted in Fig. 4.14, that sum to unity. Moreover, it is interesting to observe that another different behaviour is evident for the reach 'Downstream Ill', in which the three times have a comparable duration, in particular sub-critical time is much larger than the reach upstream the Ill river. This is coherent with the observed absence of alternate bars in that reach. Moreover, T_a is sector dependent (see Fig. 4.17 in which T_a is scaled with the value of the Downstream Ill reach). In particular, the downstream sector is more active in terms of bed-load than the upstream and central sectors and T_a of the reach downstream the Ill's confluence is one order of magnitude more active than the previous reach.

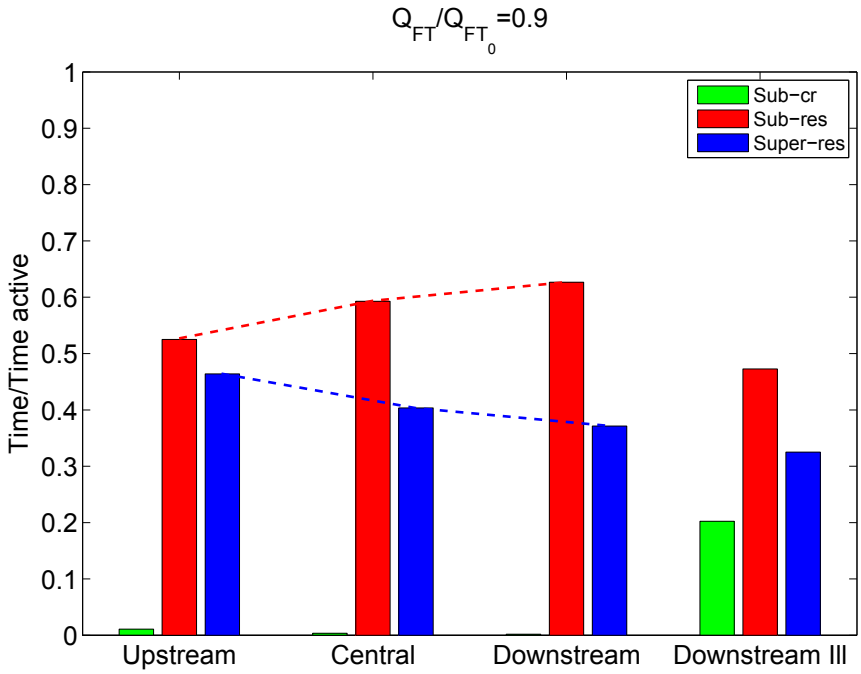

Figure 4.18: Histograms of the persistence under sub-critical conditions ($Q > Q_C$, in green), sub-resonant conditions ($Q > Q_R$, in red) and super-resonant conditions ($Q < Q_R$, in blue). Time is scaled with total active time of the 30 years hydrograph.

Fig. 4.18 and 4.19 illustrates the sensitivity of the previous result to the choice of the Q_{FT} value that is used to set the lower discharge limit of the applicability of analytical theories. They show the ratio between sub- and super-resonant times and sub-critical times. These different behaviors are presented modifying the fully transporting threshold, 0.9 times Q_{FT} in the former case and 0.8 times Q_{FT} in the latter case. From the comparison of the results with the ones of Fig. 4.14, the relative percentage of sub- and super- resonant times clearly emerges. In the case of $Q_{FT}/Q_{FT_0} = 1.0$ the sub-resonant conditions prevail, while in the case of $Q_{FT}/Q_{FT_0} = 0.8$ the super-resonant conditions prevail. The streamwise trend from super-resonant to sub-resonant conditions is not influenced by the choice of Q_{FT}, thus corroborating this third explanation to the qualitatively observed bar dynamics

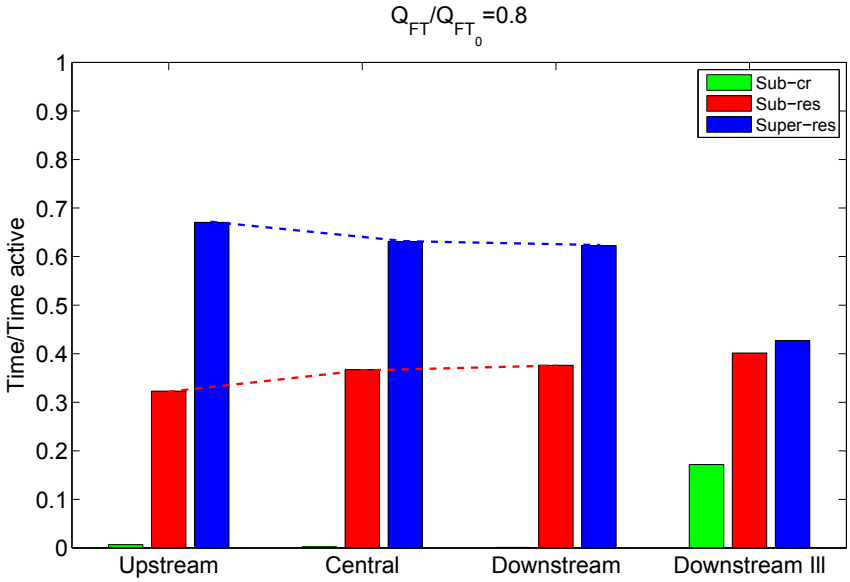

Figure 4.19: Histograms of the persistence under sub-critical conditions ($Q > Q_C$, in green), sub-resonant conditions ($Q > Q_R$, in red) and super-resonant conditions ($Q < Q_R$, in blue). Time is scaled with total active time of the 30 years hydrograph.

4.5 Discussion and conclusions

This chapter proposes an approach for the application of linear and weakly non-linear theories of free and forced alternate bars to field observations of field cases of straight channels (here the field case is represented by the Alpine Rhine reach).

The field case of the Alpine Rhine river, extensively reported in Chapter 3, is first taken as a comparison to evaluate the validity of analytical hypotheses. In particular, the behavior of the resonant and critical conditions is evaluated in terms of unsteady discharge, using the real hydrograph that considers a period of 30 years. Together with the two main conditions of the analytical models (critical and resonant) the threshold of the fully transporting discharge is considered. Fully transporting discharge is calculated starting from a theoretical rectangular section and from the cross sections of the field case, in which the same width is used. The difference between the two thresholds is evident: a theoretical value

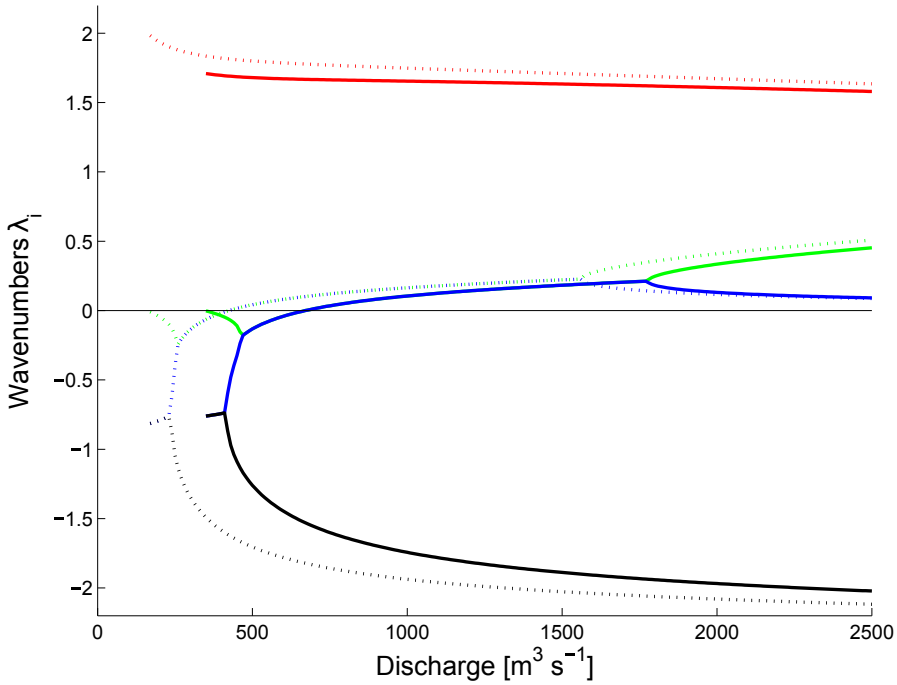

Figure 4.20: Behaviour of the imaginary part of the four eigenvalues as function of the discharge. Solid lines represent upstream sector, dotted lines represent downstream sector. Resonant conditions corresponds to $\lambda_i = 0$.

of $135\,\mathrm{m^3 s^{-1}}$ corresponds to a field value of $511\,\mathrm{m^3 s^{-1}}$ (downstream sector). Over the fully transporting discharge, the bed profile is considered active (i.e. fully transporting sediments), so the relevance in terms of the calculation of the time for which a sector is active is evident.

Based on the analysis of the application of analytical morphodynamic theories to observations on alternate bars in rectified rivers, the following synthetic conclusions can be drawn:

First, the main factor of variability in channelised rivers with alternate bars is chosen to be represented by the discharge $Q = Q(t)$, since other factors as width, slope, grain size are slowly varying in the longitudinal direction. The present approach introduces a new method that shows how to deal with varying discharge (i) in comparison with theoretical thresholds, i.e. fully transporting, critical and resonant conditions,

and (ii) introducing a new indicator, i.e. the ratio between the cumulate time percentage and the total active time. The issue remains open of the possible existence of a single, representative discharge value of the "morphodynamic signature" of the whole hydrograph- This issue is also dealt with in the next Chapter.

Second, comparing theories with observations highlights the key role of theories to aid interpretation of observations, giving the opportunity to better understand the morphodynamic processes controlling bar formation and dynamics. Moreover, it allows discussing how limiting are some of the simplifying hypotheses on which the theories are based.

Third, the study presents an apparently novel observation of alternate bar behavior in the upstream sector of the field case, followed by a behavior that is more coherent with the sub-resonant bar regime in the central and downtream sectors. This is coherent with the computed difference in the temporal persistence of the two sectors in the super- and sub-resonant regime, respectively. Such finding seems particularly interesting because very little evidence of differences in morphodynamic behavior under sub- and super-resonant regimes has been reported so far in real, albeit regulated, river systems.

Overall, the above result provides additional understanding of bar dynamics in channelized river reaches as they add new elements to the existing analyses that compare analytical theories with field observations, for which only few cases are actually present (e.g. *Welford* 1994; *Zolezzi et al.* 2012; *Eekhout et al.* 2013; *Jaballah et al.* 2015). These cases analyse only some aspects of the theories of free and forced bars. *Welford* [1994] quantitatively assesses the physically based non-linear mathematical theory of alternate bar formation under unsteady natural flow conditions in a straight alluvial stream, comparing his outcomes with the theoretical outcomes of *Tubino* [1991], in particular the bar amplitude and the ratio between the time scale of the flood and the morphology, through the parameter U. *Eekhout et al.* [2013] applied the models of *Tubino* [1991], *Struiksma et al.* [1985] and *Crosato and Mosselman* [2009] respectively to test the potential to predict the occurrence of bars in a field case of a 600 m straight channel of the Netherlands and to estimate the predictor m proposed by *Crosato and Mosselman* [2009] for the estimation of the

number of bars in a cross-section of the channel. *Jaballah et al.* [2015] applied the models of *Tubino* [1991], *Struiksma et al.* [1985] and *Crosato and Mosselman* [2009] with a sensitivity analysis of the two parameters I_p and b, respectively representing the interaction parameter between the adaptation length of the bed and the adaptation length of the flow, and the degree of non-linearity. *Jaballah et al.* [2015] presented in Fig. 9 the behavior of these parameters as function of the discharge for $m = 1$ and $m = 2$. They showed also that the length of decay for $m = 2$ is nearly $1/3$ with respect to $m = 1$. Moreover, the analysed stream (Arc river) seems to reflect a super-resonant regime in its formative conditions, but the correspondence with bar behavior is not analysed in detail, though signs of 2D upstream morphodynamic influence seem to appear upstream of the downstream end section of their study reach.

4.6 Conclusions

The dataset provided also useful information to assess the applicability of analytical bar theories, so far mainly tested against flume experiments, and following recent attempts in French and Dutch streams. Predicted values with linear theories for free and forced bars in straight channels are in good general agreement with field observations, when considering conditions of bar formation and bar wavelength. Comparing theories and observations suggests that theoretical outcomes may represent the boundaries of the actual, intermediate behavior of bars, which likely reflects non-linear interactions, flow unsteadiness, sediment size heterogeneity and finite length of straight reaches, which are not retained in linear theories. The comparison demonstrates the value of theories for the interpretation of field observations: for instance, the difference in the migration-wavelength relation may suggest the long, steady bars to be forced by local planform discontinuities and the short migrating bars to result from a free instability of the riverbed. Flow unsteadiness seems to have a minor role here while grain size sorting might affect bar wavelength and migration. Together with analytical theories set up to separately investigate both effects, a numerical analysis might also help to study bar dynamics subject to real flood sequences.

Despite the above limits, the work shows that bar theories not only provide information on bar geometry and dynamics, but they can also help interpret the physical processes at the basis of their occurrence, i.e., set a suitable framework to differentiate between free migrating or forced steady bars.

Chapter 5

Reproducing free and forced alternate bars with numerical models

This chapter is partly based on the monograph: "Alternate bars in straight domains", Laboratory of Hydraulics, Hydrology and Glaciology of the Swiss Federal Institute of Technology of Zurich.

5.1 Introduction

Morphodynamic numerical models represent a powerful scientific tool to enhance our understanding of river systems. Morphodynamic models are increasingly being used for different purposes, from managing river engineering problems to answering basic research questions. The research on involved topics is an important and socially relevant undertaking regarding our environment [*Siviglia and Crosato*, 2016]. Due to increasing computer power and the development of advanced numerical techniques, morphodynamic models are nowadays more and more used to predict the bed pattern evolution for a broad spectrum of spatial and temporal scales.

Several different numerical models have been tested to correctly reproduce the formation and development of alternate bars in straight channels (e.g. [*Takebayashi and Egashira*, 2001; *Defina and Lanzoni*, 2002; *Federici and Colombini*, 2002; *Defina*, 2003; *Bernini et al.*, 2009; *Crosato et al.*,

2011, 2012; *Siviglia et al.*, 2013]), but a benchmark analysis of the uncertainties and the comparison with the theoretical findings are still rare [*Siviglia et al.*, 2013].

Takebayashi and Egashira [2001] studied numerically the influence of multiple sediment size on alternate-bar formation and development. They found that non-uniform sediment forms bars with shorter wavelength, greater migration celerity and smaller height with respect to the uniform sediment case. *Defina and Lanzoni* [2002] analysed the stability of a train of bars under a periodic boundary condition. They found that the temporal variability of bar amplitude provides an indication of the equilibrium or non equilibrium state of the system. *Federici and Colombini* [2002] showed that bed perturbations generate a train of bars that behave as waves that migrate downstream increasing their amplitude in time as theoretically predicted by *Colombini et al.* [1987]. *Defina* [2003] investigated the influence of a local bed perturbation on the formation and development of alternate bars. The perturbation was either a single bump, periodic bumps in time or multiple bumps in space. In the case of periodic bumps in time, bar celerity was shown to depend on the frequency of the perturbation. On the contrary, values of bar celerity, bar wavelength and bar height are connected to one another, independently of the type of the initial perturbation. *Bernini et al.* [2009] focused on the role of the Froude number, analysing sub- and super-critical flow conditions as well as trans-critical conditions in the formation and evolution of alternate bars. They also investigated the role of gravity on sediment transport across bars and how this influences the dynamics of bars. *Crosato et al.* [2011, 2012] assessed the long-term evolution of alternate bars in straight channels, proposing a comparison between numerical simulation and a long-duration flume experiment. They found that migrating bars tend to become gradually longer and higher, then rapidly shorter and lower. Steady bars, generated from the upstream boundary, gradually developed in the streamwise direction suppressing the migrating bars. *Siviglia et al.* [2013] proposed a set of benchmark simulations used to test the capability of a numerical model to reproduce the main outcomes of the analytical theories, including free and forced bars. *Van Der Meer et al.* [2011] performed numerical simulations of upstream and downstream overdeepening in a 'U shaped' domain

as in the experiments of *Zolezzi et al.* [2005]. The morphological model Delft3D successfully predicted the overdeepening effect, although (i) the threshold between sub- and super-resonant condition was higher in the numerical simulation than predicted by *Zolezzi and Seminara* [2001] and (ii) at very high witdh to depth ratios the computed non-migrating bars are shorter than predicted by linear theory. *Mosselman and Le* [2015] describe the importance of a correct calibration of the deviation of the sediment transport direction from the depth-averaged flow direction to correctly represent the morphological evolution of the river bed with a numerical model. This effect has been explained in terms of linear stability analysis in A.3.

The aims of this chapter are (i) to test a new series of benchmark simulations for the calibration of the coefficient of transversal slope r proposed by *Ikeda* [1982] and (ii) to present one of the first cases of comparisons between multi-decadal field data of the Alpine Rhine river, presented in Ch. 3, and numerical data of the same reach, in simplified geometrical conditions, with a further analysis of different flow discharge conditions.

5.2 Shallow-water-Exner model: numerical vs analytical solutions

5.2.1 The numerical model Basement

We simulated the alternate bar formation in straight and curved domains using the fully non-linear, time-dependent, physically based numerical model for morphodynamic processes Basement [*Vetsch et al.*, 2016a]. The 2D module of the numerical model solves separately the hydrodynamics and the bed evolution. The hydrodynamics is based on the depth averaged mass and momentum conservation equations of the Raynolds-averaged 3D Navier-Stokes equations. The evolution of the bed topography is based on the 2D Exner equation that solves the sediment mass balance in streamwise and transverse coordinates.

The system of governing equations is solved through a finite-volume method on an unstructured triangular mesh. Different Riemann solvers are implemented, i.e. the exact Riemann solver, and two approximate

solvers (HLL and HLLC). In the simulations presented in this chapter the exact Riemann solver is used. Time discretisation is based on the explicit Euler first-order method, while spatial discretisation is carried out by the finite-volume method. The hydraulic time step is determined according to the restriction based on the Courant number. In the case of the 2D model, the condition Courant ≤ 1 is satisfied by choosing Courant$= 0.95$.

5.2.2 Numerical vs analytical solution: link between the two sets of governing equations and closure relationships

To directly compare the results obtained from the analytical theories with the numerical simulations, we make the following assumptions:

- viscous and turbulent stresses, as well as momentum dispersion terms are not considered in the system of equations proposed by *Colombini et al.* [1987] and *Zolezzi and Seminara* [2001];
- terms due to viscosity, turbulent stresses and dispersion are then neglected in the momentum equations;
- terms due to sediment material (s_g) and the source term in the Exner equation are neglected;
- the grain size distribution is considered uniform, so that only one class of sediments is considered.

The simplified formulation of the four governing equations is written along the longitudinal and transverse coordinates (x, y) as follows:

$$\frac{\partial h}{\partial t} + \frac{\partial \left(\overline{u}h\right)}{\partial x} + \frac{\partial \left(\overline{v}h\right)}{\partial y} = 0, \tag{5.1}$$

$$\frac{\partial \overline{u}}{\partial t} + \overline{u}\frac{\partial \overline{u}}{\partial x} + \overline{v}\frac{\partial \overline{u}}{\partial y} + g\frac{\partial h}{\partial x} + g\frac{\partial z_B}{\partial x} + \frac{1}{\rho h}\tau_{Bx} = 0, \tag{5.2}$$

$$\frac{\partial \overline{v}}{\partial t} + \overline{u}\frac{\partial \overline{v}}{\partial x} + \overline{v}\frac{\partial \overline{v}}{\partial y} + g\frac{\partial h}{\partial y} + g\frac{\partial z_B}{\partial y} + \frac{1}{\rho h}\tau_{By} = 0, \tag{5.3}$$

$$(1-p)\frac{\partial z_B}{\partial t}+\left(\frac{\partial q_B}{\partial x}+\frac{\partial q_B}{\partial y}\right)=0. \tag{5.4}$$

where:

h is the water depth;

g is the acceleration due to gravity;

$\overline{u},\overline{v}$ are the depth averaged velocities respectively in x and y directions;

z_B is the bed elevation;

τ_{Bx},τ_{By} are the bed shear stresses in x and y directions;

p is the material porosity;

q_B is the specific bed load flux.

Eqs. 5.1 ÷ 5.4 are compared with Eqs. 2.4 ÷ 2.7 proposed by *Colombini et al.* [1987]. The numerical model solves the unsteady regime through the presence of time derivatives in the continuity and momentum equations. These terms are neglected in the linear solutions proposed by *Colombini et al.* [1987] and *Zolezzi and Seminara* [2001], on the hypothesis that the flow field is always in equilibrium with a bed that slowly varies in time. The base of this 'quasi-steady assumption' lies in the difference on characteristic time-scales of bed and flow development (see e.g. *Vriend* [1981]).

The roughness parameter is computed by the model using the same closure of Chezy:

$$C_f=5.75\log\left(\frac{12R}{k_s}\right), \tag{5.5}$$

where the hydraulic radius R is approximated with the water depth and $k_s=3d_{90}$.

In the test-runs two different bed-load formulas have been used: Meyer-Peter and Müller formula [1948] and *Wong and Parker* [2006].

The numerical model corrects the direction of the sediment transport through a modification in the direction of the shear stress. The analytical

solution does the same. The formulation implemented in Basement [*Vetsch et al.*, 2016b] is written for the cases in which a transverse bed slope exists. The gravitationally induced lateral transport correction, for the case of a single grain class, is modelled using the approach proposed by *Ikeda* [1982] as presented by *Van Rijn* [1993]:

$$\frac{q_{B,lateral}}{q_B} = \beta \left(\frac{\tau_{B_{cr}}}{\tau'_B} \right)^{\gamma} S_{transverse}, \tag{5.6}$$

where $q_{B_{lateral}}$ and q_B are respectively the lateral transport component and specific bed load; β is a lateral transport factor (default value, up to version 3.5, is 2.05); γ is a lateral transport exponent (default value: 0.5). $\tau_{B_{cr}}$ is the critical shear stress of the individual grain class, τ'_B is the effective shear stress and $S_{transverse}$ is the bed slope in transverse direction.

This correction is compared with the formulation used by *Colombini et al.* [1987] (see Eq. A.10) and based on the analysis of *Engelund* [1981]. We obtain that factor β can be converted as follows:

$$\beta \sqrt{\tau_{B_{cr}}} = r \tag{5.7}$$

Then, setting $r = 0.3$ (e.g. [*Olesen*, 1984]) and $\tau_{B_{cr}} = 0.0495$, the corresponding value of β to be used in Basement, in the GUI input interface of the software named `lateral_transport_factor` in the `BEDLOAD-PARAMETER` block, is 1.3484.

Transverse velocity and transverse bed-load transport at the lateral boundaries are set to zero. Wall friction at the boundary is neglected, too.

5.2.3 Correction of local longitudinal slope

Basement implements per default in the calculations the corrections due to the longitudinal and transverse local slopes, that are not considered in the solutions of *Colombini et al.* [1987] and *Zolezzi and Seminara* [2001], but already introduced in the review proposed by *Tubino et al.* [1999] to be added to the critical value of the shear stress θ_C and written as:

$$\theta'_c = \left(\theta_c + \frac{r_1}{\beta} \frac{\partial \eta}{\partial s} \right) \sqrt{1 - \frac{(\partial \eta / \partial n)^2}{\tan^2 \phi}}, \tag{5.8}$$

where ϕ is the angle of repose of the bed material and coefficient r_1 ranges between $0.1 \div 0.2$. A full analysis of this subject is proposed by *Kovacs and Parker* [1994].

The role of local slope is implemented in Basement using a similar formulation:

$$\theta_c' = \theta_c \xi_x \xi_y, \tag{5.9}$$

where ξ_x represents the correction due to the local longitudinal slope $\partial\eta/\partial x$ and is defined as:

$$\xi_x = \frac{\sin\left(\gamma - \frac{\partial\eta}{\partial x}\right)}{\sin\gamma}, \tag{5.10}$$

while ξ_y refers to the correction due to the local transverse slope $\partial\eta/\partial y$ and is defined as:

$$\xi_y = \cos\frac{\partial\eta}{\partial y}\sqrt{1 - \frac{\tan^2\left(\frac{\partial\eta}{\partial y}\right)}{\tan^2\gamma}}. \tag{5.11}$$

γ is the angle of repose of the bed material. We analysed terms of Eqs. 5.10 and 5.11 expanding the slope in Taylor series, to evaluate their order of approximation. The local longitudinal slope results to be in the form $\epsilon + O(\epsilon^3)$, while the local transverse slope results to be in the form $1 - \epsilon^2 + O(\epsilon^4)$. Since *Colombini et al.* [1987] and *Zolezzi and Seminara* [2001] solve the 2D system of equations up to the order ϵ in the linear case and $\epsilon^{3/2}$ in the weakly non-linear case, the only correction that can be taken into account for the comparison is the one due to the local longitudinal slope.

The local longitudinal slope correction modifies the coefficients of the system of equations $2.4 \div 2.7$, in particular adding a new term to coefficient a_{44} of the homogeneous algebraic system of *Colombini et al.* [1987]. In particular, the coefficient with the corrections reads:

$$a_{44} = Q_0\left(\Phi_0\frac{r}{\beta\sqrt{\theta}}m^2\frac{\pi^2}{4} + \Phi_s\frac{\Phi_0}{s}\frac{\lambda^2}{\beta}\right) - \Omega_c \tag{5.12}$$

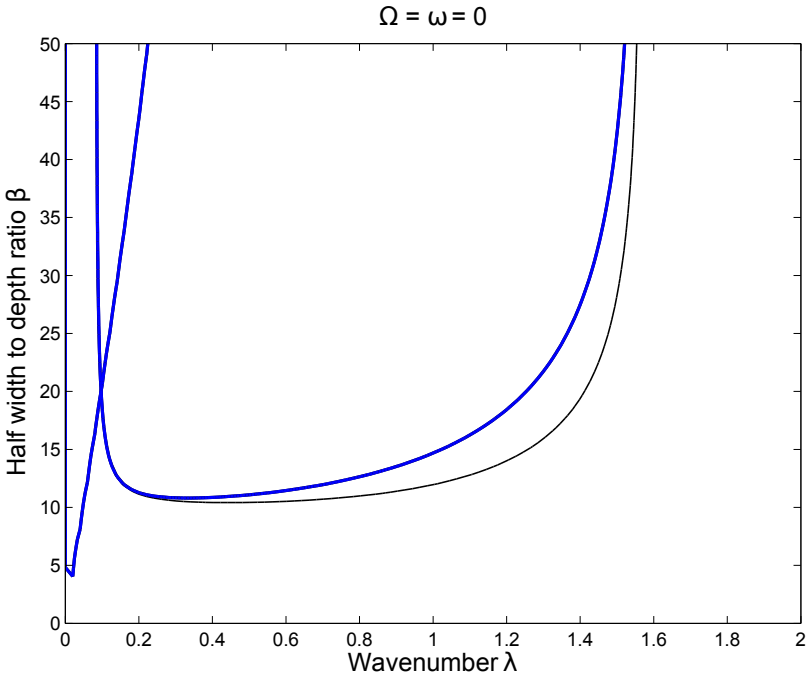

Figure 5.1: Effect of local longitudinal slope on the stability analysis of the solution of *Colombini et al.* [1987]. Corrected solution (solid blue lines) differs from the basic solution for high values of wavenumbers λ. ($Q = 2000\,\mathrm{m^3 s^{-1}}$, $d_{50} = 0.04\,\mathrm{m}$, $s = 0.002\,\mathrm{m/m}$, $W = 100\,\mathrm{m}$; Roughness: *Einstein* [1950], Bedload: *Meyer-Peter and Müller* [1948], r=0.3.)

where Φ_s is defined similarly to Φ_D and Φ_θ as:

$$\Phi_s = -\Phi_\theta \frac{\theta_c}{\theta} \theta_{c_s} \tag{5.13}$$

In Fig. 5.1 the comparison between the solution of *Colombini et al.* [1987] without the local longitudinal slope correction and with the correction (solid blue line) is presented. Dimensional data are the same as in Fig. A.3. The effect of the correction is evident for high values of wavenumber λ, or rather short bars. The typical plateau of the solution proposed by *Colombini et al.* [1987] is partially modified, while the critical and resonant values of the width ratio β remain almost unchanged. Finally, the role of the local longitudinal slope affects only the shape of the growth ratio Ω, while the angular frequency ω does not change.

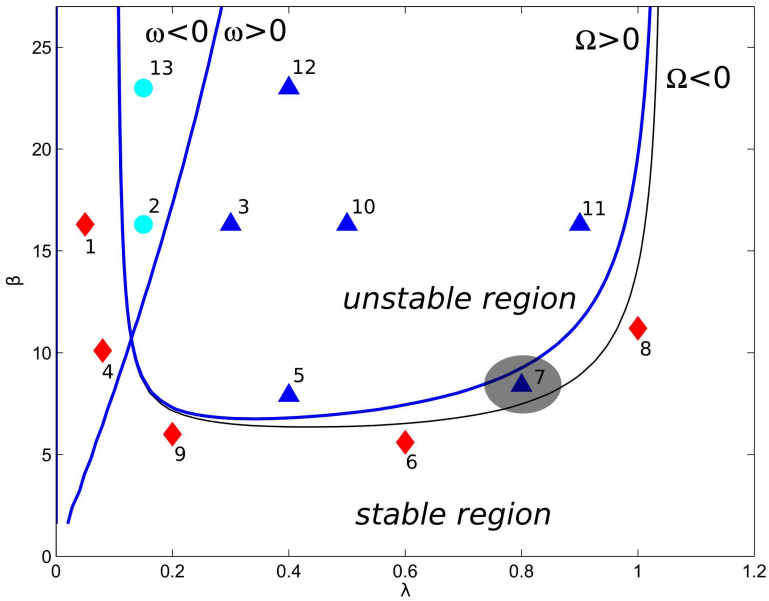

Figure 5.2: Formation of free bars in straight channels. Threshold curves for growth rate ($\Omega = 0$) and migration ($\omega = 0$) resulting from the linear analysis of *Colombini et al.* [1987] (black line) and with the correction of the local longitudinal slope (blue lines) are superimposed on the benchmark runs of the numerical simulations of Basement. Reference values of the parameters and closures: $\theta = 0.1$, $d_s = 0.061$, $r = 0.3$, $\Delta = 1.65$, soil porosity $p = 0.4$, roughness: *Einstein* [1950], bed-load: *Wong and Parker* [2006]. Colours of the runs are explained in detail in the text.

5.3 Benchmark simulations on alternate bar stability

To evaluate the capability of the numerical model Basement to correctly estimate the process of free-bar stability, the series of benchmark simulations proposed by *Siviglia et al.* [2013] is applied. This benchmark consists of 13 2D mobile-bed numerical simulations run at fixed values of parameters θ, d_s, coefficient r, relative density, soil porosity, roughness and bed-load formulae, but at different values of the parameters λ, β (see Tab. 5.1). Threshold curves for growth rate ($\Omega = 0$) and migration ($\omega = 0$)

resulting from the linear stability analysis of *Colombini et al.* [1987] set the base for the choice of λ, β combinations, in order to cover theoretical stability and instability cases (respectively at $\Omega < 0$ and $\Omega > 0$) as well as upstream and downstream migration (respectively at $\omega > 0$ and $\omega < 0$).

The original threshold curves of *Siviglia et al.* [2013] are modified, adding the correction due to the local longitudinal slope described in 5.2.3. The new thresholds are shown in Fig. 5.2, in which the original 13 runs are superimposed. Runs with red diamonds refer to cases of bar suppression, runs with blue triangles refer to cases of bar growth and downstream migration, runs with light blue circles refer to cases of bar growth and upstream migration. The main difference between the present analysis and the one proposed by *Siviglia et al.* [2013] is the expected behaviour of run 7, that originally was in the unstable region ($\Omega > 0$), while now it is in the region of bar suppression ($\Omega < 0$).

The set-up of numerical simulations consists of straight channels with initially a sinusoidally perturbed bed in the form:

$$\eta\left(x, y, t = 0\right) = A\left(t = 0\right) \sin\left(\frac{2\pi y}{W}\right) \cos\left(\frac{2\pi x}{L_b}\right), \tag{5.14}$$

where $A\left(t = 0\right) = A_0$ is the initial bar amplitude, set as 1% of the reference uniform flow depth, L_b is the given bar length, an inverse function of λ of Tab. 5.1. Constant flow discharge and solid discharge at a rate that is in equilibrium with the stream transport capacity are imposed as upstream boundary conditions, a uniform flow depth as downstream boundary condition. Banks are considered solid boundaries without roughness (slip walls). Numerical runs are carried out in a straight rectangular domain, 300 m long and 1 m wide. The computational domain has been discretized with 85990 triangular cells.

The hypothesis of linear growth rate and migration of the analytical solution is reproduced in the numerical model by setting a very short duration of the runs ($t_{run} = 100\,\mathrm{s}$), so that intrinsic non-linearities can not become relevant.

In Fig. 5.3 the left longitudinal profile of run 12 is shown. The red line represents the initial condition of the bed elevation ($t = 0\,\mathrm{s}$), set with the spatial structure of Eq. 5.14, while the blue line is the bed elevation configuration at $t = 100\,\mathrm{s}$. Bar growth in time and downstream migration

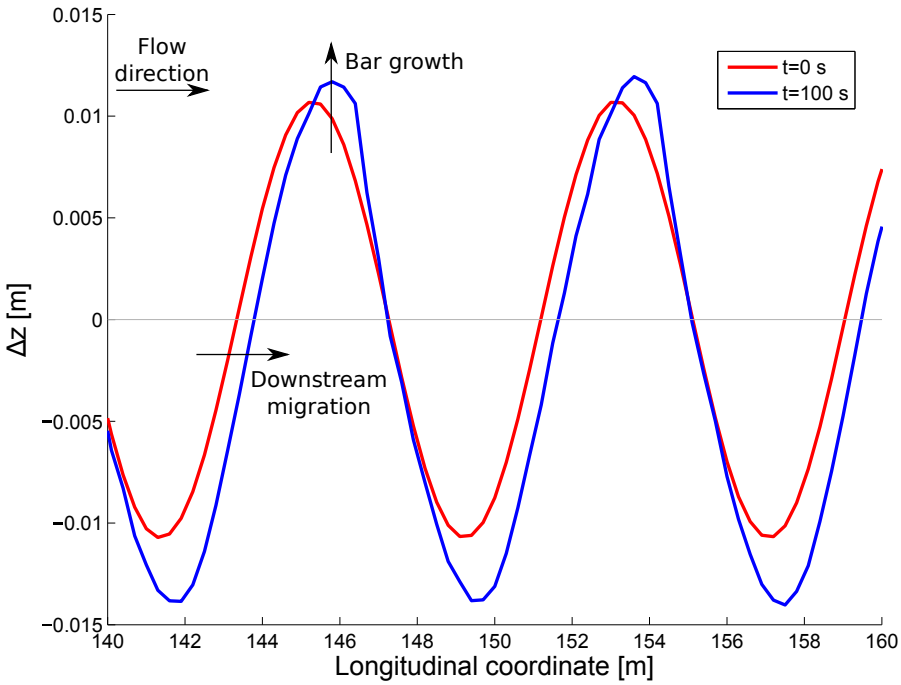

Figure 5.3: Example of benchmark run 12 for which theoretical growth in time and downstream migration are expected. The x-axis shows the central part of the domain, to avoid possible boundary effects.

are present. The theoretical scenario is here correctly reproduced. In Tab. 5.1 the comparison between the theoretical (subscripts '$_{CST}$') and numerical scenarios (subscripts '$_{BM}$') of the 13 runs in terms of temporal growth or decay ($\Omega > 0$ and $\Omega < 0$ respectively) and upstream or downstream migration ($\omega > 0$ and $\omega < 0$ respectively) are shown. Upstream and downstream migration are correctly estimated by the numerical model, while runs 5 and run 11 present behavior in disagreement with the free linear theory in terms of growth rate Ω. This suggests that the numerical growth rate threshold $\Omega = 0$ differs from the theoretical one: in Fig. 5.4 an hypothesis of the numerical threshold curve $\Omega = 0$ is shown and superimposed to the set-up presented by *Siviglia et al.* [2013]. This hypothesis implies a different critical condition for the appearance of alternate bars: $\beta_{C_{BM}} > \beta_{C_{CST}}$.

Table 5.1: Comparison between theoretical and numerical linear behaviour of benchmark simulations. Conditions $\Omega > 0$ and $\omega > 0$ are described with a '+', conditions $\Omega < 0$ and $\omega < 0$ are described with a '-'. In **bold** discrepancies are underlined.

Run n.	λ	β	Ω_{CST}	Ω_{BM}	ω_{CST}	ω_{BM}
1	0.05	16.3	-	-	-	-
2	0.15	16.3	+	+	-	-
3	0.30	16.3	+	+	+	+
4	0.08	10.1	-	+	-	+
5	0.40	7.9	**+**	**-**	+	+
6	0.60	5.6	-	-	+	+
7	0.80	8.4	-	-	+	+
8	1.00	11.2	-	-	+	+
9	0.20	6.0	-	-	+	+
10	0.50	16.3	+	+	+	+
11	0.90	16.3	**+**	**-**	+	+
12	0.40	23.0	+	+	+	+
13	0.15	23.0	+	+	-	-

The result of the numerical runs presented in Fig. 5.4 shows that the resulting threshold curve can be represented by the theoretical one together with an extra effect, whose nature is diffusive (i.e. tends to damp local bed perturbations).

In order to calibrate the numerical model to correctly reproduce the theoretical marginal curves, a new benchmark analysis is proposed for the coefficient r of lateral transport.

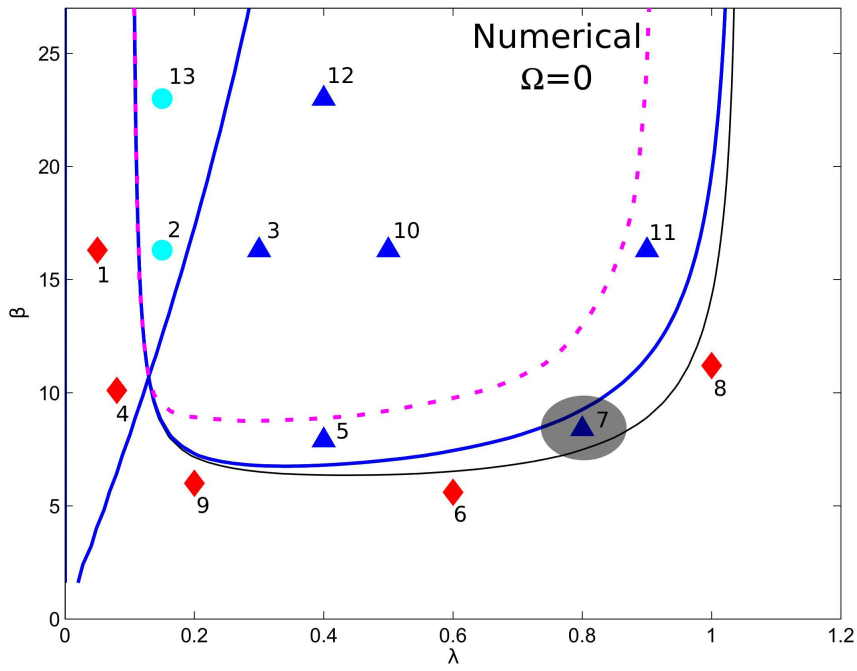

Figure 5.4: Comparison between theoretical and numerical marginal curves.

5.4 The role of the coefficient of lateral transport r

A series of benchmark simulations is here proposed to numerically investigate the effect of the transverse bed slope component on the bed-load transport direction (see also *Mosselman and Le* [2015]). This effect controls the balance between the gravitational effects acting in the transverse direction and the convective acceleration. Numerical simulations on alternate bars are sensitive to a change in the 'r' of *Ikeda* [1982] [*Defina*, 2003]: high values of r result in a smoothed topography while low values of r result in a steeper topography.

Benchmark simulations for the calibration of the coefficient of lateral transport r consist of a new series of simulations based on the same principle as the benchmark simulations of free bars in straight channels proposed by *Siviglia et al.* [2013], in which a refinement of the runs is added near

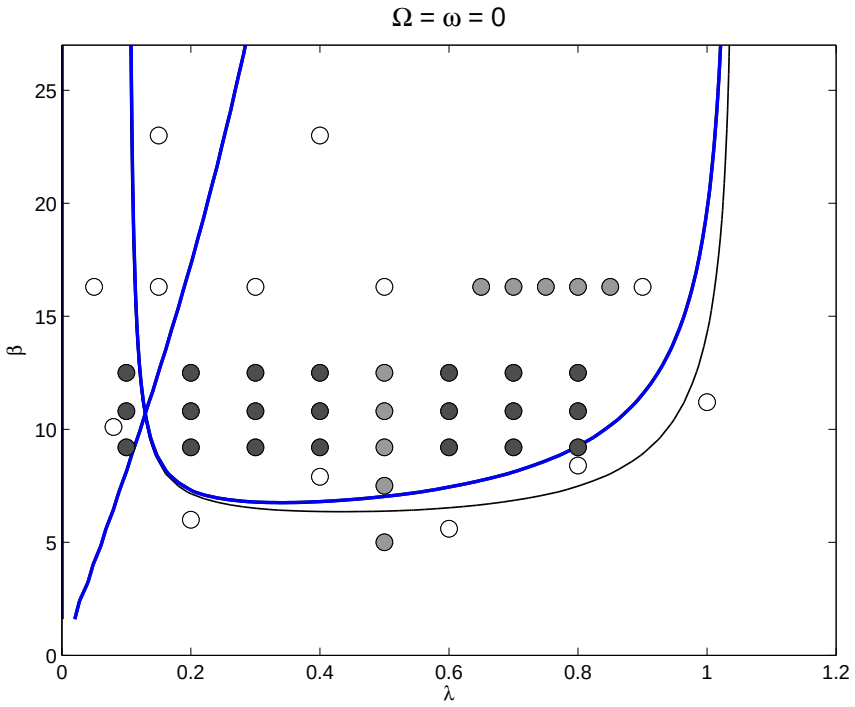

Figure 5.5: Set of benchmark simulations for the calibration of the effect of the transverse bed slope component on the bed-load transport direction, varying parameter r.

the plateau of the threshold growth rate curve ($\Omega = 0$) and for high values of λ, where the theoretical and numerical curves much differ.

In Fig. 5.5 three different sets of simulations are shown: a first set (empty circles) represents the basic procedure by *Siviglia et al.* [2013]; a second set (light grey circles) tests the vertical shift of the critical conditions ($\lambda = 0.5$, different values of β) and the unstable behavior at high values of lambda ($\beta = 16.3$, different values of λ); a third set (dark grey circles) is proposed to correctly estimate the shape of the plateau of the threshold $\Omega = 0$ condition (β respectively 9.2, 10.8 and 12.5, λ ranging in the interval 0.1-0.8).

Moreover, with respect to the runs presented in *Siviglia et al.* [2013] in which r is set as constant, here the value of the coefficient r ranges in the interval 0.0-0.9, with $\Delta r = 0.1$, so that each simulation of Fig. 5.5 is run

Table 5.2: Map of comparison between the theoretical behaviour of the 13 benchmark runs of *Siviglia et al.* [2013] with $r = 0.3$ and the numerical runs with different values of r.

	Coefficient r			
Run	0.0	0.1	0.2	0.3
1				
2				
3				
4				
5				
6				
7				
8				
9				
10				
11				
12				
13				

10 times. The lower limit $r = 0.0$ is tested to evaluate the capability of the numerical model to correctly predict the theoretical complete instability (and only the unstable region $\Omega > 0$ exists), the upper limit $r = 0.9$ is chosen as three times the 'standard' value of the parameter $r = 0.3$.

Each simulation is compared with the corresponding theoretical behaviour, so that a map of correspondence as the one presented in Tab. 5.1 is built.

In Tab. 5.2 the result-map of the benchmark simulations proposed by *Siviglia et al.* [2013] for different values of r is shown. The three different colours refer to different situations: green if the result of the run coincides with the theoretical behavior, yellow if the numerical behavior coincides with the threshold conditions ($\Omega = 0$), red if the theoretical and the

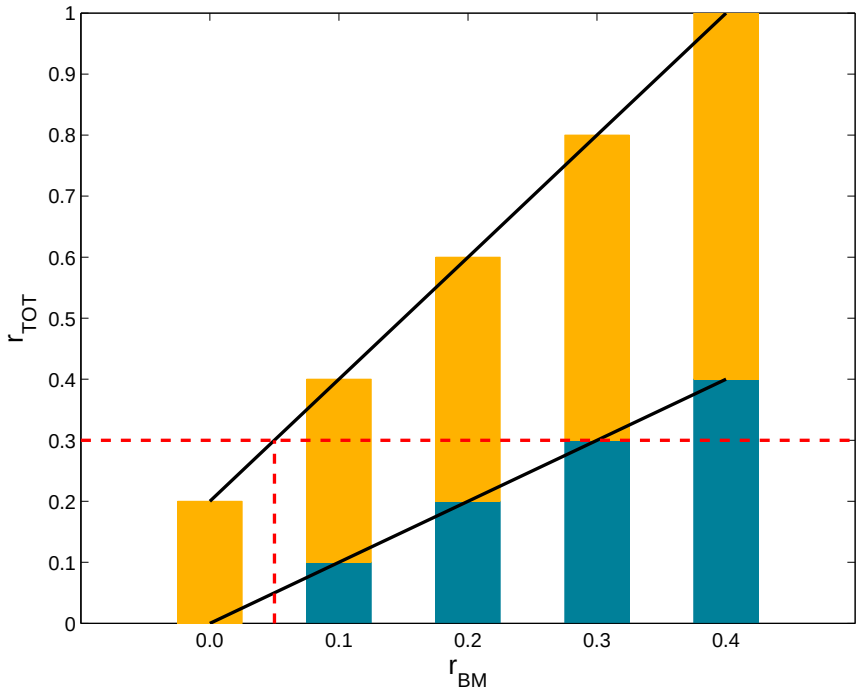

Figure 5.6: r_{BM} and r_{TOT}. The following values of the parameters have been employed: $\theta = 0.1$, $d_s = 0.061$, roughness formula: *Einstein* [1950], bed-load formula: *Wong and Parker* [2006].

numerical behavior differ. Run 11 presents always suppression, even with $r = 0.0$, run 9 only for the case of $r = 0.0$. Run 5 shows a not correct behaviour for $r = 0.2 - 0.3$, while for lower values of r the behaviour is correct or near the threshold. The condition $r = 0$ provides an indication of the residual diffusion of the numerical model. Some indications and hypotheses are described in 5.6. The residual numerical diffusion (r_N) is summed to the diffusion generated by the coefficient of lateral transport r (r_{BM}) to obtain a 'total' diffusion (r_{TOT}) that can be written as follow:

$$r_{TOT} = r_N + r_{BM} \tag{5.15}$$

In Fig. 5.6 the value of r_{TOT} of Eq. 5.15 is plotted as a function of the initial coefficient r_{BM} of Basement (blue part of the bars). The residual diffusion (yellow part of the bars) is estimated to be nearly 0.2

for $r_{BM} = 0.0$ up to nearly 0.6 for $r_{BM} = 0.4$, with a linear growth in between.

5.5 Numerical simulations of the Alpine Rhine river

Numerical simulations of the Alpine Rhine river have been performed in order to test the capability of the numerical model to correctly estimate the morphology of the field case and the main properties of the bed-forms thus obtained. Numerical results are compared with the field data presented in Ch. 3.

5.5.1 Numerical simulations

The chosen reach of the Alpine Rhine river is approximately 41 km long. The total length of the reach has been described using three distinct numerical domains, corresponding to the sectors presented in Ch. 3 and Ch. 4. The numerical domain of the entire reach covers the interval between the Landquart and Ill tributaries. The two unstructured ramps along the reach of Fig. 4.6 represent the control points for the division in sectors. Banks of the domains are digitized through the available cross sections of the Alpine Rhine. Some simplifications have been adopted for the choice of slope and sediment diameter: both are considered uniform per sector. Chosen values are the same as in Tab. 3.2. The initial bed configuration is flat and no artificial bed perturbations are added during the numerical simulations. For the computational domain, triangular meshes are adopted and discretised with 14884 (upstream), 23834 (central), 27216 (downstream) cells respectively. The total area of the three sectors is 4.234 km^2 and the total length is 41 km.

The *Meyer-Peter and Müller* [1948] formula is adopted for the bed-load transport, the Strickler formula is adopted for the roughness. With high values of the coefficient of lateral transport r bars tend not to grow in time. Moreover the analysis performed in Section 5.2.3 indicates a lower value of r in order to have a total equivalent $r = 0.3$. Thus calibration of parameter r is set 0.05.

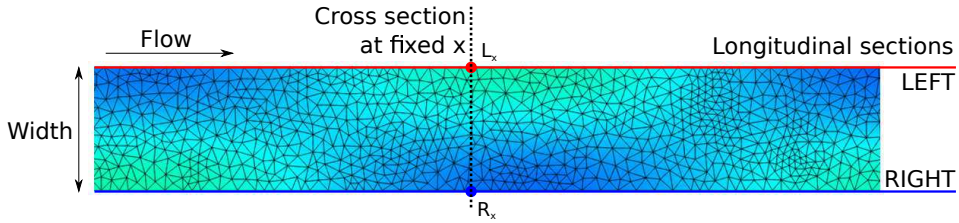

Figure 5.7: Example of the simplified computational mesh used in the free bar simulations presented in B in which the longitudinal section are superimposed.

Two different tests are performed. In the first test, constant discharges are used and two different constant discharges are chosen ($Q_{C2} = 780\,\mathrm{m^3 s^{-1}}$ and $Q_{C5} = 1000\,\mathrm{m^3 s^{-1}}$, where the subscript '$_C$' stands for constant). In the second test real hydrographs are used, and three different thresholds for minimum discharge are chosen: Q_{R2}, Q_{FT} and Q_{FW}, where the subscript '$_R$' stands for real.

At the beginning of the simulations, the mobile bed is assumed to be in equilibrium with the uniform flow conditions. The upstream boundary conditions are flow discharges and bed-load transport in equilibrium with the local upstream hydrodynamic conditions. Uniform flow depth is imposed downstream. The hydraulic conditions of all the simulations are sub-critical (Froude number $Fr < 1$).

5.5.1.1 Results for the constant discharge case

In the present section, results of the central sector are shown in terms of time evolution of the bed elevation of the left and right longitudinal sections, of the bar wavenumber and of the longitudinal position of bar tops in time.

In Fig. 5.8 and 5.9 the time evolution of the bed elevation of the right (blue lines) and left (red lines) longitudinal sections are shown. The uniform longitudinal slope is filtered out. In both figures, the width of the vertical grey strips represents the length of the bends, while the filling color is proportional with the radius of curvature (larger is lighter). Both the figures present the time evolution in the first 480 h of the run, with $\Delta t = 48\,\mathrm{h}$. Fig. 5.8 shows the case with constant discharge $Q_{C2} = 780\,\mathrm{m^3 s^{-1}}$, while Fig. 5.9 shows the case with $Q_{C5} = 1000\,\mathrm{m^3 s^{-1}}$.

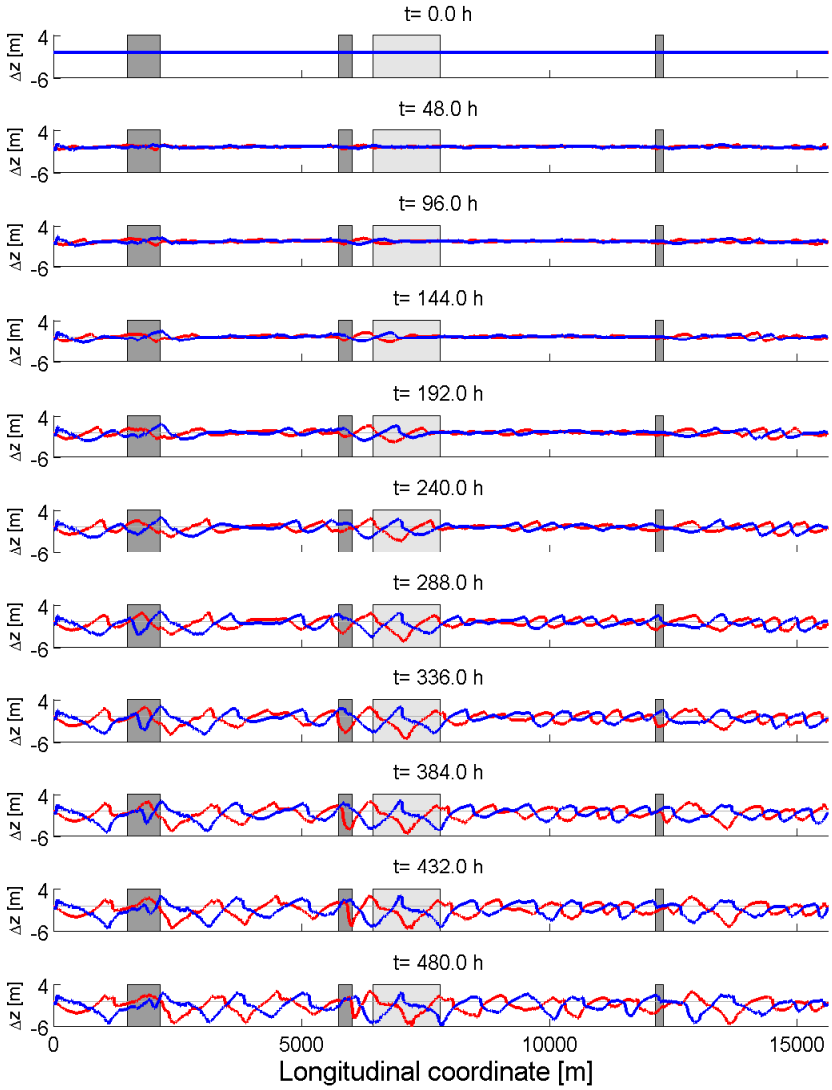

Figure 5.8: Case Q_{C2}, central sector. Time evolution of the longitudinal bed profiles of the left and right banks, respectively with red and blue lines. Longitudinal slope is filtered out. Vertical grey strips indicate Alpine Rhine bends.

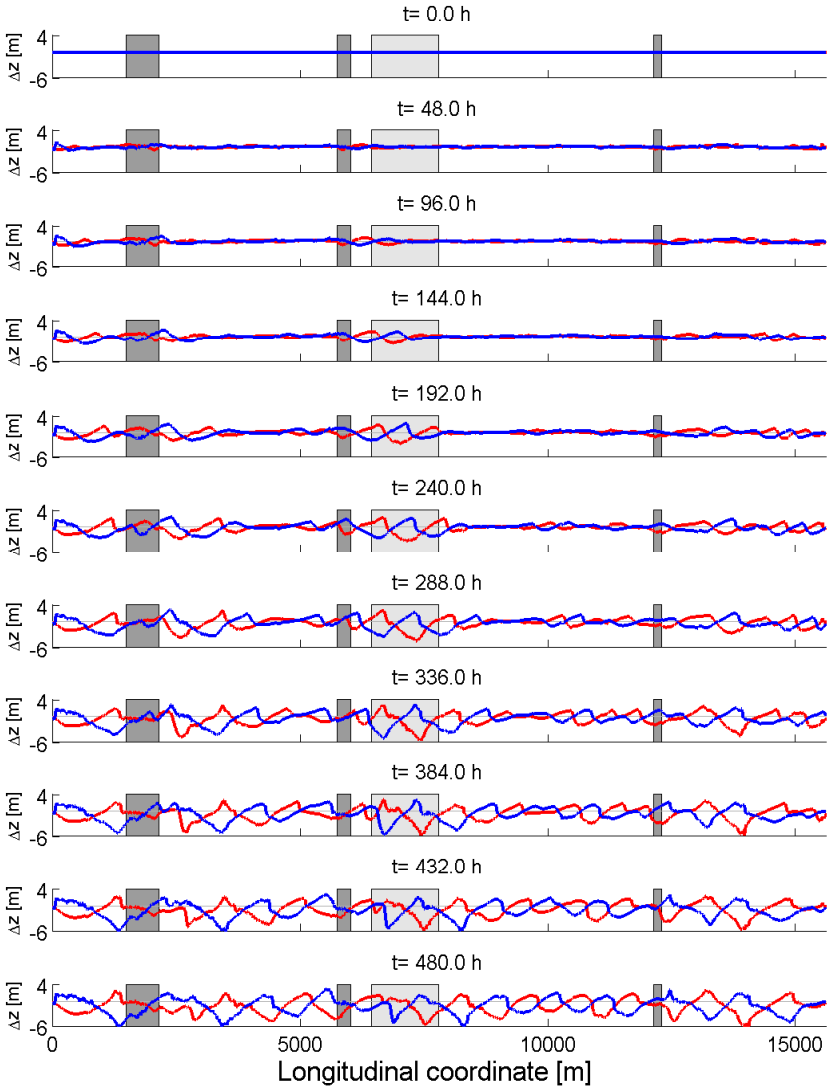

Figure 5.9: Case Q_{C5}, central sector. Time evolution of the longitudinal bed profiles of the left and right banks, respectively with red and blue lines. Longitudinal slope is filtered out. Vertical grey strips indicate Alpine Rhine bends.

Alternate bars form in the entire sector. In particular bars start to form in correspondence to the upstream boundary condition and to the three bends with the lower radius of curvature (sharp bend). Alternate bars start to grow in time and to migrate downstream. The appearance of alternate bars in the whole reach is visible since t=192 h, while the equilibrium amplitude near the bends is reached after nearly 336 h.

Fig. 5.10 shows the time evolution of the bar wavenumber in the two cases Q_{C2} and Q_{C5}. Starting the analysis of the bar wavenumber from t=196 h, in correspondence with the complete presence of alternate bars in the domain, the bar wavenumber initially presents values nearly 0.35-0.40, then decreases in time down to an equilibrium value of 0.25-0.30. The equilibrium value is reached nearly after 500 h for the Q_{C2} case and after 600 h for the Q_{C5} case.

Fig. 5.11 and Fig. 5.12 show the time evolution of the tops of alternate bars in correspondence to the left and right banks, indicated respectively with red and blue dots. As for previous figures, the width of the vertical grey strips represents the length of the bends, while the filling color is proportional with the radius of curvature (larger is lighter). Alternate bars in the domain present a relatively different behaviour in time. Up to 500 h alternate bars that form in the straight reaches migrate downstream, while alternate bars that form in the neighbourhood of the bends tend to migrate much less. Starting from 500 h alternate bars are non-migrating in the whole domain. A similar behavior is also shown in the preliminary run of super-resonant conditions in a straight channel with a permanent local narrowing presented in Appendix 1.

5.5.1.2 Results for the real hydrograph case

In the following section, results of the central sector are presented in terms of time evolution of the bar wavenumber. Real hydrographs are used as inflow boundary condition, with three different thresholds for the minimum discharge derived from the analysis presented in the previous chapters: fully wet discharge ($Q_{FW} = 230\,\mathrm{m^3 s^{-1}}$), fully transporting discharge ($Q_{FT} = 510\,\mathrm{m^3 s^{-1}}$) and discharge with a return period of 2 years ($Q_{R2} = 780\,\mathrm{m^3 s^{-1}}$).

The temporal evolution of the bar wavenumber is shown in Fig. 5.13 for

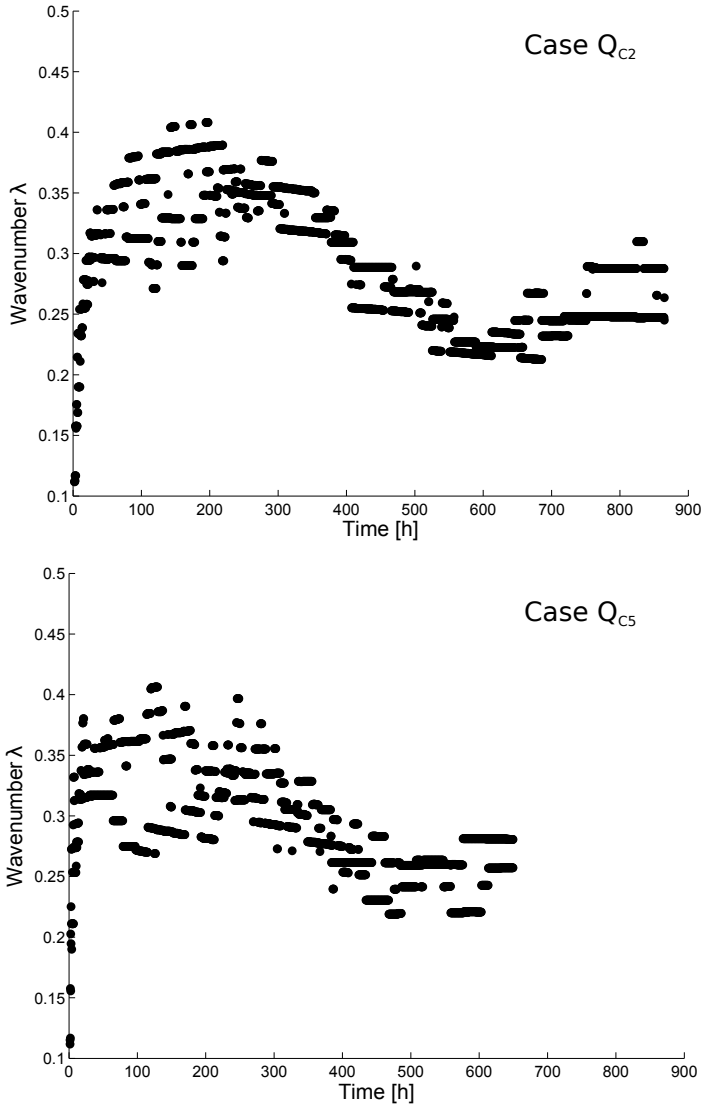

Figure 5.10: Cases Q_{C2} and Q_{C5}, central sector. Evolution in time of the bar wavenumber.

the three different cases. The choice of the minimum threshold influences the celerity of the wavenumber evolution: the lower case ($Q_{min} = Q_{R2}$) is the faster of the three analysed. In this case, the formation of alternate bars in the whole domain, defined as the time needed to have the

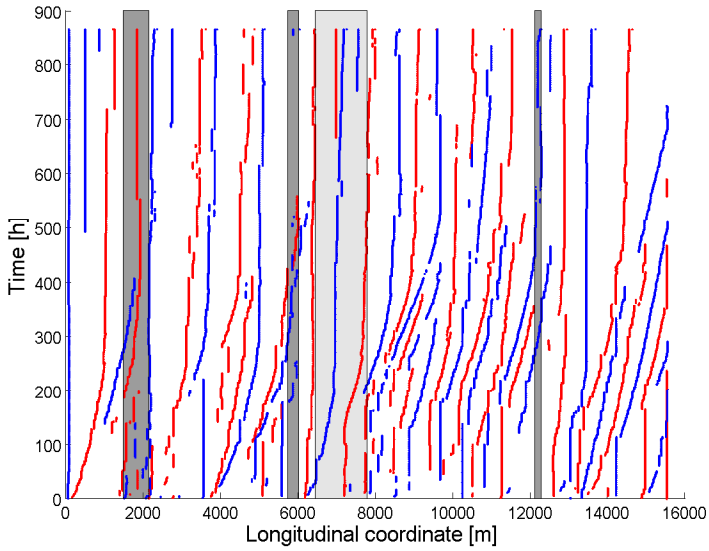

Figure 5.11: Case Q_{C2}, central sector. Evolution in time of the alternate bars tops along the left and right banks, respectively indicated with red and blue dots.

longitudinal coordinate fully covered with alternate bars, is completed in nearly 200 h, equivalent to the case of constant discharge $Q_{min} = Q_{C2}$. The range of variability of the wavenumber is greater in Q_{R2} with respect to Q_{C2} and to the cases in which Q_{min} is Q_{FT} and Q_{FW}. For the case Q_{FT} bar formation is completed in nearly 250 h, while the range of variability of bar wavelength at fixed time is clearly lower. The overall trend is comparable with the case Q_{R2}: after the maximum wavenumber a trend of bar elongation occurs up to the end of the run in which the bar wavenumber is nearly 0.25-0.30. The case in which $Q_{min} = Q_{FW}$ considers also the interval of discharges in which the river bed is not fully transporting sediments. This latter case shows a complete alternate bars formation at a longer time, nearly 800-900 h, and a range of wavenumber variability at fixed time comparable with the case of Q_{FT}. The the simulation has been stopped after 1200 h, in which the decreasing trend of the bar wavelength was beginning.

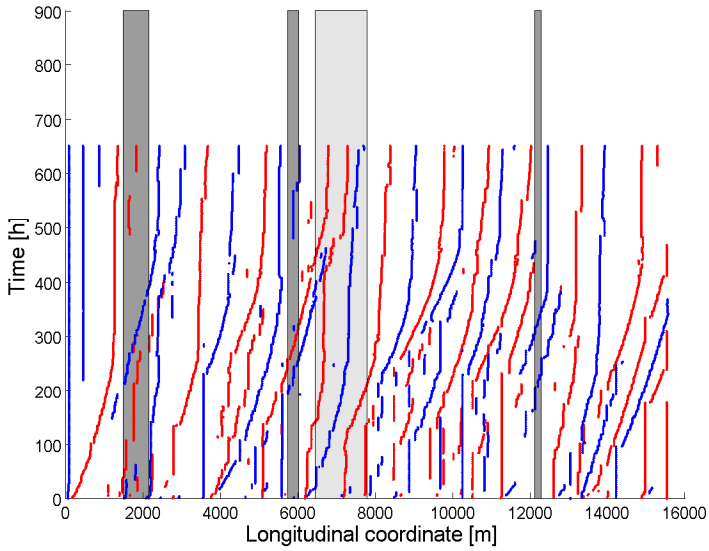

Figure 5.12: Case Q_{C5}, central sector. Evolution in time of the alternate bars tops along the left and right banks, respectively indicated with red and blue dots.

5.6 Discussion and conclusions

The capability of the morphological model Basement to correctly reproduce the theoretical growth rate and migration rate is tested through the application of a series of benchmark simulations proposed by *Siviglia et al.* [2013]. The numerical set-up includes a straight channel in which as initial condition bed elevation is sinusoidally perturbed. The solution of *Colombini et al.* [1987] is improved by adding the local effect of the longitudinal slope in the form suggested by *Van Rijn* [1989] and implemented in the numerical model. The main difference with the test cases of *Siviglia et al.* [2013] is run 7, originally in the unstable region of bar growth, now in the stable region of bar decay. Results of the benchmark tests show the correct behavior between theoretical analysis and numerical simulations for 11 cases out of the total 13. Cases 5 and 11, theoretically in the region of bar growth ($\Omega > 0$), show numerically bars that tend to be damped in time. This suggests a modification of the threshold conditions in the numerical model, due to a diffusive effect (see also *Mosselman and Le* [2015]).

The role of diffusion in the numerical model, excluding turbulence that is not considered in the analysis, is studied through an analysis of the correction on the direction of the bed-load transport due to the lateral slope. This effect, written in the form suggested by *Ikeda* [1982] and modified by *Van Rijn* [1993], counterbalances the effect due to gravity and is the main ingredient of the appearance of the stable region ($\Omega < 0$) in the analysis of *Colombini et al.* [1987]. A new benchmark test is presented with two main aims: (i) to evaluate the numerical threshold conditions in terms of growth rate and migration rate for a given value of r and (ii) to calibrate the coefficient r for a correct comparison with the theoretical threshold conditions. The set-up of the benchmark test allows to correctly calibrate the coefficient r and to evaluate the total effect due to diffusion. Changing the value of the coefficient r, the curve of total diffusion is presented for a case in which values of the parameters θ and d_s are fixed, showing an increasing total diffusion, as r is increased.

The second part of the chapter presents the numerical simulations of the Alpine Rhine reach. The first aim of the simulations is to evaluate the capability of the morphological model Basement to correctly reproduce (i) the continuous alternate bar morphology starting from flat bed conditions and (ii) the bar wavelength and migration of the field case. The second aim is to evaluate the role of different inflow conditions in the development of alternate bar properties. Each simulation is run with initial constant longitudinal slope, single grain size and with the real planimetric embankments and flat bed conditions. No artificial bed perturbation is added during the numerical simulations. This set-up allows to account for the presence along each sector of bends with different radius of curvature and different lengths that separate straight reaches with variable length. As for the case of sub- and super-resonant simulations, alternate bars start forming in correspondence to fixed planform constraints, in this case represented by bends. Moreover, the bar wavenumber λ tends to shorten in time, down to values of 0.25-0.30, between the theoretical migrating wavenumber $\lambda = 0.35$ and the non-migrating wavenumber $\lambda = 0.15$. Bar migration is also influenced by the presence of fixed bends, that tend to slow down the downstream migration (see e.g.*Zolezzi et al.* 2005 for an experimental example). The role of formative discharge is finally tested: both inflow

constant and variable tests are conducted. In the former, two different constant discharges, $Q_2 = 780\,\mathrm{m^3 s^{-1}}$ and $Q_5 = 1000\,\mathrm{m^3 s^{-1}}$, are considered. In the latter the real hydrograph is used with three different lower limits for the minimum discharge: fully wet discharge $Q_{FW} = 230\,\mathrm{m^3 s^{-1}}$, fully transporting discharge $Q_{FW} = 510\,\mathrm{m^3 s^{-1}}$ and 2 year time of return $Q_2 = 780\,\mathrm{m^3 s^{-1}}$. Similar behavior is shown in terms of temporal evolution of the bar wavenumber for the two cases of constant discharge, as well as the cases of the real hydrographs, in which the temporal scale of morphological evolution is much larger using the fully wet threshold.

Moreover, the trend of bar wavelength and migration of the application to the Alpine Rhine river is in good general agreement with the field data. Further improvements will include the presence of graded sediments and a comparison between cases in which the initial bed elevation is already composed by alternate bars, using the available topographical surveys taken in a time interval in which hydrological data are also present.

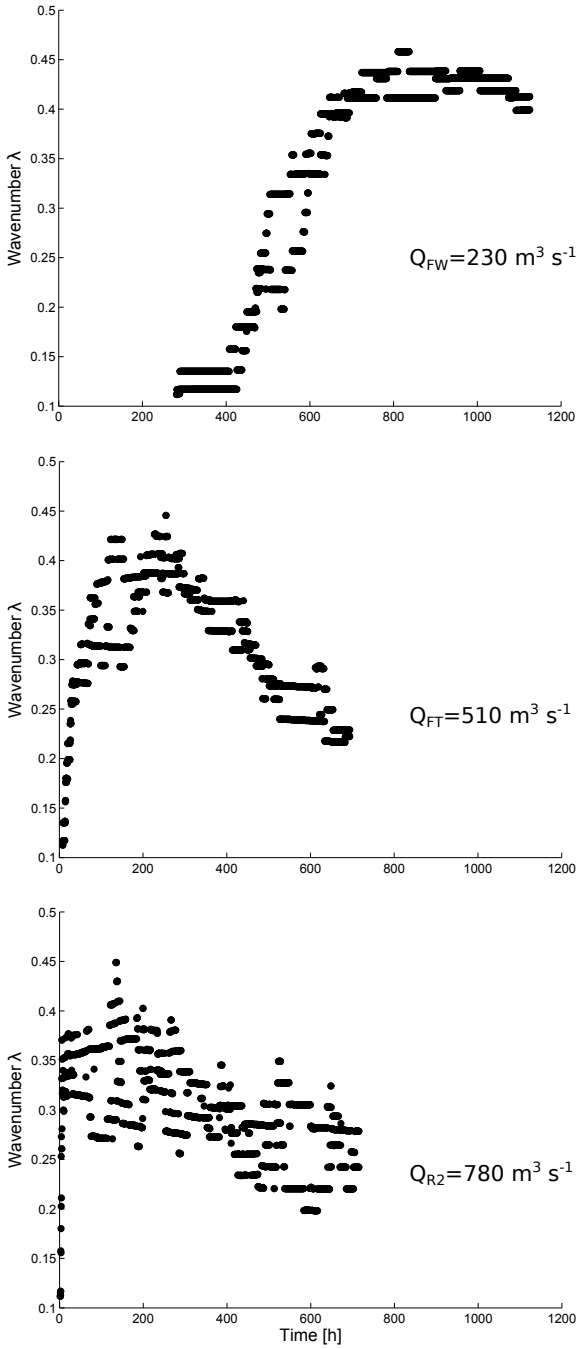

Figure 5.13: Cases Q_{FT}, Q_{FW} and Q_{R2}, central sector. Evolution in time of the bar wavenumber.

Chapter 6

Conclusions

In this final chapter, a summary of the most relevant conclusions of each previous chapter is given. Such a descriptive summary provides answers to the research questions formulated in the introductory chapter. Finally, a discussion of some open issues on further research and guidelines to follow is presented.

6.1 Summary of chapter conclusions

Long term morphodynamics of alternate bars in a straightened river. From the analysis of 30 years of freely available Landsat images, alternate-bar morphodynamics of a 42 km long reach of the Alpine Rhine river are described in terms of bar migration, bar wavelength, bar elongation and bar amplitude. This analysis resulted in one of the longest spatial and temporal field studies, with a resolution able to catch the effect of single flood events and the multi-decadal dynamics. Bars showed a spatially selective behavior, with long and non-migrating bars in the first sector of the reach and short and migrating bars in the second and third sectors. Bar elongation is absent in the upstream sector, while in the central and downstream sectors bars tend to shortening in long straight reaches. The role of bends in limiting the bar migration and in increasing the bar wavelength is also shown. The temporally long dataset allowed the investigation of bar migration as a function of the discharge, showing that bars migrate faster for intermediate floods. The dataset provides also useful information to

assess the applicability of analytical bar theories, so far mainly tested against flume experiments, and following recent attempts in French and Dutch streams.

Application of analytical bar theories to a real case. The hypotheses of the analytical theories are described and compared with the field configuration of the Alpine Rhine river. An approach is proposed to apply bar theories accounting for the difference in setting with the field case. Different roughness formulas, bed-load formulas and values of the gravitational transport coefficient are evaluated to investigate the sensitivity of these parameters. Critical and resonant conditions are shown as a function of the wavenumber λ and the width ratio β, showing their variability in the range of discharge between the fully transporting conditions and the discharge with 100 years time of return. The effect of unsteady discharge is compared with the theoretical findings of *Tubino* [1991]. The hydrograph is characterized referring to critical and resonant conditions. The wavelength of migrating bars is in good agreement with linear theory of free bars of *Colombini et al.* [1987], while the bar migration is overestimated. The wavelength of non-migrating bars is double with respect to that of migrating bars, but slightly lower with respect to that predicted for resonant conditions [*Colombini et al.*, 1987]. Estimation of the transverse bar mode as proposed by *Crosato and Mosselman* [2009] is tested with good agreement in two cases: in the reach with bars (between Landquart and Ill) and in the reach without bars (between Ill and Lake of Constance). The theoretical damping length derived from *Zolezzi and Seminara* [2001] showed also good agreement with the field data. The markedly different behaviour between the upstream sector with long non-migrating bars and the central and downstream sectors with short migrating bars is discussed in terms of differences in channel geometry, in properties of free bars and in properties of forced bars. In particular for the latter, the analysis showed that a good parameter to differentiate between the two different behaviors is the amount of time during which the discharge is high enough to determine sub resonant conditions, with respect to the amount of time for which there are super-resonant conditions. Such differences depend on the flood hydrograph, but also on the channel geometry and sediment properties. Comparing theories and observations suggests that theoretical

outcomes may represent the boundaries of the actual, intermediate behavior of bars, which likely reflects non-linear interactions, flow unsteadiness, sediment size heterogeneity and finite length of straight reaches, which are not retained in linear theories. The comparison demonstrates the value of theories for the interpretation of field observations: for instance, the difference in the migration-wavelength relation may suggest the long, steady bars to be forced by local planform discontinuities and the short migrating bars to result from a free instability of the riverbed. Flow unsteadiness seems to have a minor role here while grain size sorting might affect bar wavelength and migration. Despite the simplifying theoretical assumptions, the work shows that bar theories not only provide information on bar geometry and dynamics, but they can also help interpret the physical processes at the basis of their occurrence, i.e., set a suitable framework to differentiate between free migrating or forced steady bars.

Numerical modelling the long term evolution of alternate bars. The morphodynamic model Basement is tested to reproduce several morphological processes: (i) the formation and development of free migrating alternate bars in straight reaches; (ii) the formation and development of forced non-migrating alternate bars in straight reaches with fixed planform constraints. Moreover, (iii) the benchmark simulations of free bars as proposed by *Siviglia et al.* [2013] are used to test the capability of the software to correctly reproduce the theoretical growth rate and migration of free alternate bars; (iv) a new benchmark simulation is proposed and tested for the calibration of the coefficient r of lateral transport; (v) the long term evolution of the sectors of the Alpine Rhine reach using different inflow discharges is analysed. The model (i) correctly reproduced the formation of free migrating alternate bars and also (ii) correctly reproduced the sub- and super-resonant conditions of non-migrating bars forced by a fixed planform perturbation. Basement passed 11 of the 13 benchmark tests for free migrating bars proposed by *Siviglia et al.* [2013] and the analysis of the two failures is discussed in terms of numerical diffusion. A new benchmark set of simulation is developed and performed in order to correctly calibrate the coefficient r of lateral transport to obtain an equivalent diffusive effect for the comparison with the critical conditions resulting from the linear stability analysis of *Colombini et al.* [1987].

Moreover, (v) a series of simulations of the three different sectors of the Alpine Rhine reach showed the role of the discharge in the formation of alternate bars with different wavelengths, migration and heights. Finally, the numerical runs show that the migration rate of alternate bars in correspondence to constraints like bends is lower than the migration rate in straight reaches.

6.2 Open issues

There are four main aspects to be taken into account in order to deepen the work:

In the considered period the role of the vegetation is negligible since almost none of the alternate bars is covered by vegetation due to the typical snow-melting hydrological regime that maintains the top of the bars submerged in the vegetative period. Since 2010, the hydrological regime, influenced also by the presence of hydropower plants upstream the confluence of the Landquart river, is much more irregular and one single bar, located in the upstream sector, partially started to become vegetated. Since the whole upstream sector is composed by non-migrating bars, further attention can be focused on the causes and on the consequences of the vegetation in the morphodynamics of alternate bars of the whole reach.

Morphological model Basement and the existing theoretical framework can be used to help evaluating the morphological evolution of different widening configurations, introducing a 2D support to design projects. A test case can be the Alpine Rhine river, downstream the confluence of the Ill river [*Mähr et al.*, 2014]. In this reach, presently with no bars, an ongoing restoration project (www.rhesi.ch) aims to widen the existent embankments to lower the flood risk of the Rhine valley and to increase the morphological complexity of the river.

The diffusive effect of the correction of lateral slope on the bed-load transport direction focused the attention on a possible way to determine the role of diffusion in a morphological model. To better

describe this effect, a broader range of simulations has to be run, with a range of values of the width ratio, of the relative roughness and of the average size of the cells of the numerical mesh.

The effect of the choice of different hydro-morphological closures (e.g. roughness formula, bed-load formula, coefficient r of lateral slope) influence the threshold conditions of bar formation and bar migration. The effect of local longitudinal slope treated in Chapter 5 is an example that shows how linear solutions can be improved in order (i) to achieve a more detailed understanding of the conditions of bar formation and (ii) to provide a theoretical basis for a benchmark calibration of morphological models.

Bibliography

Adami, L., W. Bertoldi, and G. Zolezzi (2014), Morphodynamics of alternate bars in the Alpine Rhine river: Methods for the applicability of mathematical models using felds observations, *Proceedings of the International Conference on Fluvial Hydraulics, RIVER FLOW 2014*, pp. 1213–1220.

Adami, L., W. Bertoldi, and G. Zolezzi (2016), Multi-decadal dynamics of alternate bars in the Alpine Rhine river., *Submitted to Water Resources and Research*, pp. n/a–n/a.

Ashida, K., and M. Michiue (1972), Study on hydraulic resistance and bedload transport rate in alluvial streams. transactions, in *Proceedings of the Japan Society of Civil Engineers*, vol. 206, pp. 59–64.

Ashmore, P., W. Bertoldi, and J. Tobias Gardner (2011), Active width of gravel-bed braided rivers, *Earth Surface Processes and Landforms*, *36*(11), 1510–1521, doi:10.1002/esp.2182.

Bärenbold, F., B. Crouzy, and P. Perona (2016), Stability analysis of ecomorphodynamic equations, *Water Resources Research*, doi:10.1002/2015WR017492.

Bernini, A., V. Caleffi, and A. Valiani (2009), *Numerical Modelling of Alternate Bars in Shallow Channels*, pp. 153–175, Blackwell Publishing Ltd., doi:10.1002/9781444304374.ch7.

Bertoldi, W., A. Siviglia, S. Tettamanti, M. Toffolon, D. Vetsch, and S. Francalanci (2014), Modeling vegetation controls on fluvial morphological trajectories, *Geophysical Research Letters*, *41*(20), 7167–7175, doi:10.1002/2014GL061666.

Bijker, E. (1971), Longshore transport computation., *Journal of Waterways, Harbours and Coastal Engineering Division.*, *97*, 415–435.

Blondeaux, P., and G. Seminara (1985), A unified bar-bend theory of river meanders, *J. Fluid Mech.*, *157*, 449–470.

Brinson, M., and A. MalvÃąrez (2002), Temperate freshwater wetlands: Types, status, and threats, *Environmental Conservation*, *29*(2), 115–133, doi:10.1017/S0376892902000085.

Brown, T. (1991), Historical change of large alluvial rivers: Western europe edited by G. E. Petts, H. Moller and A. L. Roux, J. Wiley, Chichester, 1989. no. of pages: 355, *Earth Surface Processes and Landforms*, *16*(2), 181–182, doi:10.1002/esp.3290160210.

Callander, R. A. (1969), Instability and river channels, *Journal of Fluid Mechanics*, *36*, 465–480.

Camenen, B., A. Bayram, and M. Larson (2006), Equivalent roughness height for plane bed under steady flow, *Journal of Hydraulic Engineering*, *132*(11), 1146–1158, doi:10.1061/(ASCE)0733-9429(2006)132:11(1146).

Camporeale, C., E. Perucca, L. Ridolfi, and A. Gurnell (2013), Modeling the interactions between river morphodynamics and riparian vegetation, *Reviews of Geophysics*, *51*(3), 379–414, doi:10.1002/rog.20014.

Chang, H. (1985), Formation of alternate bars, *Journal of Hydraulic Engineering*, *111*(11), 1412–1420, doi:10.1061/(ASCE)0733-9429(1985)111:11(1412).

Church, M., and R. I. Ferguson (2015), Morphodynamics: Rivers beyond steady state, *Water Resources Research*, *51*(4), 1883–1897, doi:10.1002/2014WR016862.

Church, M., and S. P. Rice (2009), Form and growth of bars in a wandering gravel-bed river, *Earth Surface Processes and Landforms*, *34*(10), 1422–1432, doi:10.1002/esp.1831.

Claude, N., S. Rodrigues, V. Bustillo, J.-G. BrÃľhÃľret, P. Tassi, and P. JugÃľ (2014), Interactions between flow structure and morphodynamic of bars in a channel expansion/contraction, Loire River, France, *Water Resources Research*, *50*(4), 2850–2873, doi:10.1002/2013WR015182.

Colombini, M., and A. Stocchino (2012), Three-dimensional river bed forms, *Journal of Fluid Mechanics*, *695*, 63–80, doi:10.1017/jfm.2011.556.

Colombini, M., G. Seminara, and M. Tubino (1987), Finite-amplitude alternate bars, *Journal of Fluid Mechanics*, *181*, 213–232, doi:10.1017/S0022112087002064.

Constantine, J. A., T. Dunne, J. Ahmed, C. Legleiter, and E. D. Lazarus (2014), Sediment supply as a driver of river meandering and floodplain evolution in the Amazon Basin, *Nature Geoscience*, *7*(12), 899–903, doi:10.1038/ngeo2282.

Crosato, A., and E. Mosselman (2009), Simple physics-based predictor for the number of river bars and the transition between meandering and braiding, *Water Resources Research*, *45*(3), n/a–n/a, doi:10.1029/2008WR007242, w03424.

Crosato, A., E. Mosselman, F. Beidmariam Desta, and W. S. J. Uijttewaal (2011), Experimental and numerical evidence for intrinsic nonmigrating bars in alluvial channels, *Water Resources Research*, *47*(3), n/a–n/a, doi:10.1029/2010WR009714.

Crosato, A., F. B. Desta, J. Cornelisse, F. Schuurman, and W. S. J. Uijttewaal (2012), Experimental and numerical findings on the long-term evolution of migrating alternate bars in alluvial channels, *Water Resources Research*, *48*(6), doi:10.1029/2011WR011320.

Curran, J., and W. Hession (2013), Vegetative impacts on hydraulics and sediment processes across the fluvial system, *Journal of Hydrology*, *505*, 364–376, doi:10.1016/j.jhydrol.2013.10.013, cited By 3.

Defina, A. (2003), Numerical experiments on bar growth, *Water Resources Research*, *39*(4), n/a–n/a, doi:10.1029/2002WR001455.

Defina, A., and S. Lanzoni (2002), Simulazione numerica dell'evoluzione di barre alternate (in italian)., in *28 Convegno di Idraulica e Costruzioni Idrauliche*, vol. 3, pp. 103–110, Potenza, Italy.

DurÃš, G., A. Crosato, and P. Tassi (2015), Numerical study on river bar response to spatial variations of channel width, *Advances in Water Resources*, pp. –, doi:http://dx.doi.org/10.1016/j.advwatres.2015.10.003.

Eekhout, J. P. C., A. J. F. Hoitink, and E. Mosselman (2013), Field experiment on alternate bar development in a straight sand-bed stream, *Water Resources Research*, *49*(12), 8357–8369, doi:10.1002/2013WR014259.

Einstein, H. (1950), *The Bed-load Function for Sediment Transportation in Open Channel Flows*, Technical bulletin (United States. Dept. of Agriculture), U.S. Department of Agriculture.

Engels, H. (1914), *Handbuch des Wasserbaues: fur das Studium und die Praxis*, Engelmann.

Engelund, F. (1981), The motion of sediment particles on an inclined bed., *Project 53*, Tech. Univ. Denmark, ISVA.

Engelund, F., and E. Hansen (1967), A monograph on sediment transport in alluvial streams., *Project*, Tech. Univ. Denmark, ISVA.

Federici, B., and M. Colombini (2002), Barre alternate di ampiezza finita: analisi spaziale (in italian)., in *28 Convegno di Idraulica e Costruzioni Idrauliche*, vol. 3, pp. 95–102, Potenza, Italy.

Federici, B., and G. Seminara (2006), Effect of suspended load on sandbar instability, *Water Resources Research*, *42*(7), n/a–n/a, doi: 10.1029/2005WR004399, w07407.

Ferguson, R. I., D. J. Bloomer, and M. Church (2011), Evolution of an advancing gravel front: observations from Vedder Canal, British Columbia, *Earth Surface Processes and Landforms*, *36*(9), 1172–1182, doi:10.1002/esp.2142.

Fujita, Y., and Y. Muramoto (1982), Experimental studies on stream channel processes in alluvial rivers, *DPRI Bullettin*, *32*(288), 46–96.

Fujita, Y., and Y. Muramoto (1985), Studies on the process of development of alternate bars, *DPRI Bullettin*, *35*(314), 46–96.

Garcia, M., and Y. Niño (1993), Dynamics of sediment bars in straight and meandering channels: experiments on the resonance phenomenon., *Journal of Hydraulic Engineering*, *31:6*, 739–761.

Gomez, B., and M. Church (1989), An assessment of bed load sediment transport formulae for gravel bed rivers, *Water Resources Research*, *25*(6), 1161–1186, doi:10.1029/WR025i006p01161.

Gurnell, A. (2014), Plants as river system engineers, *Earth Surface Processes and Landforms*, *39*(1), 4–25, doi:10.1002/esp.3397.

Gurnell, A. (2015), Plants as river system engineers: further comments, *Earth Surface Processes and Landforms*, *40*(1), 135–137, doi:10.1002/esp.3671.

Gurnell, A., W. Bertoldi, and D. Corenblit (2012), Changing river channels: The roles of hydrological processes, plants and pioneer fluvial landforms in humid temperate, mixed load, gravel bed rivers, *Earth-Science Reviews*, *111*(1-2), 129–141, doi:10.1016/j.earscirev.2011.11.005.

Hansen, E. (1967), On the formation of meanders as a stability problem., *Tech. Rep. Prog. Rep. 13*, Tech. Univ. of Denmark, Lyngby, Denmark, coastal Eng. Lab.

Hasegawa, K. (1981), Bank-erosion discharge based on a non-equilibrium theory, in *Proceedings of the Japan Society of Civil Engineers*, vol. 316, pp. 37–50.

Hauer, C. (2015), Review of hydro-morphological management criteria on a river basin scale for preservation and restoration of freshwater pearl mussel habitats, *Limnologica*, *50*, 40–53, doi:10.1016/j.limno.2014.11.002.

Henshaw, A. J., A. M. Gurnell, W. Bertoldi, and N. A. Drake (2013), An assessment of the degree to which Landsat TM data can support the assessment of fluvial dynamics, as revealed by changes in vegetation extent and channel position, along a large river, *Geomorphology*, *202*(0), 74 – 85, doi:http://dx.doi.org/10.1016/j.geomorph.2013.01.011.

Huang, H. Q. (2010), Reformulation of the bed load equation of Meyer-Peter and Müller in light of the linearity theory for alluvial channel flow, *Water Resources Research*, *46*(9), n/a–n/a, doi:10.1029/2009WR008974, w09533.

Hunziker, Zarn, and Partners (2001), Morphologie und Geschiebehaushalt Alpenrhein (Morphology and sediment budget of Alpine Rhine), *Project A-108*, Internationale Regierungskommission Alpenrhein (International Government Commission of Alpine Rhine).

Hunziker, R., and M. Jäggi (2002), Grain sorting processes, *Journal of Hydraulic Engineering*, *128*(12), 1060–1068, doi:10.1061/(ASCE)0733-9429(2002)128:12(1060).

Ikeda, S. (1982), Lateral bed load transport on side slopes, *Journal of the Hydraulic Division, ASCE*, *108*(HY11), 1369–1373.

Ikeda, S. (1984), Prediction of alternate bar wavelength and height, *Journal of Hydraulic Engineering*, *110*(4), 371–386, doi:10.1061/(ASCE)0733-9429(1984)110:4(371).

Jaballah, M., B. Camenen, L. PÃľnard, and A. Paquier (2015), Alternate bar development in an alpine river following engineering works, *Advances in Water Resources*, *81*(available on-line), 103–113, doi:http://dx.doi.org/10.1016/j.advwatres.2015.03.003.

Jäggi, M. (1983), Alternierende kiesbanke (Alternate bars), Ph.D. thesis, Swiss Federal Institute of Technology Zürich Laboratory of Hydraulics, Hydrology and Glaciology, Switzerland.

Jäggi, M. (1984), Formation and effects of alternate bars, *Journal of Hydraulic Engineering*, *110*(2), 142–156, doi:10.1061/(ASCE)0733-9429(1984)110:2(142).

Kinoshita, R. (1961), Investigation of channel deformation in ishikari river., *Tech. report*, Bureau of Resources, Department of Science and Technology, Japan.

Kinoshita, R., and H. Miwa (1967), River channel formation which prevents downstream translation of transverse bar (in japanese), *Shinsabo*, *94*, 12–17.

Knaapen, M., S. Hulscher, H. D. Vriend, and A. V. Harten (2001), Height and wavelength of alternate bars in rivers: modelling vs. laboratory experiments, *Journal of Hydraulic Research*, *39*(2), 147–153, doi:10.1080/00221680109499815.

Kovacs, A., and G. Parker (1994), A new vectorial bedload formulation and its application to the time evolution of straight river channels, *Journal of Fluid Mechanics*, *267*, 153–183, doi:10.1017/S002211209400114X.

Lane, S., and K. Richards (1997), Linking river channel form and process: Time, space and causality revisited, *Earth Surface Processes and Landforms*, *22*(3), 249–260, doi:10.1002/(SICI)1096-9837(199703)22:3<249::AID-ESP752>3.0.CO;2-7.

Lane, S., K. Bradbrook, K. Richards, P. Biron, and A. Roy (1999), The application of computational fluid dynamics to natural river channels: Three-dimensional versus two-dimensional approaches, *Geomorphology*, *29*(1-2), 1–20, doi:10.1016/S0169-555X(99)00003-3.

Lanzoni, S. (2000a), Experiments on bar formation in a straight flume: 1. uniform sediment, *Water Resources Research*, *36*(11), 3337–3349, doi:10.1029/2000WR900160.

Lanzoni, S. (2000b), Experiments on bar formation in a straight flume: 2. graded sediment, *Water Resources Research*, *36*(11), 3351–3363, doi:10.1029/2000WR900161.

Lanzoni, S., and M. Tubino (1999), Grain sorting and bar instability, *Journal of Fluid Mechanics*, *393*, 149–174, doi:10.1017/S0022112099005583.

Lesser, G., J. Roelvink, J. van Kester, and G. Stelling (2004), Development and validation of a three-dimensional morphological model, *Coastal Engineering*, *51*(8âĂŞ9), 883 – 915, doi:http://dx.doi.org/10.1016/j.coastaleng.2004.07.014, coastal Morphodynamic Modeling.

Lewin, J. (1976), Initiation of bedforms and meanders in coarse grained sediment, *Bulletin of the Geological Society of America*, *87*(2), 281–285.

Lotter, G. (1933), Soobrazheniia k gidravlicheskomu raschetu rusel s razlichnoi sherokhovatos tiiu stenok (Considerations on hydraulic design of channels with different roughness of walls), *Izvestiia Vsesoiuznogo N uachnoIssledovatelâĂŹskogo Instituta Gidrotekhniki (All-Union Scientific Research Institute of Hydraulic Engineering)*, *9*, 238–241.

Lytle, D., and N. Poff (2004), Adaptation to natural flow regimes, *Trends in Ecology and Evolution*, *19*(2), 94–100, doi:10.1016/j.tree.2003.10.002.

Mähr, M., D. Schenk, M. Schatzmann, and A. Meng (2014), Alpine rhine project (section river ill-lake constance), in *Proceedings of the International Conference on Fluvial Hydraulics, RIVER FLOW 2014*, pp. 39–47.

Meyer-Peter, E., and R. Müller (1948), Formulas for bed-load transport, in *Proc. 2nd Meeting IAHR*, pp. 39–64, Stockholm, Sweden.

Mosselman, E., and T. Le (2015), Five common mistakes in fluvial morphodynamic modeling, *Advances in Water Resources*, doi:10.1016/j.advwatres.2015.07.025.

Mosselman, E., M. Tubino, and G. Zolezzi (2006), The overdeepening theory in river morphodynamics: Two decades of shifting interpretations, in *Proceedings of the International Conference on Fluvial Hydraulics - River Flow 2006*, vol. 2, pp. 1175–1181.

Nagayama, S., M. Harada, and Y. Kayaba (2015), Classification of morphology and habitat in streams and rivers: Application to river management, *Ecology and Civil Engineering*, *18*(1), 19–33.

Nakamura, F., Y. Kawaguchi, D. Nakano, and H. Yamada (2007), 19 ecological responses to anthropogenic alterations of gravel-bed rivers in japan, from floodplain river segments to the microhabitat scale: a review, in *Gravel-Bed Rivers VI: From Process Understanding to River Restoration*, *Developments in Earth Surface Processes*, vol. 11, edited by H. P. Helmut Habersack and M. Rinaldi, pp. 501 – 523, Elsevier, doi:http://dx.doi.org/10.1016/S0928-2025(07)11141-X.

Nicholas, A. P. (2013), Modelling the continuum of river channel patterns, *Earth Surface Processes and Landforms*, *38*(10), 1187–1196, doi:10.1002/esp.3431.

Nienhuis, P., and R. Leuven (2001), River restoration and flood protection: controversy or synergism?, *Hydrobiologia*, *444*(1), 85–99, doi:10.1023/A:1017509410951.

Olesen, K. W. (1983), Alternate bars in and meandering of alluvial rivers, *Communications on Hydrology. Report*, pp. 7–83.

Olesen, K. W. (1984), Discussion of "steady flow in alluvial channels" by Gerd Holtorff (august, 1982), *Journal of Waterway, Port, Coastal, and Ocean Engineering*, *110*(1), 99–100, doi:10.1061/(ASCE)0733-950X(1984)110:1(99).

Palmer, M., D. Lettenmaier, N. Poff, S. Postel, B. Richter, and R. Warner (2009), Climate change and river ecosystems: Protection and adaptation options, *Environmental Management*, *44*(6), 1053–1068, doi:10.1007/s00267-009-9329-1.

Parker, G. (1975), Sediment inertia as cause of river antidunes, *Journal of Hydraulic Division*, *101*, 536–558.

Parker, G. (1984), Discussion of âĂIJlateral bed load transport on side slopesâĂİ by syunsuke ikeda (november, 1982)., *Journal of Hydraulic Engineering*, *110*, 197–199, doi:10.1061/(ASCE)0733-9429(1984).

Parker, G. (1990), Surface-based bedload transport relation for gravel rivers, *Journal of Hydraulic Research*, *28*(4), 417–436, doi:10.1080/00221689009499058.

Parker, G., and H. Johannesson (1989), *Observations on Several Recent Theories of Resonance and Overdeepening in Meandering Channels*, pp. 379–415, American Geophysical Union, doi:10.1029/WM012p0379.

Parker, G., P. R. Wilcock, C. Paola, W. E. Dietrich, and J. Pitlick (2007), Physical basis for quasi-universal relations describing bankfull hydraulic geometry of single-thread gravel bed rivers, *Journal of Geophysical Research: Earth Surface*, *112*(F4), doi:10.1029/2006JF000549.

QGIS Development Team (2009), *QGIS Geographic Information System*, Open Source Geospatial Foundation.

Recking, A. (2006), An experimental study of grain sorting effects on bedload, Ph.D. thesis, Institute National Des Sciences Appliquees De Lyon.

Reid, D., and M. Church (2015), Geomorphic and ecological consequences of riprap placement in river systems, *Journal of the American Water Resources Association*, *51*(4), 1043–1059, doi:10.1111/jawr.12279, cited By 0.

Repetto, R., and M. Tubino (2001), Topographic expressions of bars in channels with variable width, *Physics and Chemistry of the Earth, Part B: Hydrology, Oceans and Atmosphere*, *26*(1), 71–76, doi:10.1016/S1464-1909(01)85017-6, cited By 4.

Repetto, R., M. Tubino, and C. Paola (2002), Planimetric instability of channels with variable width, *Journal of Fluid Mechanics*, *457*, 79–109, doi:10.1017/S0022112001007595.

Ribberink, J. S. (1998), Bed-load transport for steady flows and unsteady oscillatory flows, *Coastal Engineering*, *34*(1âĂŞ2), 59 – 82, doi:http://dx.doi.org/10.1016/S0378-3839(98)00013-1.

Rodrigues, S., N. Claude, P. Juge, and J.-G. Breheret (2012), An opportunity to connect the morphodynamics of alternate bars with their sedimentary products, *Earth Surface Processes and Landforms*, *37*(2), 240–248, doi:10.1002/esp.2255.

Rodrigues, S., E. Mosselman, N. Claude, C. L. Wintenberger, and P. Juge (2015), Alternate bars in a sandy gravel bed river: generation, migration and interactions with superimposed dunes, *Earth Surface Processes and Landforms*, *40*(5), 610–628, doi:10.1002/esp.3657.

Rousseau, Y. Y., P. M. Biron, and M. J. Van de Wiel (2016), Sensitivity of simulated flow fields and bathymetries in meandering channels to the choice of a morphodynamic model, *Earth Surface Processes and Landforms*, pp. n/a–n/a, doi:10.1002/esp.3885.

Schielen, R., A. Doelman, and H. de Swart (1993), On the nonlinear dynamics of free bars in straight channels, *Journal of Fluid Mechanics*, *252*, 325–356.

Schumm, S., and H. Khan (1972), Experimental study of channel patterns, *Bulletin of the Geological Society of America*, *83*(6), 1755–1770, doi:10.1130/0016-7606(1972)83[1755:ESOCP]2.0.CO;2.

Schuurman, F., W. Marra, and M. Kleinhans (2013), Physics-based modeling of large braided sand-bed rivers: Bar pattern formation, dynamics, and sensitivity, *Journal of Geophysical Research: Earth Surface*, *118*(4), 2509–2527, doi:10.1002/2013JF002896.

Sekine, M., and G. Parker (1992), Bed-load transport on transverse slope. i, *Journal of Hydraulic Engineering*, *118*(4), 513–535, doi:10.1061/(ASCE)0733-9429(1992)118:4(513).

Seminara, G., and M. Tubino (1992), Weakly nonlinear theory of regular meanders, *Journal of Fluid Mechanics*, *244*, 257–288, doi:10.1017/S0022112092003069.

Shields, M. (1936), Anwendung der aehnlichkeitsmechanik und der turbulenzforschung auf die geschiebebewegung, Ph.D. thesis, Technical University Berlin.

Siviglia, A., and A. Crosato (2016), Numerical modelling of river morphodynamics: Latest developments and remaining challenges, *Advances in Water Resources*, pp. –, doi:http://dx.doi.org/10.1016/j.advwatres.2016.01.005.

Siviglia, A., G. Stecca, D. Vanzo, G. Zolezzi, E. F. Toro, and M. Tubino (2013), Numerical modelling of two-dimensional morphodynamics with applications to river bars and bifurcations, *Advances in Water Resources*, *52*(0), 243 – 260, doi:http://dx.doi.org/10.1016/j.advwatres.2012.11.010.

Smart, G. (1984), Sediment transport formula for steep channels, *Journal of Hydraulic Engineering*, *110*(3), 267–276, doi:10.1061/(ASCE)0733-9429(1984)110:3(267).

Solari, L., M. Van Oorschot, B. Belletti, D. Hendriks, M. Rinaldi, and A. Vargas-Luna (2016), Advances on modelling riparian vegetationâĂŤhydromorphology interactions, *River Research and Applications*, *32*(2), 164–178, doi:10.1002/rra.2910.

Soulsby, R. (1997), *Dynamics of Marine Sands: A Manual for Practical Applications*, Telford.

Stevens, M. (1989), Width of straight alluvial channels, *Journal of Hydraulic Engineering*, *115*(3), 309–326, doi:10.1061/(ASCE)0733-9429(1989)115:3(309).

Struiksma, N., and A. Crosato (1989), *Analysis of a 2-D Bed Topography Model for Rivers*, pp. 153–180, American Geophysical Union, doi:10.1029/WM012p0153.

Struiksma, N., K. Olesen, C. Flokstra, and H. De Vriend (1985), Bed deformation in curved alluvial channels, *Journal of Hydraulic Research*, *23*(1), 57–59, doi:10.1080/00221688509499377.

Sukegawa, N. (1972), Criterion for alternate bar formation in experimental flumes., *Proc Jap Soc Civ Eng*, *207*, 47–50.

Surian, N., and M. Rinaldi (2003), Morphological response to river engineering and management in alluvial channels in Italy, *Geomorphology*, *50*(4), 307 – 326, doi:http://dx.doi.org/10.1016/S0169-555X(02)00219-2.

Takebayashi, H., and S. Egashira (2001), Instability of developed alternate bar on non-uniform sediment bed., in *Proceedings of the 29th International Association of Hydraulic Engineering and Research*, edited by E. W. Z. Y. et al., Tsinghua University Press, Beijing.

Talmon, A. (1992), Bed topography of river bends with suspended sediment transport, *Tech. rep.*, Delft Hydraulics Laboratory, Delft, Netherlands.

Talmon, A., N. Struiksma, and M. V. Mierlo (1995), Laboratory measurements of the direction of sediment transport on transverse alluvial-bed slopes, *Journal of Hydraulic Research*, *33*(4), 495–517, doi:10.1080/00221689509498657.

Talukdar, S., B. Kumar, and S. Dutta (2012), Predictive capability of bedload equations using flume data, *Journal of Hydrology and Hydromechanics*, *60*(1), 45–56.

Tockner, K., and J. Stanford (2002), Riverine flood plains: Present state and future trends, *Environmental Conservation*, *29*(3), 308–330, doi:10.1017/S037689290200022X.

Tubino, M. (1991), Growth of alternate bars in unsteady flow, *Water Resources Research*, *27*(1), 37–52, doi:10.1029/90WR01699.

Tubino, M., and G. Seminara (1990), Free-forced interactions in developing meanders and suppression of free bars, *Journal of Fluid Mechanics*, *214*, 131–159, cited By 57.

Tubino, M., R. Repetto, and G. Zolezzi (1999), Free bars in rivers, *Journal of Hydraulic Research*, *37*(6), 759–775, doi:10.1080/00221689909498510.

Van Der Meer, C., E. Mosselman, C. Sloff, B. Jagers, G. Zolezzi, and M. Tubino (2011), Numerical simulations of upstream and downstream overdeepening, in *RCEM 2011: Proceedings of the 7th IAHR Symposium of River, Coastal and Estuarine Morphodynamics, Beijing, China, 6-8 September 2011*, pp. 1721–1729, Tsingshua University Press.

van der Wegen, M., and J. A. Roelvink (2008), Long-term morphodynamic evolution of a tidal embayment using a two-dimensional, process-based model, *Journal of Geophysical Research: Oceans*, *113*(C3), n/a–n/a, doi:10.1029/2006JC003983, c03016.

Van Rijn, L. (1984), Sediment transport, Part i: Bed load transport, *Journal of Hydraulic Engineering*, *110*, 1431–1456.

Van Rijn, L. (1989), Handbook: sediment transport by current and waves, *Tech. rep.*, Delft Hydraulics Laboratory, Delft, Netherlands.

Van Rijn, L. (1993), *Principles of sediment transport in rivers, estuaries and coastal seas*, Aqua Publications.

Vetsch, D., A. Siviglia, D. Ehrbar, M. Facchini, M. Gerber, S. Kammerer, S. Peter, D. Vanzo, L. Vonwiller, C. Volz, D. Farshi, R. Mueller, P. Rousselot, R. Veprek, and R. Faeh (2016a), Basement - basic simulation environment for computation of environmental flow and natural hazard simulation, https://www.basement.ethz.ch/, version 2.6.

Vetsch, D., A. Siviglia, D. Ehrbar, M. Facchini, M. Gerber, S. Kammerer, S. Peter, D. Vanzo, L. Vonwiller, C. Volz, D. Farshi, R. Mueller, P. Rousselot, R. Veprek, and R. Faeh (2016b), *System manuals of BASEMENT, Version 2.6 - Basic Simulation Environment for Computation of Environmental Flow and Natural Hazard Simulation*, Laboratory of Hydraulics, Glaciology and Hydrology (VAW). ETH Zurich., http://www.basement.ethz.ch.

Vriend, H. J. D. (1981), Steady ïňĆow in shallow channel bends, *Tech. rep.*, Delft University of Technology, Delft, The Netherlands.

Welford, M. R. (1994), A field test of Tubino's (1991) model of alternate bar formation, *Earth Surface Processes and Landforms*, *19*(4), 287–297, doi:10.1002/esp.3290190402.

Werth, K. (2014), *Geschichte der Etsch zwischen Meran und San Michele Flussregulierung, Trockenlegung der MÃűser, Hochwasserschutz.*, Athesia.

Whipple, K., and G. Tucker (2002), Implications of sediment-flux-dependent river incision models for landscape evolution, *Journal of Geophysical Research: Solid Earth*, *107*(2), 3–1–3–20.

Wong, M., and G. Parker (2006), Reanalysis and correction of bed-load relation of Meyer-Peter and Müller using their own database, *Journal of Hydraulic Engineering*, *132*, 1159–1168.

Wu, W., S. S. Wang, and Y. Jia (2000), Nonuniform sediment transport in alluvial rivers, *Journal of Hydraulic Research*, *38*(6), 427–434, doi: 10.1080/00221680009498296.

Yalin, M. S. (1963), An expression for bed-load transportation, *Journal of Hydraulic Engineering*, *89*(3), 221–250.

Zeller, J. (1967), Flussmorphologische studie zum mäanderproblem / meandering channels in switzerland, *Project 74*, ETH Zürich.

Zen, S., G. Zolezzi, and M. Tubino (2014), A theoretical analysis of river bars stability under changing channel width, *Advances in Geosciences*, *39*, 27–35, doi:10.5194/adgeo-39-27-2014.

Zolezzi, G., and G. Seminara (2001), Downstream and upstream influence in river meandering. part 2. planimetric development, *Journal of Fluid Mechanics*, *438*, 183–211, doi:10.1017/S002211200100427X.

Zolezzi, G., M. Guala, D. Termini, and G. Seminara (2005), Experimental observations of upstream overdeepening, *Journal of Fluid Mechanics*, *531*, 191–219.

Zolezzi, G., W. Bertoldi, and M. Tubino (2012), *Morphodynamics of Bars in Gravel-Bed Rivers: Bridging Analytical Models and Field Observations*, pp. 69–89, John Wiley & Sons, Ltd, doi:10.1002/9781119952497.ch6.

Appendices

Appendix A

Sensitivity of theoretical results to roughness and bed-load closure relations and the effect of transverse bed slopes on sediment transport direction

The qualitative outcomes of linear stability analysis for free bars, and also of the theories of forced bars, shows some dependance on the choice of:

- roughness formula;
- bed-load formula;
- coefficient r, quantifying the role of local transverse bed slope $\partial\eta/\partial n$ on the direction of sediment transport.

The above items represent empirical closures of the governing mathematical problem. Nevertheless, changing roughness and bed-load formula, as well as the empirical value of the r coefficient, the resonant and critical parameter change. Here the comparison between different formulations of roughness, bed-load and and the effect of r in the linear solution for free bars instability is analysed.

It must be remarked that the quantitative differences that emerge in the present Appendix are thought not to affect significantly the key outcomes of the analysis presented in Chapter 4 of the thesis. The sensitivity to the roughness, bed-load formulae and to the empirical r coefficient become quantitatively relevant when aiming to compare analytical theories with numerical simulations of bar morphodynamics in the same case, or when benchmarking the latter with the former.

A.1 Roughness formula

Two different bed roughness formula are compared in order to evaluate their role in determining different critical and resonantthreshold conditions in terms of critical and resonant values of the parameter β. Bed roughness are here written in terms of the Chezy roughness, and in dimensionless form. The first one, reported also in 2.9, refers to *Einstein* [1950]:

$$C = 6 + 2.5 \ln\left(\frac{D}{2.5 d_s}\right), \tag{A.1}$$

while the second is from *Van Rijn* [1984]:

$$C = \frac{18}{\sqrt{g}\ln 10} \ln\left(\frac{12D}{3d_s}\right), \tag{A.2}$$

where the d_{90} is put equal to d_{50} and expressed as $d_s = d_{50}/D_0$.

In Figure A.1 an example of the comparison of the two different formulation is reported using the same dimensional parameters (Q, d_{50}, s, W). In terms of growth rate Ω, the *Van Rijn* [1984] formula sets a larger critical parameter β_C and considers a broader unstable region for large wavenumbers. In terms of migration rate ω, the threshold curve $\omega = 0$ is less steep, so that the resonant value is smaller respect to the case of *Einstein* [1950] formula. The sub-resonant region $\beta_C < \beta < \beta_R$ is then smaller.

A.2 Bed-load formula

Bed-load transport formulae are based on the idea that a relations between hydraulic conditions, bed surface layer and sediment transport rate exists

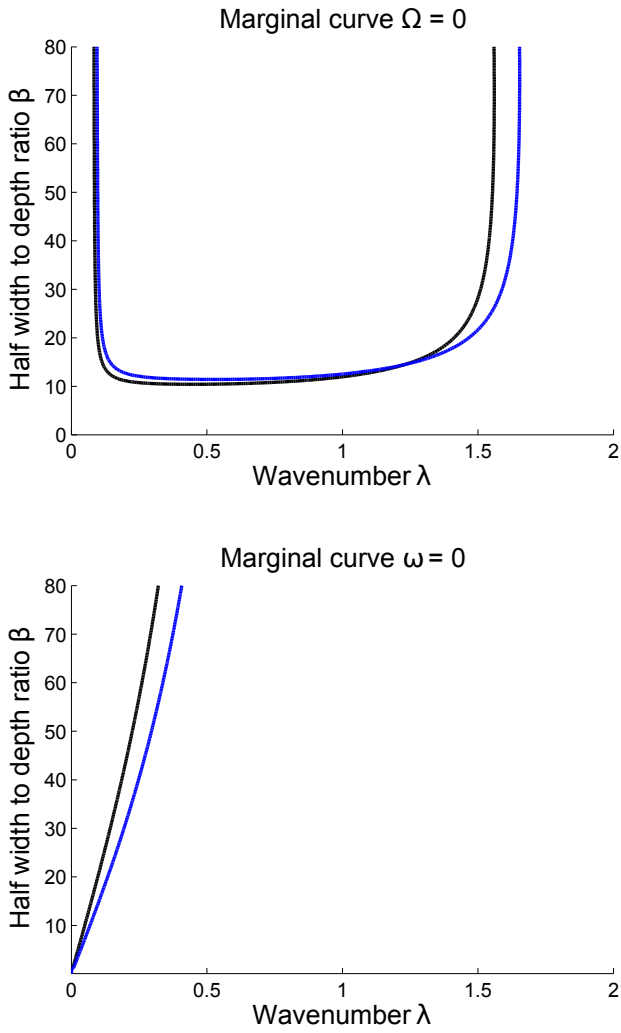

Figure A.1: Comparison between neutral curves $\Omega = 0$ and $\omega = 0$ using different roughness formula. The blue lines refer to the case of *Einstein* [1950] formula, while blue lines refer to *Van Rijn* [1984] formula ($Q = 2000\,\mathrm{m^3 s^{-1}}$, $d_{50} = 0.04\,\mathrm{m}$, $s = 0.002\,\mathrm{m/m}$, $W = 100\,\mathrm{m}$).

(see e.g. *Gomez and Church*, 1989). Different approaches have been used to obtain the existing bed-load transport formulae (e.g. *Talukdar et al.*, 2012), based on shear stress (e.g. *Shields*, 1936; *Ribberink*, 1998; *Wong*

and Parker, 2006, energy slope, discharge, regression (e.g. *Yalin*, 1963; *Engelund and Hansen*, 1967; *Camenen et al.*, 2006, equal mobility and probability approach(e.g. *Einstein*, 1950). Extensive analysis has been performed by *Recking* [2006], but the choice of the 'correct' bed-load formula remains an open issue.

In this comparison, 7 different bed-load formulae have been tested.

1. *Meyer-Peter and Müller*, 1948:

$$\Phi = 8\left(\theta - \theta_{cr}\right)^{\frac{3}{2}}, \tag{A.3}$$

   where $\theta_c = 0.047$.

2. *Wong and Parker*, 2006:

$$\Phi = 3.97\left(\theta - \theta_{cr}\right)^{\frac{3}{2}}, \tag{A.4}$$

   where $\theta_c = 0.0495$.

3. *Hunziker and Jäggi*, 2002:

$$\Phi = 5\left(\theta - \theta_{cr}\right)^{\frac{3}{2}}, \tag{A.5}$$

   where $\theta_c = 0.05$.

4. *Huang*, 2010:

$$\Phi = 6\left(\theta - \theta_{cr}\right)^{\frac{5}{3}}, \tag{A.6}$$

   where $\theta_c = 0.047$.

5. *Engelund and Hansen*, 1967:

$$\Phi = 0.05\frac{\theta^{\frac{5}{2}}}{C_0}, \tag{A.7}$$

6. *Van Rijn*, 1984:

$$\Phi = 0.053\frac{tsp^{2.1}}{d_*^{0.3}}, \tag{A.8}$$

   where $tsp = \left(u*^2 - u*_c^2\right)/u*_c^2$ represent the transport stage parameter, $d_* = d_{50}\left(\Delta g/k_{visc}^2\right)^{1/3}$ is the dimensionless particle diameter with the kinematic viscosity $k_{visc} = 1 \times 10^{-6}\,\mathrm{m^2 s^{-1}}$.

7. *Parker*, 1990:

$$\begin{cases} \phi = \phi_0\, 5474 \left(1 - \frac{0.853}{\theta'}\right)^{\frac{9}{2}}, & \text{if } \theta' > 1.588 \\ \phi = \phi_0\, e^{14.2(\theta'-1)-9.28(\theta'-1)^2} & \text{if } 1 < \theta' \leq 1.588, \\ \phi = \phi_0\, \theta'^{14.2} & \text{if } 1 \geq \theta'. \end{cases} \tag{A.9}$$

where $\phi_0 = 0.00218\,\theta^{3/2}$ and $\theta' = \theta/\theta_c$, with $\theta_c = 0.0386$.

In Figure A.2 and Figure A.3 marginal curves $\Omega = 0$ and $\omega = 0$ are shown in two different cases. The former is the case of parameter near the conditions of incipient motion ($\theta \approx \theta_c$), while the latter shows the case of fully established bed-load transport ($\theta \gg \theta_c$). The critical conditions for the case of Figure A.2 is defined in a broader interval of β compared with the case of Figure A.3, with β_C ranging in the interval $5 \div 20$ in the first case and $9 \div 12$ in the second case. The two formulations that present the greater difference respect the average $\Omega = 0$ curve are *Engelund and Hansen* [1967] and *Van Rijn* [1984]. *Engelund and Hansen* [1967] is also the only one that differs respect to the average behaviour in terms of marginal $\omega = 0$ for the case of incipient motion.

A.3 Coefficient of lateral transport r

The analysis on the deviation of average particle trajectories respect to the direction of the average shear stress under the effect of gravity performed by *Engelund* [1981] (see also e.g. *Parker*, 1984, *Blondeaux and Seminara*, 1985) introduce a correction in which the coefficient r is present in the term:

$$-\frac{r}{\beta\sqrt{\theta}}\frac{\partial \eta}{\partial n} \tag{A.10}$$

of Equation 2.11. This lateral deviation of the direction of the particle trajectories is the fundamental process that introduce the instability ($\Omega > 0$) in the solution, otherwise unconditionally stable. Very few studies (e.g. *Hasegawa*, 1981; *Ikeda*, 1982; *Olesen*, 1983; *Parker*, 1984; *Sekine and Parker*, 1992) account for the role of this term, even if it is broadly used.

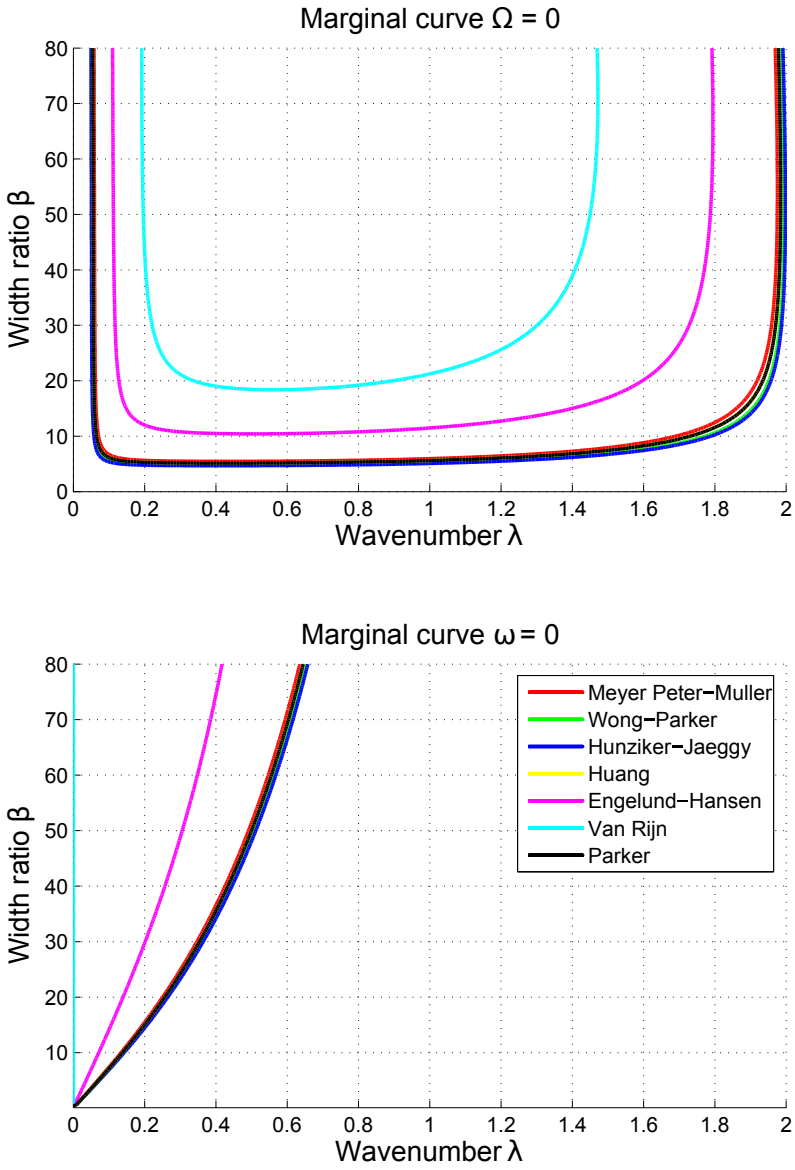

Figure A.2: Comparison between neutral curves $\Omega = 0$ and $\omega = 0$ using different bed-load formulae, near the condition of incipient motion. ($Q = 500\,\mathrm{m^3 s^{-1}}$, $d_{50} = 0.04\,\mathrm{m}$, $s = 0.002\,\mathrm{m/m}$, $W = 100\,\mathrm{m}$).

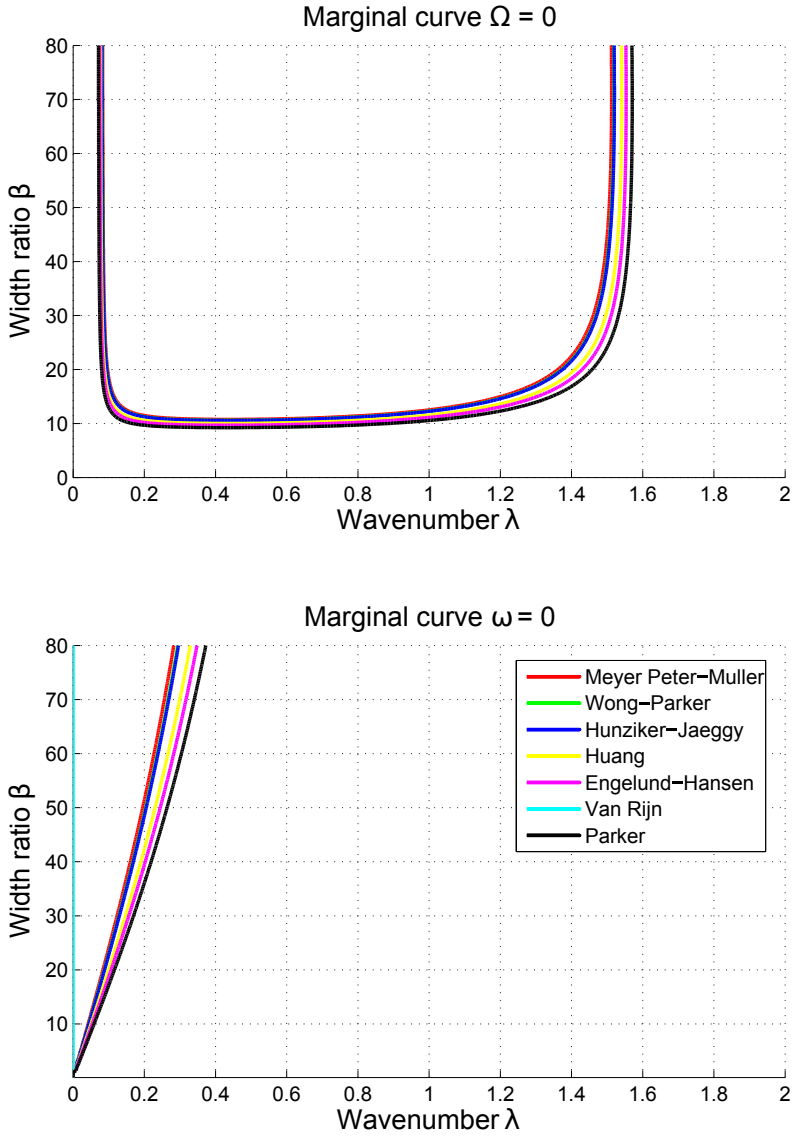

Figure A.3: Comparison between neutral curves $\Omega = 0$ and $\omega = 0$ using different bed-load formulae, far from the condition of incipient motion. ($Q = 2000\,\mathrm{m^3 s^{-1}}$, $d_{50} = 0.04\,\mathrm{m}$, $s = 0.002\,\mathrm{m/m}$, $W = 100\,\mathrm{m}$).

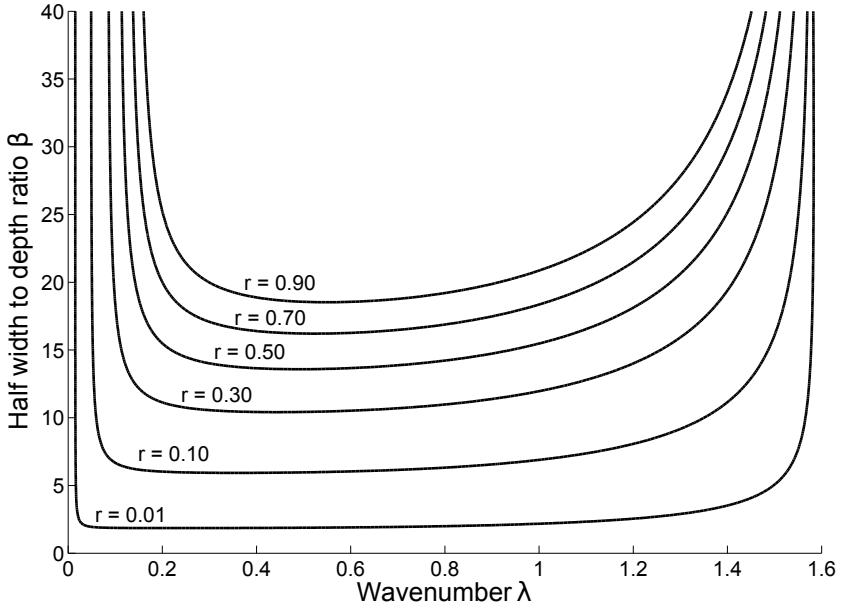

Figure A.4: Different neutral curves $\Omega = 0$ at fixed values of β, θ, d_s, for different values of the r coefficient of lateral transport in the range $r = 0.01 \div 0.9$. Lowering r corresponds to increase the unstable region ($\Omega > 0$ in which bars develop in time.

Appendix B

Numerical simulations of alternate bar formation with the morphological model Basement

This chapter is partly based on the monograph: "Alternate bars in straight domains", Laboratory of Hydraulics, Hydrology and Glaciology of the Swiss Federal Institute of Technology of Zurich.

B.1 Introduction

Aims of this Chapter are to test the capability of the numerical model Basement (i) to simulate conditions of formation and development of alternate bars in a straight channels and (ii) to correctly reproduce theoretical critical [*Colombini et al.*, 1987] and resonant [*Seminara and Tubino*, 1992; *Zolezzi and Seminara*, 2001] conditions.

B.2 Numerical model: Basement

Main characteristics of Basement model are compared with two 2D numerical models used to evaluate alternate bar formation and development: GIAMT2D [*Siviglia et al.*, 2013] and DELFT3D [*Lesser et al.*, 2004; *van der Wegen and Roelvink*, 2008]

Table B.1: Summary of the characteristics of numerical model BASEMENT v2.5.1, in comparison with GIAMT2D and with Delft3D.

CHARACTERISTICS	*GIAMT2D*	*Delft3D*	*Basement*
Mesh	unstructured, triangular	structured, curvilinear	structured curvilinear, unstructured triangular
Numerics	Finite volume, fully-coupled, explicit scheme	Finite difference, semi-coupled, semi-implicit scheme	Finite volume, uncoupled or semi-coupled, explicit scheme
Lateral bank erosion	not available	based upon stream line curvature	available since v2.6
Spiral flow parametrization	not available	based upon stream line curvature	not available
Sediment transport	Meyer-Peter and Muller-like formulas, *Parker* [1990]	Meyer-Peter and Muller-like formulas, *Engelund and Hansen* [1967], *Bijker* [1971], *Ashida and Michiue* [1972], *Van Rijn* [1984], *Soulsby* [1997]	Meyer-Peter and Muller-like formulas, *Smart* [1984], *Van Rijn* [1984], *Wu et al.* [2000]
Transverse bed slope effects on direction of bed-load	*Ikeda* [1982]	*Ikeda* [1982] modified by *Van Rijn* [1993]	*Ikeda* [1982] modified by *Van Rijn* [1993]
2D-Roughness formulation	Manning	Manning, Chezy, White-Colebrook	Manning, Chezy, Darcy-Weisbach
2D-Turbulence	Not available	Constant value assigned, turbulence closure models and algebraic forms	Algebraic forms
Wetting and drying	Capable	Capable	Capable

B.3 Test runs of free and forced bars in straight domains

A first set of simulations are completed to test the capability of the numerical model Basement to correctly simulate the formation and development of alternate bars in a straight domain. These runs focus on the formation of free migrating bars and forced steady bars testing different boundary conditions and different set-ups of the numerical model. This section partially follows the existing analysis of *Defina* [2003]; *Bernini et al.* [2009]; *Siviglia et al.* [2013] to allow a direct comparison of the methods.

B.3.1 Setting up the numerical simulations

Numerical model is tested to correctly reproduce free and forced bar generation and bar growth under the conditions proposed by *Siviglia et al.* [2013]. For the case of free bars, some further preliminary analysis are performed in order to evaluate the role of boundary conditions in the formation of alternate bars (e.g. *Defina* 2003). Next section starts form this last case.

B.3.2 Free bars

A first set of simulation is run to evaluate to which extent Basement can reproduce free bars in a straight domain. The geometrical and hydraulic properties of the runs follow the hypothesis of the analytical solution of *Colombini et al.* [1987]: rectangular cross section, constant inflow discharge and solid discharge and uniform grain size.

Two different scenarios are described, starting from the rectangular cross section in which the bed elevation can be left free to evolve in time or randomly perturbed. Cases tested are in super-critical conditions ($\beta > \beta_C$) and in sub-resonant conditions ($\beta < \beta_R$)

Case A flat bed condition, constant inflow discharge;

Case B flat bed condition, constant inflow discharge, random perturbation of the bottom in time;

Table B.2: Summary of the parameters used in the Cases A and B.

Description	*Value*	*Unit*
Mesh Length	6000	m
Mesh Width	60	m
N. of cells	31117	–
Discharge	500	m^3/s
Slope	0.011	m/m
Mean diameter	40	mm
Total run time	259200	s
Initial bed	Flat	
θ	0.266	–
d_s	0.025	–
β	18.80	–
β_C	8.75	–
β_R	33.2	–

Cases A and B are tested with the same initial and boundary conditions, reported in Table B.2. The difference between the cases is due to the random perturbation of the bottom artificially added to the numerical solution of Case B. Total run time of Cases A and B is 72 h.

Results are presented in terms of variation of the bed elevation in time respect the initial bed elevation conditions:

$$\Delta z = z\,(t) - z\,(t = 0) \tag{B.1}$$

Case A

Fig. B.1 shows a zoom of the computational straight domain in which left and right longitudinal sections have been plotted in Fig. B.2. L_x and R_x represent the two points of intersection of a cross section at fixed longitudinal coordinate x and the two longitudinal sections plotted in time in Fig. B.3. In Fig. B.2 the time evolution of the longitudinal bed profiles in the first 16 h is shown in correspondence of the right and left banks

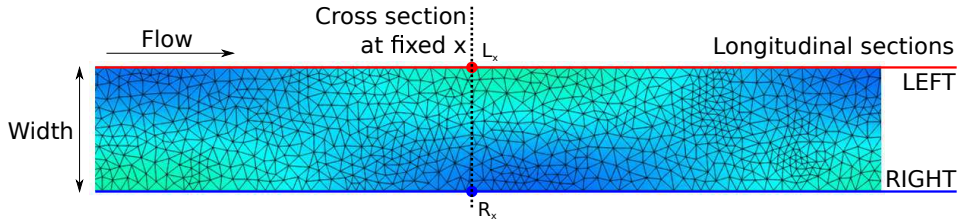

Figure B.1: Example of computational mesh used in the free bar simulations. The mesh grid is superimposed to the value of the bed elevation, in order to evaluate the cell size in comparison with the size of a single bar.

(respectively blue and red lines). Time $t = 0.0\,\mathrm{h}$ corresponds to the initial flat bed conditions, in which the bed variation Δz is zero in the whole domain. Starting form $t = 15.0\,\mathrm{h}$ a first appearance of alternate bars is present in the second half of the domain. First half of the domain remains flat during the whole run. A train of bars starts to form and to migrate downstream, as in the experiments of *Fujita and Muramoto* [1985] and in the numerical runs of *Defina* [2003]. Only one single train of bars arises, this suggesting a convective nature of the instability of free alternate bars.

In Fig. B.3 the temporal evolution of the bed elevation in three different couples of points L_x, R_x is shown. At $x = 2000\,\mathrm{m}$ apparently no bars arise in the whole run; at $x = 4000\,\mathrm{m}$ only one complete wavelength is present; finally, at $x = 6000\,\mathrm{m}$ a total of 5 wavelength is shown. These bars show the typical shape of free bars, with a steep front and a mild tail. Fig. B.3c shows the steep increase up to a local maximum (the crest of the bar) and a mild decreasing part. Wave celerity decreases increasing time: the first two wavelengths pass in nearly 4 h, while the last wavelength pass in nearly 5 h. This lower celerity of migration corresponds with a lower wavenumber.

In Fig. B.4 the time evolution of the wavelength is presented in the time interval $0\,\mathrm{h} \div 16\,\mathrm{h}$. Initial bar wavelength remains to values of $0.74 \div 0.76$, representative of the wavenumber of maximum amplification for mode $m = 2$. From theoretical analysis, $\beta = 18.8$ also corresponds to $\beta_C(m = 2)$. After the first 6 h, bar wavenumber decreases near values of 0.6. Final equilibrium is not completely reached when the last bars pass through the downstream section.

Bar height evolution in time is shown in Fig. B.5. Bar height evo-

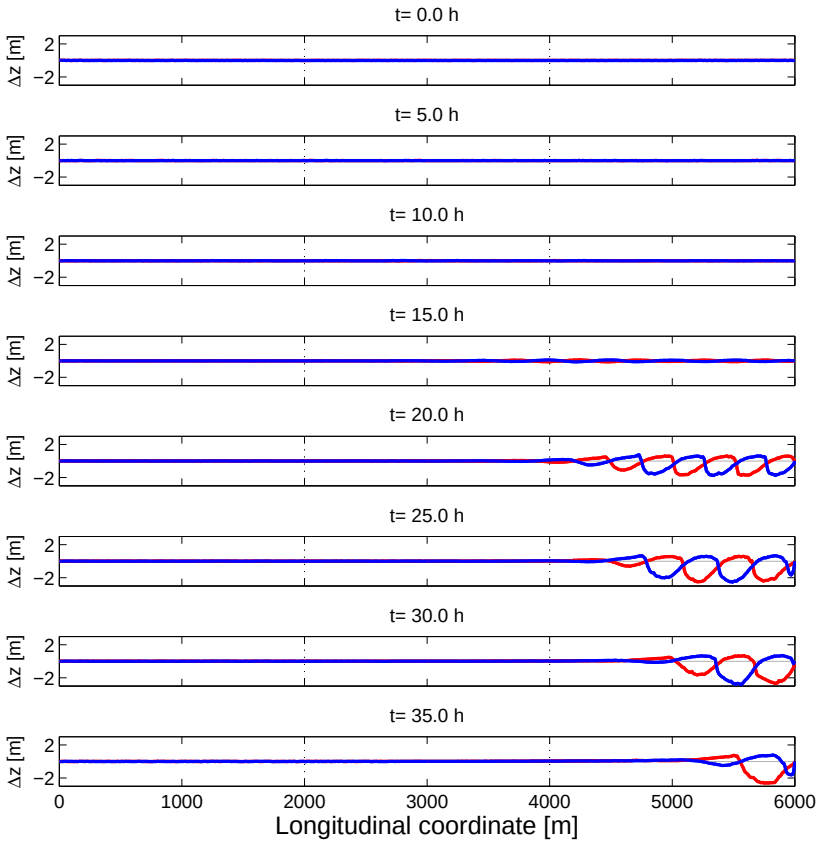

Figure B.2: Case A. Time evolution of the longitudinal bed profiles of the two longitudinal sections showed in Fig. B.1 (left in red, right in blue). Base longitudinal slope is filtered out.

lution is evaluated in different cross sections, starting from $x = 3500\,\mathrm{m}$ up to $x = 3500\,\mathrm{m}$. In the cases $x = 3500\,\mathrm{m}$ and $x = 4000\,\mathrm{m}$ bar height never reach the value of $0.5\,\mathrm{m}$. From $x = 4500\,\mathrm{m}$ to $x = 5500\,\mathrm{m}$ a peak of bar height is present, respectively for $t = 6\,\mathrm{h}$, $t = 11\,\mathrm{h}$ and $t = 16\,\mathrm{h}$. Height evolution presents two distinct behaviour in time: in a first region (up to $t = 5\,\mathrm{h}$) present a linear growth, a second region (starting from $t = 5\,\mathrm{h}$) presents a growth that tends to an equilibrium. The final part of the height evolution present a sudden decrease due to the lack of dis-

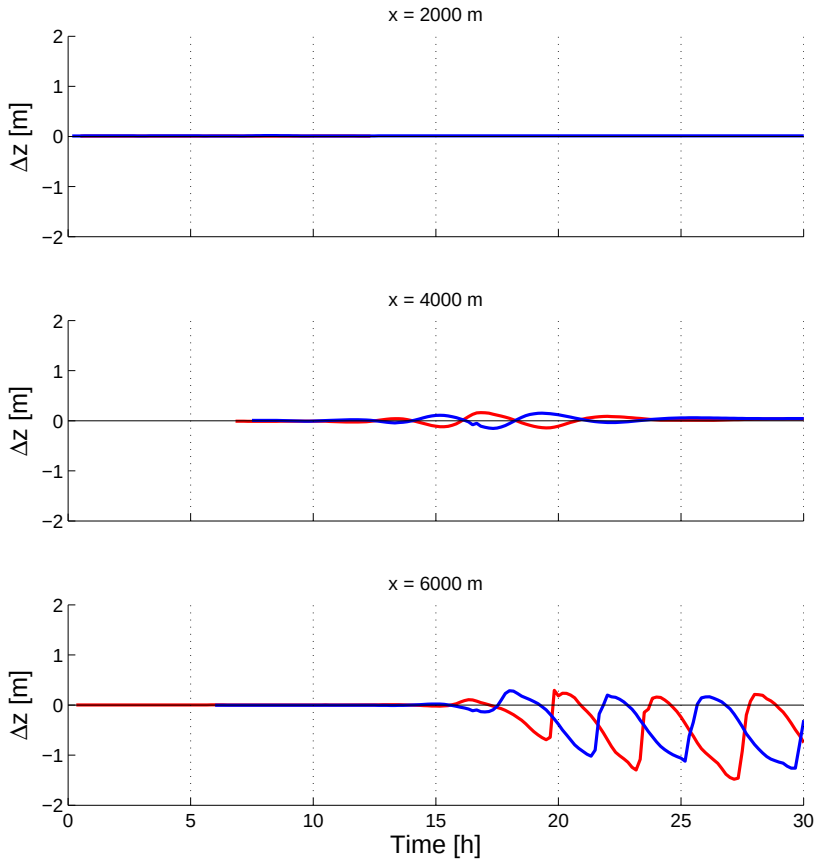

Figure B.3: Case A. Time evolution of the bed elevation in three different longitudinal coordinates: one third (x=2000 m), two thirds (x=4000 m) of the domain and at the downstream cross section (x=6000 m). Colours follow the scheme of Fig. B.1.

turbance to continue the free bar presence. Furthermore, in Fig. B.5 the theoretical value of equilibrium bar height of *Colombini et al.* [1987] is reported together with the empirical value calculated with the empirical formulation of *Ikeda* [1984].

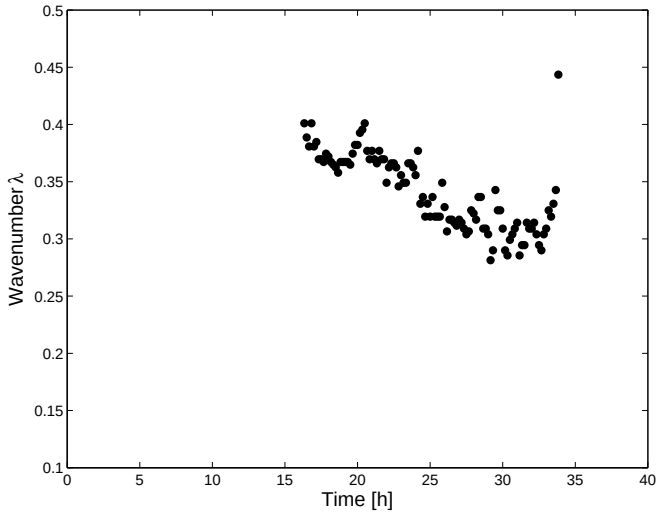

Figure B.4: Case A. Time evolution of the average value of the wavenumber $\lambda = 2\pi W/L$. Bars with $\Delta\eta > 0.1\,\mathrm{m}$ are considered in the average.

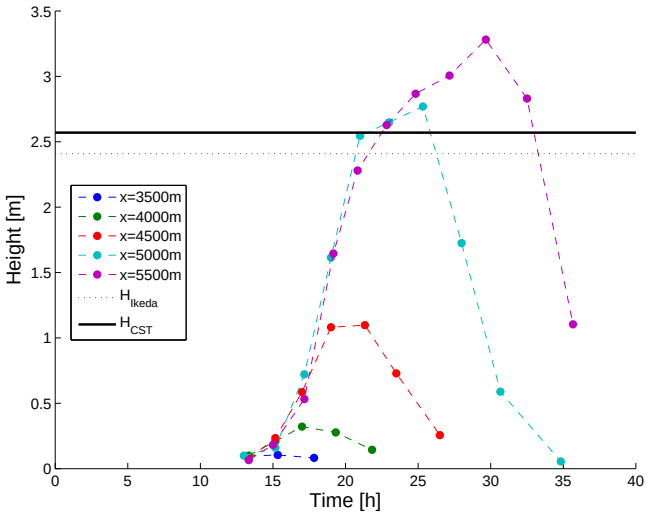

Figure B.5: Case A. Height evolution in time for different cross section in the interval $x = 3500\,\mathrm{m} \div x = 5500\,\mathrm{m}$. Two thresholds refers to theoretical value of equilibrium bar height of *Colombini et al.* [1987] (continuous line) and empirical formulation by *Ikeda* [1984] (dotted line).

Case B

Respect to Case A, Case B has the same geometrical and hydrological configuration; moreover the same initial and boundary conditions are considered. On the opposite, a random bed perturbation is added to all the cells of the mesh. Random perturbation, actually added to Basement ver. 2.6, considers two parameters that must be defined by the user: the first one consists in the maximum height of the perturbation, the second one is the time interval of two consecutive perturbation. The height of the perturbation in each cell has a probability normally distributed between zero and the maximum height parameter defined by the user. In the run of Case B, max height is set equal to 1% of the uniform flow depth, while time interval between two consecutive perturbation is set equal to 300 s.

In Fig. B.6 the longitudinal evolution of the bed elevation is shown in the time interval $t = 0.0$ h-$t = 16.0$ h. Contrarily respect to Case A in which only one train of bars appeared, here the effect of random bed perturbation is to continue triggering the free bar formation in time. Bars are downstream migrating and their appearance is similar to Case A: no alternate bars are present in the first half of the domain, due to an upstream boundary effect. Free migrating bars constantly appear from the second half of the domain, between $x = 3000$ m and $x = 4000$ m.

Fig. B.7 shows the time evolution of the bar wavenumber λ. Mean value of λ is 0.7, almost twice respect the wavenumber corresponding to the theoretical maximum amplification ($\lambda_{\Omega max} = 0.35$) of the critical conditions. In the interval 9-14 h there is a sudden temporary bar elongation, down to λ 0.55-0.6, after which the wavenumber is again nearly 0.7.

Fig. B.8 shows the time evolution of bar height in different cross sections of the second half of the domain. Cross sections $x = 3000$ m and $x = 3500$ m are still affected from the upstream boundary condition and show a non-equilibrium height. On the contrary, sections $x = 5000$ m and $x = 5500$ m shows an initial linear growth of the bar height, as presented in Case A, up to a relative maximum at 3.5 m. Starting from $t = 15$ h a pseudo-equilibrium value of the bar height is reached (nearly 3.0 m) and remains constant for the rest of the run. This pseudo-equilibrium value is slightly greater respect the theoretical equilibrium value proposed by *Colombini et al.* [1987] (Eq. 2.24) and the empirical one by *Ikeda* [1984]

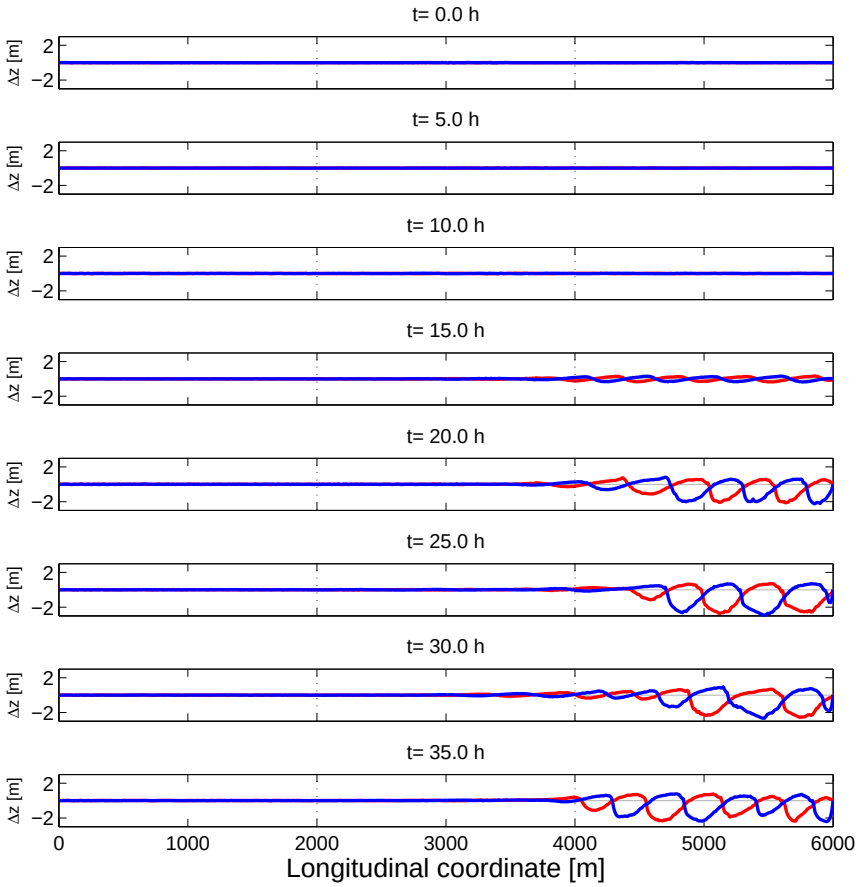

Figure B.6: Case B. Time evolution of the left and right longitudinal sections. Base longitudinal slope is filtered out.

(Eq. 2.25).

B.3.3 Forced bars

A second set of simulations is run to evaluate to which extent Basement can reproduce forced bars in a straight domain in sub- and super-resonant conditions. The geometrical and hydraulic properties of the runs follow the hypothesis of the analytical solution of *Colombini et al.* [1987]; *Zolezzi and*

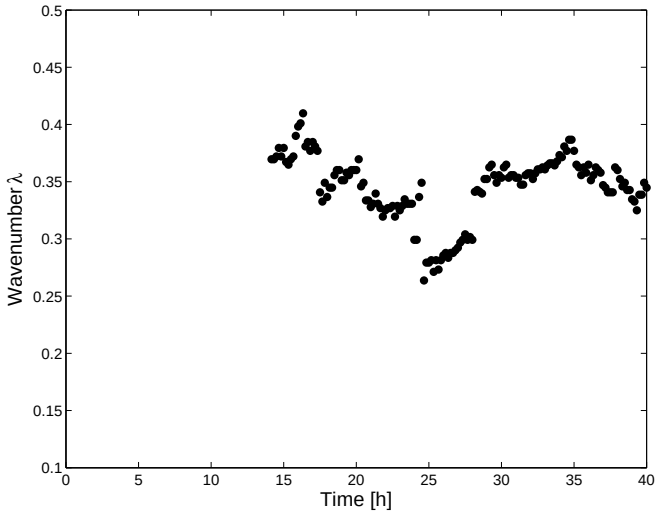

Figure B.7: Case B. Time evolution of the average value of the wavenumber $\lambda = 2\pi W/L$. Bars with $\Delta\eta > 0.1\,\mathrm{m}$ are considered in the average.

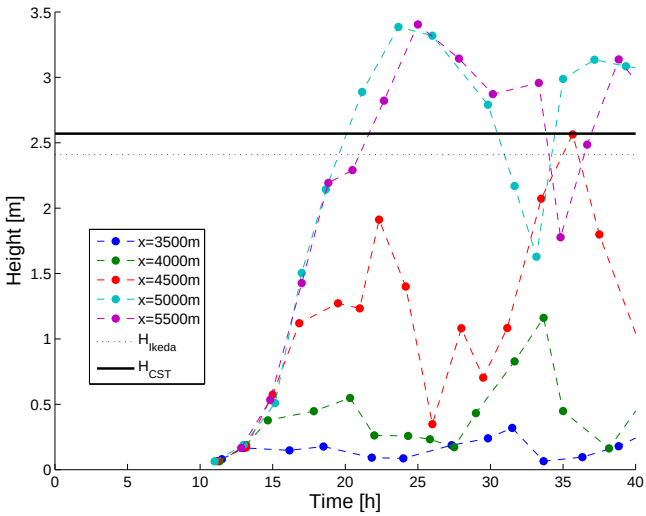

Figure B.8: Case B. Height evolution in time for different cross section in the interval $x = 3500\,\mathrm{m} \div x = 5500\,\mathrm{m}$. Two thresholds refers to theoretical value of equilibrium bar height of *Colombini et al.* [1987] (continuous line) and empirical formulation by *Ikeda* [1984] (dotted line).

Table B.3: Summary of the parameters used in the Cases Sub-Resonant and Super-Resonant.

Description	*Value*	*Unit*
Mesh Length	12000	m
Mesh Width	60	m
N. of cells	31247	–
Discharge	783.5 (sub-R); 482.1 (super-R)	m^3/s
Slope	0.011	m/m
Total run time	259200	s
Initial bed	Flat	
θ	0.100	–
d_s	0.067	–
β	12 (sub-R); 17 (super-R)	–
β_C	8.06	–
β_R	13.28	–

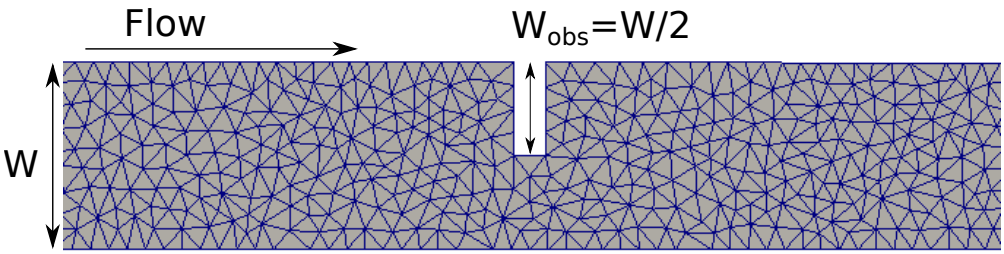

Figure B.9: Example of computational mesh used in the forced bar simulations in the neighbourhood of the local narrowing.

Seminara [2001]: rectangular cross sections, constant inflow discharge and solid discharge and uniform grain size distribution. A planform obstacle is placed at half of streamwise length. Obstacle has the form of a local narrowing of the channel, with $W_{obs} = W/2$. In Fig. B.9 the sketch of the mesh in the neighbourhood of the obstacle is shown.

Two different scenarios are described, starting from the rectangular cross section in which the bed elevation can be left free to evolve in time, without random perturbations as described in the previous case B. Cases tested are in sub-resonant conditions ($\beta < \beta_R$) and in super-resonant conditions ($\beta > \beta_R$):

Case Sub-Resonant flat bed conditions, constant inflow discharge, $\beta_C < \beta < \beta_R$;

Case Super-Resonant flat bed conditions, constant inflow discharge, $\beta_C < \beta_R < \beta$;

These cases follow the benchmark runs proposed by *Siviglia et al.* [2013] and based on the experiments of *Struiksma and Crosato* [1989], where a fix obstacle located at $x = L/2$ is add to the case of a straight domain.

Case Sub-Resonant

In Fig. B.10 the left and right longitudinal are shown at different times. The role of the local narrowing at $x = 6000\,\mathrm{m}$ is evident starting from the second time-step: a fixed scour starts forming at the right bank and a correspondent deposit is present at the left bank, immediately after the narrowing. This fixed obstacle triggers the formation of two distinct kinds of bars: a first train of free bars start forming downstream the obstacle and travels downstream like in the free bar Cases A and B; a second train of bars also starts forming right after the narrowing. These bars, forced by the obstacle, are twice longer than free bars and non-migrating. Free bar amplitude grows in time and space, up to a pseudo-equilibrium value, while forced bar amplitude is rapidly dumped in the streamwise direction: in one single bar wavenumebr the amplitude decreases by 90%. Moreover, upstream the obstacles the initial flat bed condition does not change in time. Only a 1D effect is present upstream the obstacle, due to the backwater effect induced by the narrowing. In the analysed case, the top of the deposits newer overcome the water surface elevation, so that in the whole run the bars can be considered submerged.

Fig. B.11 shows the time evolution of the average wavenumber λ. Wavenumber tends to decrease in time from values of 0.35 to values near

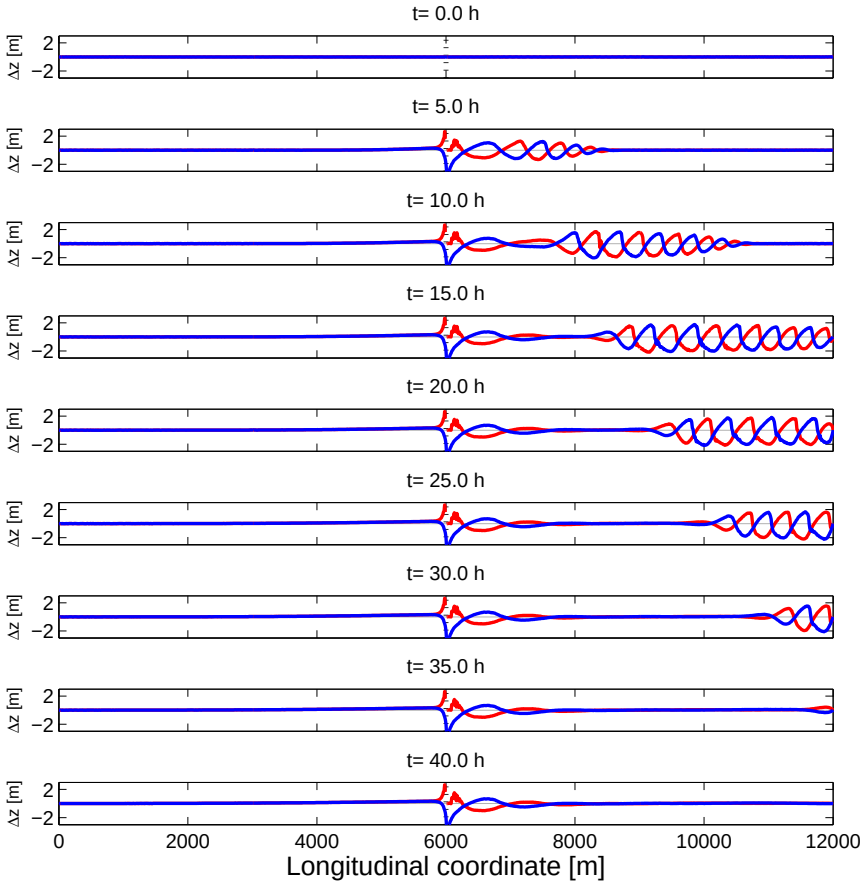

Figure B.10: Case Sub-Resonant. Time evolution of the longitudinal bed profiles of the left and right banks, respectively with red and blue lines, of the entire domain. Base longitudinal slope is filtered out.

0.2. These values can be compared with the theoretical value of $\lambda_C = 0.43$ and $\lambda_R = 0.13$. The run shows a shift from conditions of migrating bars to conditions near to non-migrating bars, even if the steady condition is not reached.

Fig. B.12 present the time evolution of bar height in different control sections with a $\Delta x = 1\,\text{km}$ downstream the local narrowing. Curves of bar height present a bell form as Case A. This run in fact present again a train

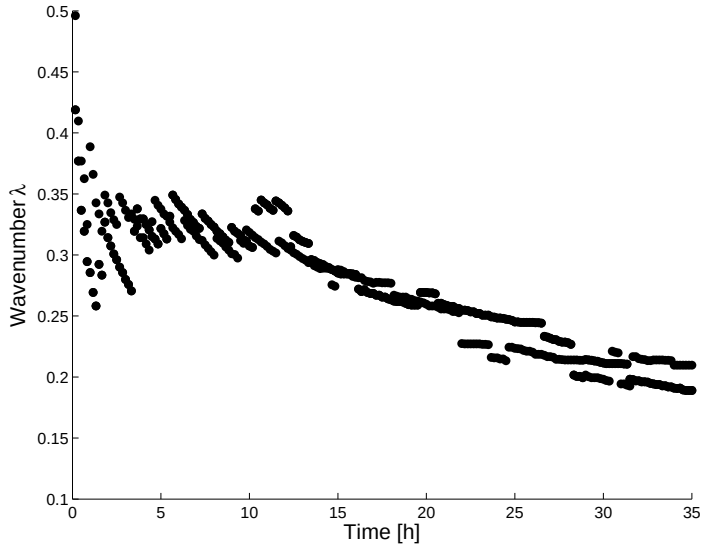

Figure B.11: Case Sub-Resonant. Time evolution of the average value of the wavenumber $\lambda = \pi W/L$. Only bars with $\Delta\eta > 0.1\,\mathrm{m}$ are considered.

of free bars that migrate downstream leaving a flat bed condition after the passage as in the case described for Case A. The relative maximum can be compared with the theoretical and empirical values of *Colombini et al.* [1987] and *Ikeda* [1984] respectively, even if these value are derived from free bars cases.

Case Super-Resonant

Fig. B.13 shows the longitudinal bed profiles of the left and right banks, respectively red and blue lines, at different times. Initial flat bed condition are evident at $t = 0.0\,\mathrm{h}$, while the role of the local narrowing at $x = 6000\,\mathrm{m}$ is evident starting from the second time-step as in the Case Sub-Resonant: a fix scour starts forming at the right bank and a correspondent deposit is present at the left bank, immediately after the narrowing. Again, the fix obstacle triggers the formation of two distinct kinds of bars: a first train of free bars start forming downstream the obstacle and travels downstream like in the free bar Cases A and B; also the second kind of bars starts forming right after the narrowing. Respect to free bars, these latter are

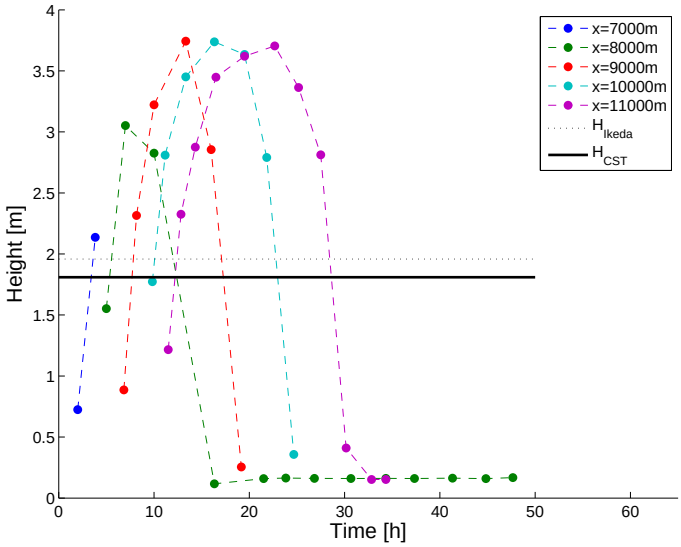

Figure B.12: Case Sub-Resonant. Time evolution of bar height for different cross sections in the interval $x = 7000\,\mathrm{m}$ $x = 11\,000\,\mathrm{m}$. Two thresholds refers to theoretical equilibrium height of *Colombini et al.* [1987] (continuous line) and empirical formulation by *Ikeda* [1984] (dotted line).

forced by the local narrowing, two times longer and non-migrating. These two different effects evolve with the same time scale, so that there is a mild shift from longer to shorter wavelength in the streamwise direction.

Moreover, upstream the obstacle the initial flat bed condition is affected by the appearance of a group of free migrating bars (e.g. see at $t = 20\,\mathrm{h}$ of Fig. B.13) and, as in the previous case, by the 1D effect due to the backwater effect induced by the narrowing.

Contrary to the theoretical behavior predicted by *Zolezzi and Seminara* [2001] and to the numerical findings of *Siviglia et al.* [2013], upstream of the obstacle non migrating bars forced by the obstacle do not form. Moreover, the top of the deposits overcomes the water surface elevation. This can be seen by the milled behaviour of the longitudinal sections. Milled behaviour of the bed elevation does not reflect the real smooth behaviour of emerging bars, due to, maybe, the way in which the wet and dry scheme is solved by the model.

Fig. B.14 shows the time evolution of the average wavenumber λ.

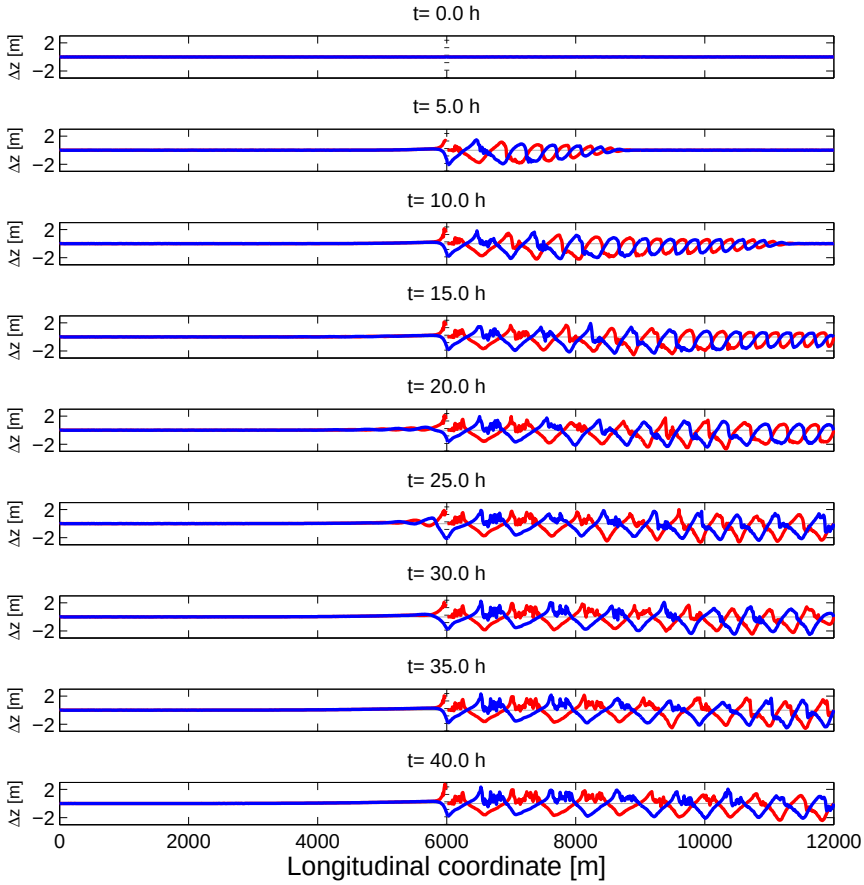

Figure B.13: Case Super-Resonant. Time evolution of the longitudinal bed profiles of the left and right banks, respectively with red and blue lines, of the entire domain. Base longitudinal slope is filtered out.

Wavenumber tends to decrease in time from values of 0.35 to values near 0.25. These values can be compared with the theoretical value of $\lambda_C = 0.43$ and $\lambda_R = 0.13$. The run shows a shift from conditions typical of migrating bars to condition in which the angular frequency ω of *Colombini et al.* [1987] is smaller (i.e. lower migration), even if the steady condition $\lambda = \lambda_R$ is not reached.

Results of both Cases Sub- and Super-Resonant are in agreement with

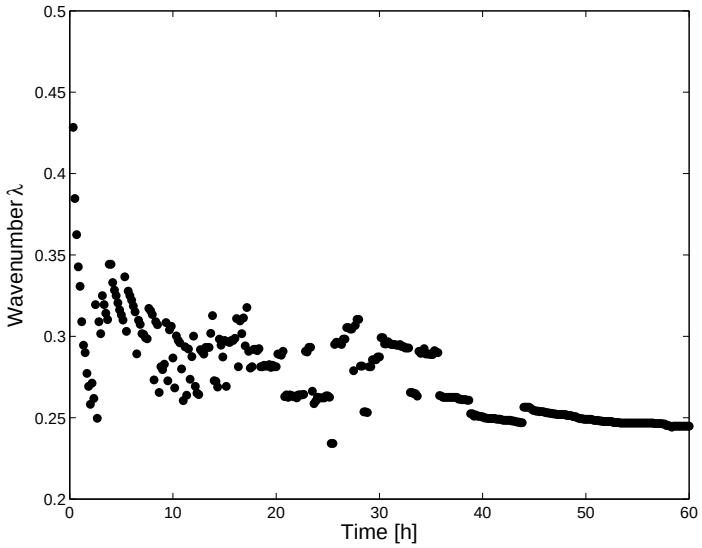

Figure B.14: Case Super-Resonant. Time evolution of the average value of the wavenumber $\lambda = \pi W/L$. Only bars with $\Delta\eta > 0.1\,\mathrm{m}$ are considered.

the findings of *Siviglia et al.* [2013], stating that the steady bars wavelengths are larger for the sub-resonant case respect to the super-resonant case.

Fig. B.15 presents the time evolution of bar height in different control sections downstream the local narrowing with a $\Delta x = 1\,\mathrm{km}$. After a rapid increase of bar height, the value reach a relative relative maximum near the theoretical and empirical equilibrium value of *Colombini et al.* [1987] and *Ikeda* [1984] respectively.

B.4 Discussion and conclusions

In this Chapter, the ability of the morphodynamic numerical model Basement to correctly reproduce the theoretical alternate free and forced bars properties and behaviour is tested.

Flume experiments (e.g. *Fujita and Muramoto* 1985; *Lanzoni* 2000a,b; *Takebayashi and Egashira* 2001), theoretical studies [*Colombini et al.*, 1987; *Stevens*, 1989; *Tubino et al.*, 1999] and numerical runs (e.g. *Federici*

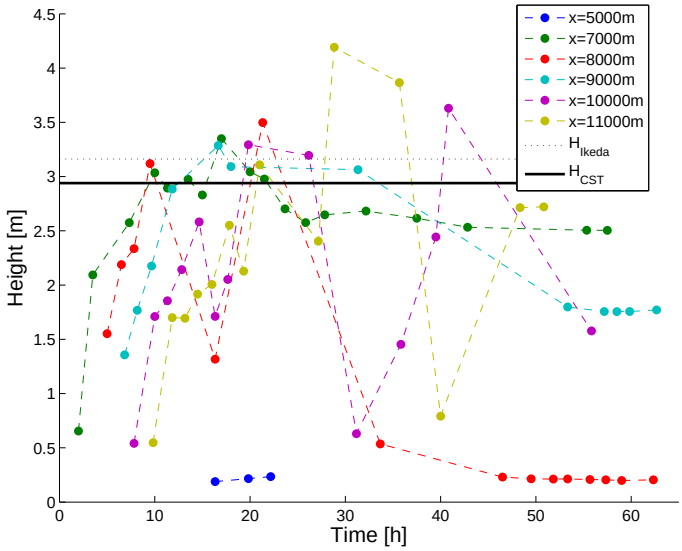

Figure B.15: Case Super-Resonant. Time evolution of bar height for different cross sections in the interval $x = 7000\,\mathrm{m}$ $x = 4000\,\mathrm{m}$. Two thresholds refers to theoretical equilibrium height of *Colombini et al.* [1987] (continuous line) and empirical formulation by *Ikeda* [1984] (dotted line).

and Colombini 2002; *Defina and Lanzoni* 2002; *Defina* 2003; *Bernini et al.* 2009) showed that free bars in straight channels, after an initial phase of development, evolve towards an equilibrium configuration in which the main bar properties reach stable values. Cases A and B show clearly the initial development of free migrating bars in terms of bar wavelength and height. The equilibrium configuration is reached only in terms of bar height, with values in good agreement with the empirical formulation of *Ikeda* [1984] and the theoretical formulation of *Colombini et al.* [1987], while bar wavenumber was still evolving at the end of the numerical tests. An upstream boundary effect is evident and prevents the formation of alternate bars in an interval of nearly 100 times the width of the numerical domain. The initial configuration triggers the formation of a train of free bars that migrate downstream as showed numerically e.g. by *Bernini et al.* [2009].

Bar wavelength is calculated as the longitudinal distance between two consecutive crests in the same bank side. The associated longitudinal

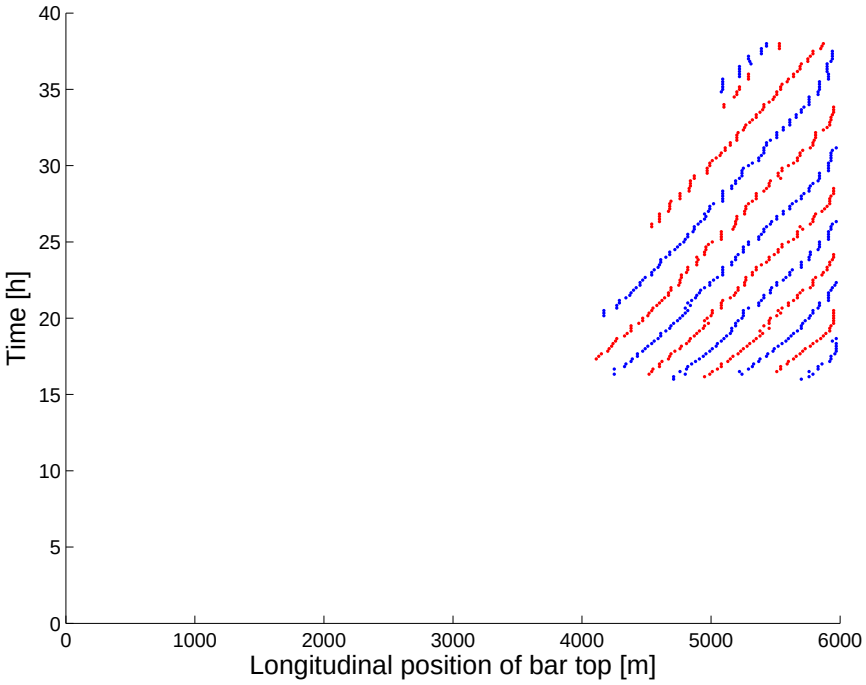

Figure B.16: Case A. Evolution in time of the alternate bars tops along left and right longitudinal sections, respectively indicated with red and blue dots.

frequency of the crests, named bar wavenumber, is calculated as $\lambda = \pi W/L$. Both Cases A and B showed values initially decreasing in time from 0.4 to 0.30-0.35. The analysis of free bar theory by *Colombini et al.* [1987] shows that the most probable value of bar wavenumber (i.e. the one associated with the maximum growth rate) is 0.35, in good agreement with the numerical outcomes.

Bar celerity of Cases A and B is estimated by tracking the longitudinal position of the bar crests over time. The value of the celerity of a single deposit is given by the slope of its corresponding curve (see Fig. B.16 and fig. B.17 for Case A and Case B respectively), similarly to what showed by *Defina* [2003]; *Bernini et al.* [2009]. Mean celerity of the Case A is approximately $2.9\,\mathrm{cms}^{-1}$, while of the Case B is nearly $3.2\,\mathrm{cms}^{-1}$.

Cases Sub-Resonant and Super-Resonant reproduce with morphodynamic model Basement the occurrence of steady alternate bars forced by

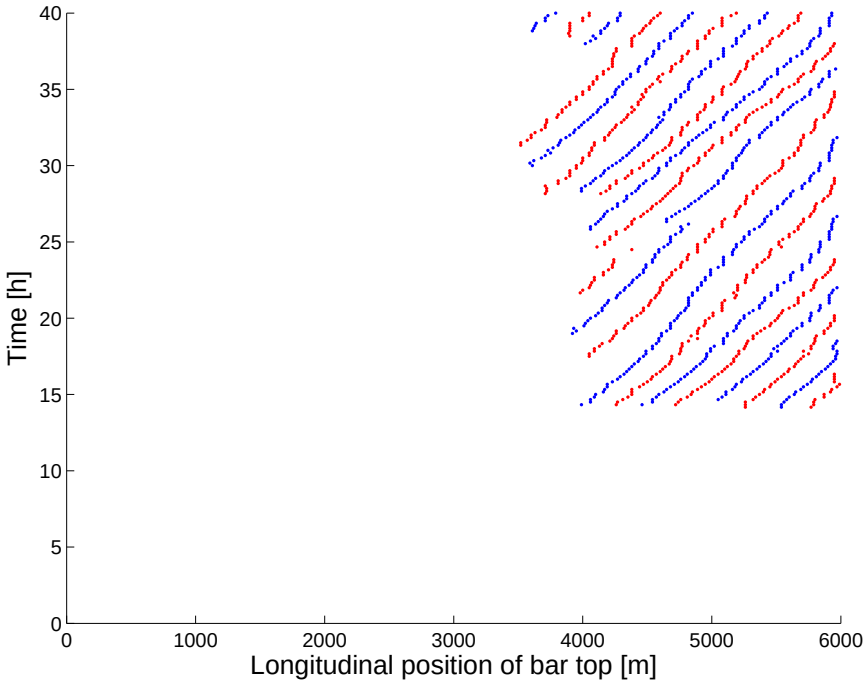

Figure B.17: Case B. Evolution in time of the alternate bars tops along left and right longitudinal sections, respectively indicated with red and blue dots.

a fixed constraint of the channel geometry [*Siviglia et al.*, 2013]. As shown experimentally e.g. by *Struiksma et al.* [1985]; *Zolezzi et al.* [2005]; *Crosato et al.* [2011, 2012] bars forced by a fixed constraint are longer than free bars and much less migrating. Moreover, *Zolezzi and Seminara* [2001] analytically defined the role of resonance in the development of alternate bars upstream or downstream the constraint and their spatial growth or damping.

Fig. B.18 and Fig. B.19 summarize these different aspects showing the longitudinal position in time of bar tops of left and right banks (respectively in red and blue). Fig. B.18 shows the initial evolution of migrating bars downstream the local narrowing at x=6000 m. Numerical model correctly reproduce non migrating alternate bars downstream the constraint. After 10 h a single wavelength reached the equilibrium amplitude, while celerity decreased to zero. In the remaining part downstream the local

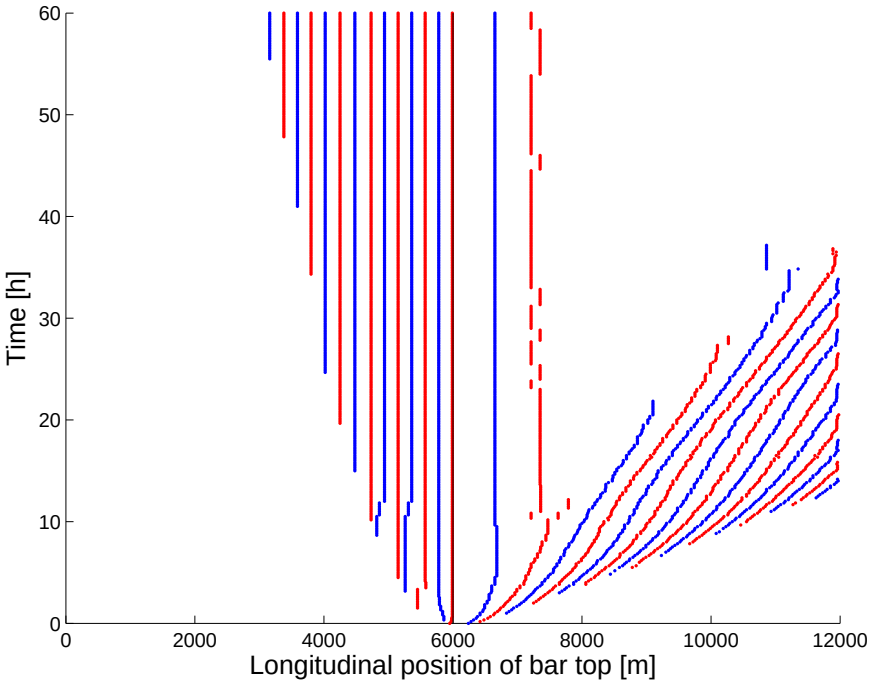

Figure B.18: Case Sub-resonant. Evolution in time of the alternate bars tops along left and right longitudinal sections, respectively indicated with red and blue dots.

narrowing a train of free bars start developing with a similar behaviour of Cases A and B. Equilibrium bar wavenumber is nearly 0.25, greater than the theoretical resonant conditions for non-migrating bars [*Colombini et al.*, 1987] and at the same time lower than the wavenumber of free migrating bars. Furthermore, a series of non-migrating bars also form upstream the obstacle, with a wavenumber nearly 0.35.

Fig. B.19 shows the evolution in time of the bar crests in the super-resonant case. In good accordance with the results of *Siviglia et al.* [2013], alternate bars form upstream and downstream the local narrowing. The former are migrating bars, contrary with the numerical results of *Siviglia et al.* [2013] and the theoretical super-resonant behavior; downstream the constraint, as in the sub-resonant case a train of downstream migrating bars form starting from the constraint itself, but in this case slowly evolves

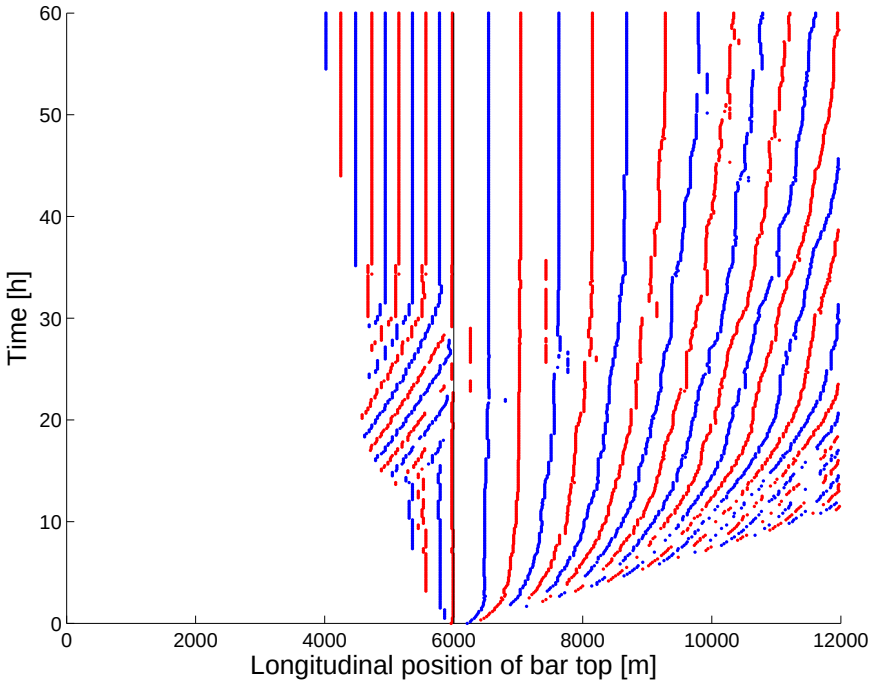

Figure B.19: Case Super-resonant. Evolution in time of the alternate bars tops along left and right longitudinal sections, respectively indicated with red and blue dots.

in non-migrating bars. Accordingly with *Siviglia et al.* [2013], bar wavelengths result larger for the sub-resonant case (around 22 times the width, $\lambda = 0.14$) respect the super-resonant case (around 16 times the width, $\lambda = 0.19$), with values more than 30% larger than the ones found by *Siviglia et al.* [2013], and nearer the theorerical resonant (non-migrating) conditions of *Colombini et al.* [1987].

In the version used in the present work (2.5.1), Basement does not include a module modules for lateral bank erosion neither for spiral flow parametrisation, similarly with model GIAMT2D [*Siviglia et al.*, 2013]. On the contrary, Delft3D include these modules (see e.g. *Schuurman et al.* [2013] for a recent application). Although the morphodynamic model Basement is still in a development phase, the tested version is already capable to correctly reproduce the main morphological processes of alternate

bars.